

Doctoral Dissertation, 2013

Radiation Hydrodynamic Studies of  
Line-Driven Disk Wind in Active Galactic Nuclei

OCHANOMIZU UNIVERSITY

Division of Advanced Sciences,  
Graduate School of Humanities and Sciences

Mariko NOMURA

March, 2014



# Abstract

We research the dynamics of the line-driven disk wind in the active galactic nuclei (AGNs) by radiation hydrodynamic calculations and compare them to the X-ray observations of broad absorption line (BAL) quasars and ultra-first outflow (UFO) in Seyfert galaxies. The observations of blueshifted absorption lines by metals suggest the outflow with the large velocity  $\sim 10,000 \text{ km s}^{-1}$ – $90,000 \text{ km s}^{-1}$  ( $0.3c$ ) in the active galactic nuclei, where  $c$  is the velocity of the light. The origin of the outflow is still unknown and the existing phenomenological model for AGNs cannot reproduce these outflows, since the obscuring torus that is the absorber assumed in the model is just rotating around the nuclei and cannot explain the large blueshifted speed.

Our aim is to investigate the dynamics and structure of the outflow, to explain the origin of the absorption lines, and furthermore, to establish the theoretical model of the AGN including the outflow. We focus on the plausible model for the outflows, the line-driven disk wind model, in which the radiation force due to spectral lines (line force) accelerates the matter on the surface of the accretion disk and induces the disk wind.

First we investigate the steady structure of the line-driven disk wind by calculating streamlines of the wind and compare with X-ray observation. We found the funnel-shaped winds with a half opening angle of  $\sim 50^\circ$  in the wide parameter space,  $\varepsilon = 0.3$ – $0.9$  and  $M_{\text{BH}} = 10^7$ – $10^{8.5} M_\odot$ , where  $\varepsilon$  is the Eddington ratio and  $M_{\text{BH}}$  is the black hole mass. The BAL features appear when the system is observed from an observer with the viewing angle,  $\sim 50^\circ$ . A resulting probability of detecting BAL is  $\sim 7$ – $11\%$ , which is roughly consistent with the abundance ratio of BAL quasars,  $\sim 10$ – $15\%$ .

Second we perform the two-dimensional radiation hydrodynamic simulations of line-driven disk wind to investigate more realistic structure of the wind. We find that the funnel-shaped disk wind is basically consistent with the calculation of the streamlines as we have mentioned above, and newly find the time variation of the column density, velocity, and ionization degree. In the upper region of the funnel (typically  $\lesssim 70^\circ$ ), the matter is powered by the line force near the disk surface and is not accelerated at the higher latitude. Therefore the terminal velocity of the wind is relatively small,  $v_r \lesssim 0.1c$ , and a part of the matter returns to the disk. In the equatorial region (typically  $\gtrsim 70^\circ$ ), the wind continues to be accelerated even after the launching, and the outflow velocity reaches  $0.3$ – $0.4c$ . As a result, for  $\varepsilon = 0.3$ – $0.9$  and  $M_{\text{BH}} = 10^8$ – $10^9 M_\odot$ , the UFO features are observed in the direction of  $\sim 70^\circ$  and come and go at the time scale from  $\sim 20$

days to several months. The resulting short timescale ( $\sim 20$  days) is similar to the rapid variability ( $\sim 7$  days) reported by the X-ray observations. The time-averaged UFO probability is 20–30%, which is comparable to or slightly smaller than that estimated by the observation,  $\sim 50\%$ . For  $\varepsilon \lesssim 0.1$  and  $M_{\text{BH}} \lesssim 10^{7.5} M_{\odot}$ , the disk wind is launched, but the UFO probability is pretty small or null, since the column density of the matter of which the ionization state is suited for producing the metal absorption lines are small.

We conclude that the disk wind is successfully launched by the line force and the line-driven disk wind model can reproduce the absorption features of the BAL and UFO. In addition, the detection of the absorption lines are depend on not only the viewing angle but also the Eddington ratio and the black hole mass.

# Contents

<b>1</b>	<b>Introduction</b>	<b>5</b>
1.1	Introduction to AGNs . . . . .	5
1.2	Unified model of AGNs . . . . .	6
1.3	Absorption lines and outflows . . . . .	9
1.3.1	Broad absorption line (BAL) . . . . .	9
1.3.2	Ultra-fast outflow (UFO) . . . . .	10
1.3.3	Impact on environment of AGNs and importance of the outflow . . . . .	12
1.4	Disk wind model . . . . .	13
1.4.1	Outline . . . . .	13
1.4.2	Time variability of absorption lines and new picture of wind model . . . . .	15
1.5	Line-driven wind model . . . . .	16
1.5.1	Outline . . . . .	16
1.5.2	Line force . . . . .	20
1.5.3	Previous works . . . . .	27
1.6	Motivations and aim of this work . . . . .	32
<b>2</b>	<b>Non-Hydrodynamic Calculation for BAL Quasars</b>	<b>34</b>
2.1	Method . . . . .	34
2.1.1	Outline . . . . .	34
2.1.2	Initial conditions and basic equations . . . . .	35
2.1.3	Radiative fluxes of X-ray and ultraviolet . . . . .	38
2.1.4	Force multiplier . . . . .	41
2.1.5	Assessment of BAL probability . . . . .	42
2.2	Results . . . . .	43
2.2.1	Structure of line-driven wind . . . . .	43
2.2.2	BAL probability . . . . .	46
2.3	Discussions . . . . .	49
2.3.1	Comparison with observations . . . . .	49
2.3.2	Comparison with previous works and motivations for hydrodynamic simulations . . . . .	50
<b>3</b>	<b>Radiation Hydrodynamic Simulations for Line-Driven Disk Wind</b>	<b>53</b>
3.1	Method . . . . .	53

3.1.1	Basic equations and set up . . . . .	53
3.1.2	Boundary conditions . . . . .	54
3.1.3	Initial conditions . . . . .	55
3.1.4	Line force . . . . .	55
3.1.5	The code . . . . .	56
3.2	Results . . . . .	58
3.2.1	Structure of line-driven wind . . . . .	58
3.2.2	Mechanism of acceleration . . . . .	61
3.2.3	Comparison with observations of UFOs . . . . .	67
3.2.4	Parameter dependence . . . . .	80
3.3	Discusstions . . . . .	92
3.3.1	Comparison with observations . . . . .	92
3.3.2	Comparison with previous works . . . . .	93
3.3.3	Future works . . . . .	94
<b>4</b>	<b>Conclusion</b>	<b>98</b>

# 1 Introduction

## 1.1 Introduction to AGNs

The galactic center, which shows the energetic phenomena such as powerful radiation or jets, is called active galactic nucleus (AGN). Such powerful phenomena are thought to be triggered by the accretion disk around the supermassive black holes, where about 10% of the mass energy of the accreting matter can be converted to the radiation energy and/or kinetic energy of the jets (see § 1.2 for detail). Today, all of the galaxies are believed to have the supermassive black holes at their center, but about half of the galaxies have the AGNs. We introduce some major classes of the AGNs.

**Seyfert galaxy** — This type of galaxy has the AGN whose luminosity is relatively low, from  $10^{42}$  ergs $^{-1}$  to  $10^{44}$  ergs $^{-1}$ . They show the various emission lines from the ionized gas including the metals. Based on the line width, Seyfert galaxies are classified into type 1 and type 2 (Khachikian & Weedman, 1974).

For type 1 Seyfert galaxies, we can observe broad emission lines of which FWHM (full width at half maximum) is from  $1000$  km s $^{-1}$  to  $10,000$  km s $^{-1}$ , and narrow emission lines of which FWHM is several  $100$  km s $^{-1}$ . For type 2 Seyfert galaxies, only the narrow emission lines are observed. Examples of the broad emission lines are the recombination line of H and He, and especially H $\alpha$   $\lambda 656.3$  nm and H $\beta$   $\lambda 656.3$  nm appear. In the UV spectra, we can observe Ly $\alpha$   $\lambda 121.6$  nm, HeII  $\lambda 164.0$  nm and so on. In addition, the metal lines, such as NV, CIV, CIII] and MgII, are also observed as the broad emission lines in the type 1 Seyferts. For the type 2 Seyferts, these lines are observed as the narrow emission lines. The forbidden lines are narrow for both types of Seyfert galaxies. Examples are [OII]  $\lambda\lambda 372.6, 372.9$ nm, [OIII]  $\lambda\lambda 495.9, 500.7$ nm, [NII]  $\lambda\lambda 654.8, 658.3$ nm and [SI I]  $\lambda\lambda 671.7, 673.1$ nm.

The continuum spectra of the Seyfert covers the wide range of the wavelength from optical to X-ray and bluer than that of non-AGN galaxies. This is because the radiation from the accretion disk with high temperature ( $\sim 10^5$  K) contributes to the total spectra in the case of Seyfert, whereas in non-AGN galaxies, the spectra consists of the emission of the stars ( $\sim$ several  $1000$ – $10000$  K). This strong radiation from the nuclei of the Seyferts makes the photoionization region and various line emissions come from there.

**Radio galaxy** — Galaxies with the bright radio emission are called radio galaxies. The radio luminosity of the radio galaxies is  $100$ – $1000$  times larger than that of Seyfert galaxies. However, except for the strong radio radiation, the spectral features of the radio

galaxies are quite similar to those of the Seyfert galaxies. Then the radio galaxies are identified as a sort of AGNs and are also classified into type 1 and 2 by the existence or non-existence of the broad emission lines. Type 1 and type 2 radio galaxies are called broad line radio galaxies and narrow line radio galaxies respectively. In contrast to the fact that Seyfert galaxies are spiral galaxies, most of the radio galaxies are elliptical galaxies. The radio galaxies are accompanied with the radio jet that is extended over the size of the host galaxy.

**Quasar** — Quasars are the most luminous subclass of the AGNs. The criteria of difference between Seyfert galaxies and quasars are the luminosity,  $M_B = -21.5 + 5 \log h_0$ , where  $M_B$  is the optical B-band magnitude and  $h_0$  is the Hubble constant normalized by  $100 \text{ km s}^{-1} \text{ Mpc}^{-1}$ . If the B-band magnitude is smaller than the criteria (i.e. the B-band luminosity is larger than the criteria), the galaxies are classified as the quasars. Historically, the quasars were observed as the radio sources of which corresponding objects were unknown since the nucleus is so bright that the host galaxy could not be observed. Today, the host galaxies are observed because of the improvement of the observation technology and it becomes clear that there is no essential difference between the quasars and Seyfert galaxies. As we have mentioned above, one of the differences is luminosity. Another difference is the ratio of the number of type 1 objects to the number of the type 2 objects. Although the number of type 2 Seyferts are comparable to or slightly larger than that of type 1 Seyferts, most quasars are classified as type 1 objects. By the optical and UV observations, large number of quasars with no strong radio emission are detected. Radio quiet quasars are 90% of all quasars.

## 1.2 Unified model of AGNs

The unified model is proposed to simply explain the difference between type 1 and 2. In this model, the main components of the AGN are the accretion disk, the broad line region, the narrow line region and the obscuring torus. Figure 1.1 is the schematic picture of the unified model of the AGN. The black hole is located at the center. The accretion disk surrounding the black hole is a main engine and a source of the continuum emission. In the broad and narrow line regions, the matter is photoionized by the continuum, and the line emission is produced. The broad line region is located near the central black hole. The narrow line region is distributed farther from the nucleus than the broad line region. The obscuring torus absorbs the continuum from the disk and the line emission from the broad line region. In some cases, the AGN has the jet.

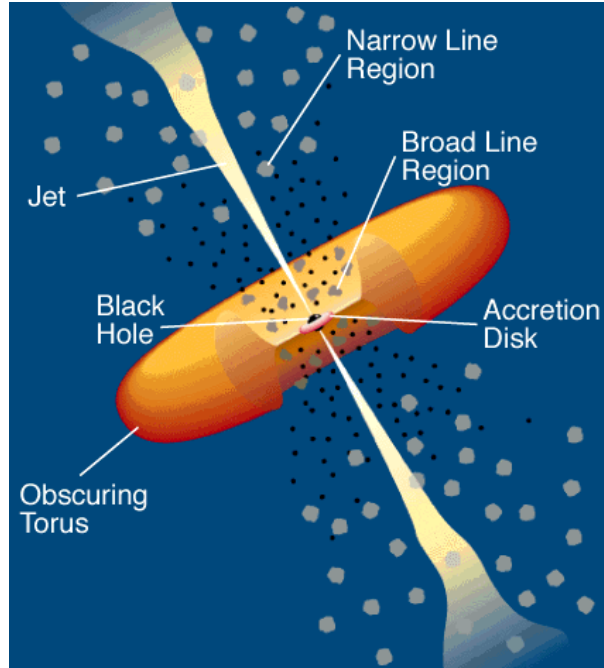


Figure 1.1: Schematic picture of the unified model of the AGN (from the web page of NASA, Credit: C.M. Urry and P. Padovani).

The gas around the black hole inflows due to the gravitational force, but the gas has the angular momentum and forms the disk like structure, called the accretion disk. The angular momentum is transferred outward due to the viscosity and the gas gradually falls into the black hole. During this process, the gravitational energy is converted to thermal energy via viscosity. Then the thermal energy is converted to radiation energy and the accretion disk shines brightly. The most famous disk model, which is established by Shakura & Sunyaev (1973), is called as the standard disk model. Its features are listed bellow:

- The disk is geometrically thin and optically thick.
- The temperature of the disk is high at the inner region and low at the outer region.
- Radiation from the accretion disk is multi-temperature black body.

The optical and UV continuum of the Seyfert galaxies and the quasars are well fitted by the standard disk model, since the disk temperature is several  $10^4$  K  $-10^5$  K near the black hole, leading to the strong optical and UV emissions. Though the origin of the X-ray is still unknown, the corona above the inner disk is might be the source of X-ray radiation.

The various emission lines are observed AGNs (see § 1.1). They would be emitted from a lot of gas clouds around the black holes. The origin of the width of these lines is thought to be the kinematic motion rather than the thermal broadening. The broad lines should be emitted in the region where gas clouds move with the velocity of 1000–10,000 km s<sup>-1</sup>, and the narrow emission lines would be emitted in the region where gas clouds move with the velocity of  $\sim 100$  km s<sup>-1</sup>. The former region is called the broad line region (BLR) and the latter region is called the narrow line region (NLR). For the Seyfert galaxies, the broad emission lines vary after 100 days following the variation of the continuum. This time delay suggests that the BRL is photoionized by the continuum and that BRL is located at  $\lesssim 0.1$  pc from the nucleus. The following variation of the narrow lines is not observed. However, the size of the NLR is estimated by the imaging. The NLR is a conical shape and is spread to  $\sim 100$  pc from the nucleus.

The obscuring torus is located at  $\sim 0.1$  pc from the black hole, which is between the BLR and NLR. Ionizing radiation is transferred without attenuation by the obscuring torus in the polar direction, and the wide ionized region (NLR) is formed here. The disk and the BLR are not obscured when we observe the AGN in the pole-on direction. Thus we detect the features of the type 1 AGNs, the broad emission lines with the narrow emission lines and the undiluted soft X-ray emission. On the other hand, if the AGN is observed from the edge-on direction along which the torus obscure the disk and BLR. We detect only the narrow emission lines without the broad emission lines and the soft X-ray is attenuated by the obscuring torus. These observational features are that of type 2 AGNs. The dichotomy of the type 1 and 2 is simply explained by the observers' viewing angle.

There is the observation supporting the unified model that the scattered broad emission lines are observed in type 2 AGNs (e.g., Antonucci & Miller, 1985). It is impossible to observe the BLR directly for the type 2 AGNs, but this indirect observation of BLR is the evidence that the type 2 AGNs have the BLR.

Until now, typical features of the AGNs appearing in their spectra are well explained by the unified model. However, the unified model is phenomenologically proposed without physical bases. Recently the absorption lines are observed in the spectra, which cannot be reproduced by the unified model. These absorption features might be the key to understand the AGNs.

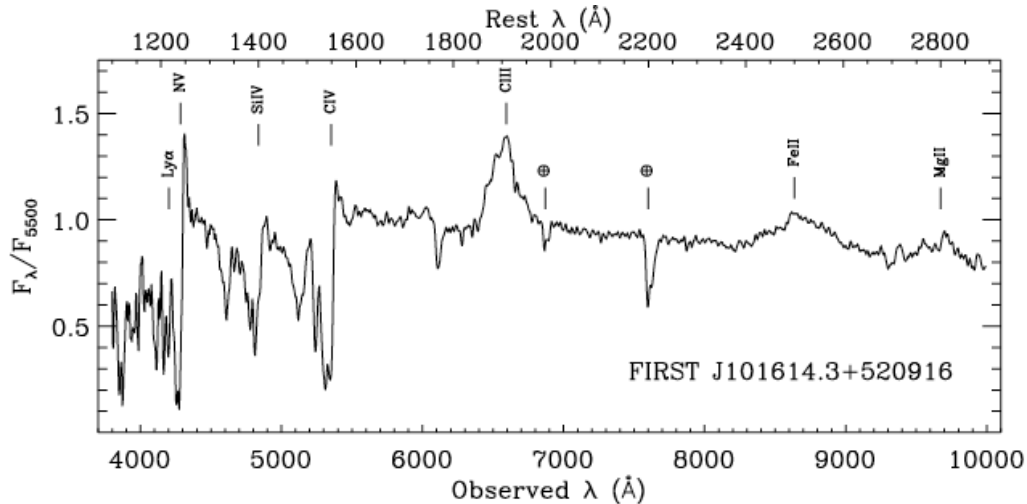


Figure 1.2: Continuum subtracted spectrum of a BAL quasar (Gregg et al., 2000). BAL features of CIV and SiIV appear at around  $1500 \text{ \AA}$  and  $1350 \text{ \AA}$  in the rest frame.

### 1.3 Absorption lines and outflows

Recently the AGNs that show the blueshifted absorption lines in their spectrum are observed. The blueshifted absorption features could not be reproduced by the obscuring torus just rotating around the black hole. If there is the absorber moving toward the observer along the line of sight, the blueshifted absorption lines appear on the spectra because the absorption wavelength is blueshifted due to the Doppler effect. That is, the blueshifted absorption lines imply the existence of the outflows. Roughly 10–20 % of the quasars show the wide blueshifted absorption lines in the optical or UV spectra and about half of the Seyfert galaxies are thought to have the blueshifted absorption features in the X-ray band. Thus, outflows are no longer rare phenomena, but ubiquitous components of AGNs. The unified model is no longer perfect, and needs to be modified. We should research the acceleration mechanism and the structure of the outflow. Here, we show the typical absorption lines of the AGNs.

#### 1.3.1 Broad absorption line (BAL)

A portion of quasars show the blueshifted absorption lines in their rest frame UV spectra. Among them, absorption troughs covering a continuous velocity range of  $2000 \text{ km s}^{-1}$  ( $\text{FWHM} > 2000 \text{ km s}^{-1}$ ) are called broad absorption lines (BALs).

Figure 1.2 shows the spectrum of BAL quasars normalized by the continuum flux at  $5500 \text{ \AA}$  (Gregg et al., 2000). We can find the CIV BAL at around  $1500 \text{ \AA}$  and SiIV

BAL at around  $1350 \text{ \AA}$  in the rest frame. The line centers are marked with the name of elements, where the line center means the wavelength of the radiation that is absorbed by the static ion via the bound-bound transition. The widths of these BALs are roughly  $15,000 \text{ km s}^{-1}$  and the velocities of the blueshift are  $17,200 \text{ km s}^{-1} - 20,000 \text{ km s}^{-1}$ . The absorption troughs are deep and the remaining continuum is less than 90% in the wide range. The thermal broadening cannot explain the large width of the BALs. If we try to explain the line width of  $15,000 \text{ km s}^{-1}$  by the thermal broadening, the temperature becomes unrealistically high. Then the wide absorption trough is interpreted as the superposition of the absorption lines with different outflow velocities and the absorbers are accelerated along the line of sight. The large blueshift means that the absorber moves toward the observer with a large velocity,  $\sim 20,000 \text{ km s}^{-1}$ . There are BALs with much larger blueshifted speeds,  $0.2c$  (e.g., Jannuzi et al., 1996). Then, to reproduce the broadening and blueshift of the BALs, we need the outflow strongly accelerated toward the observer. In addition, to explain the deep absorption trough, the column density of the outflow is expected to be  $\sim 10^{23} \text{ cm}^{-2}$ . The BALs typically come from the ions at moderate ionization states such as CIV and/or SiIV. This means that the outflow contains the moderately ionized metals and the fully ionized outflow is unacceptable. The BALs are roughly observed in 15–20% of quasars (Weymann et al., 1991; Hamann et al., 1993; Allen et al., 2011).

Here, we mention the other class of absorption lines appearing on optical/UV spectra. The absorption lines of which FWHM is less than  $500 \text{ km s}^{-1}$  are called the narrow absorption lines (NALs). The class between BAL and NAL is mini-BAL ( $500 \text{ km s}^{-1} < \text{FWHM} < 2000 \text{ km s}^{-1}$ ). Their origin is also unknown, but the same as the BALs, the outflow is the plausible origin.

### 1.3.2 Ultra-fast outflow (UFO)

In addition to BALs in the UV spectra, recently the absorption features are observed in the X-ray spectra. The absorption lines by the highly ionized Fe, FeXXV and/or FeXXVI, suggest ultra-fast outflows (UFOs) (e.g., Pounds et al., 2003). The velocity of the UFO is  $> 10,000 \text{ km s}^{-1}$ . Tombesi et al. (2010) survey 42 local radio-quiet Seyfert galaxies and they find that almost half of them have the UFOs. Figure 1.3 is the example of the spectrum showing the absorption line of the UFO (Tombesi et al., 2011). The top panel shows the background subtracted spectrum with the best-fit model (red line). The middle panel shows the best-fit model, and the bottom panel is the background spectrum. The

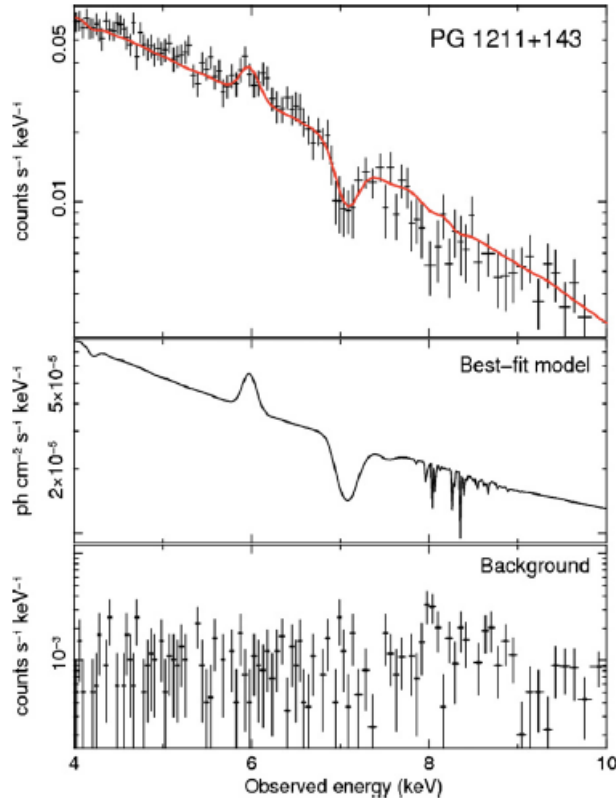


Figure 1.3: X-ray spectrum of the PG 1211+143 (Tombesi et al., 2011). The top panel shows the background subtracted spectrum with the best-fit model (red line). The middle panel shows the best-fit model and the bottom panel shows the background spectrum. The absorption line appearing at  $\sim 7$  keV is the  $\text{He}\alpha$  ( $1s^2-1s2p$ ) line of  $\text{FeXXV}$  and suggests the UFO whose velocity is  $\sim 0.15c$ .

absorption line appearing at  $\sim 7$  keV is  $\text{He}\alpha$  ( $1s^2-1s2p$ ) line of  $\text{FeXXV}$  and suggests the UFO whose velocity is  $\sim 0.15c$ .

Figure 1.4 shows the histograms of the outflow velocity, the ionization parameter,  $\xi$ , and the column density,  $N_{\text{H}}$ , in the left, middle and right panels (Tombesi et al., 2011). The ionization parameter is defined as  $\xi = L_{\text{ion}}/4\pi nR^2$ , where  $L_{\text{ion}}$  is the ionizing luminosity,  $n$  is the number density, and  $R$  is the distance from the light source. Solid lines show the histograms of UFOs and dashed lines show the histograms of the outflows with the lower velocity,  $< 10,000 \text{ km s}^{-1}$ . We focus on the histograms of UFOs. The left panel shows that the outflow velocity spans from  $10,000 \text{ km s}^{-1}$  to  $90,000 \text{ km s}^{-1}$  ( $\sim 0.3c$ ) and the peak value is about  $42,000 \text{ km s}^{-1}$  ( $\sim 0.14c$ ). The ionization parameters are in the wide range of  $\log \xi \sim 2.5-6$  and the peak value is  $\log \xi \sim 4.2$ . The ionization state,  $\log \xi \sim 6$ , means that the Fe ions are almost fully ionized. The column densities are distributed in a wide range,  $N_{\text{H}} \sim 10^{22}-10^{24} \text{ cm}^{-2}$ . To reproduce the absorption features

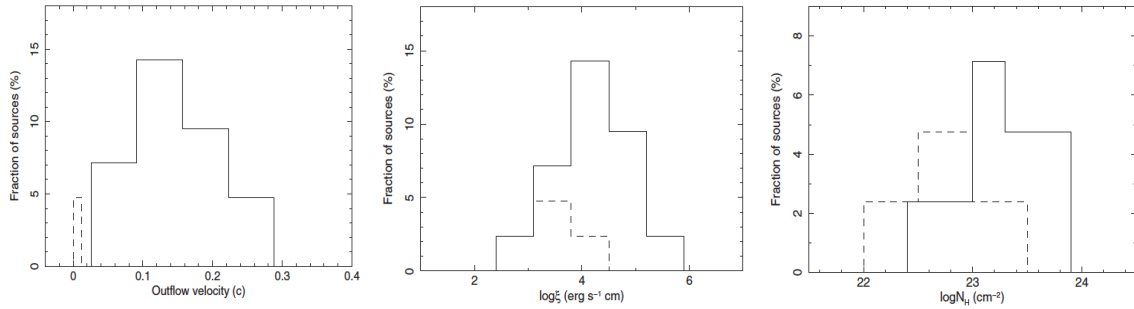


Figure 1.4: Histograms representing the distribution of the outflow velocity (left panel), the ionization parameter (middle panel), and the column density (right panel) (Tombesi et al., 2011). Solid lines show the distributions of the UFOs and dashed lines show the distribution of the absorption lines with the lower velocity ( $< 10,000 \text{ km s}^{-1}$ ).

of UFOs, the outflow should meet above conditions of the outflow velocity, the ionization parameter and the column density.

From above estimated values, Tombesi et al. (2012a) estimated the location, the mass outflow rate and the energy outflow rate. They find that the outflowing matter is located between  $100R_{\text{S}}$  and  $10^4R_{\text{S}}$  from the nucleus. This result indicates that the probable origin of the UFO is the outflow launched from the accretion disk. The mass outflow rate obtained by assuming the biconical geometry (for details to Krongold et al., 2007; Tombesi et al., 2012a) is large,  $\sim 10\%$  of the mass accretion rate. In addition, the kinematic energy is comparable to the bolometric luminosity.

### 1.3.3 Impact on environment of AGNs and importance of the outflow

The outflow has the impact on other phenomena surrounding the AGNs.

One of the important phenomena probably affected by the outflow is the growing of the supermassive black hole. The supermassive black hole grows by the mass accretion through the accretion disk. However, if the outflow is ejected from the disk, the mass is lost on the way of the accretion. Then, it is possible that the mass fed into the black hole becomes smaller and the growth of the supermassive black hole becomes slow. Such a slowdown is nontrivial, since the mass outflow rate estimated from the observation of UFOs is comparable to or slightly smaller than the accretion rate.

The feedback on the host galaxy is also the important phenomenon.  $M - \sigma$  relation, which is the correlation between the black hole mass and the velocity dispersion of the bulge, suggests the coevolution of the supermassive black hole and the host galaxy (e.g., Magorrian et al., 1998; Gültekin et al., 2009). That is, the nuclei and the host galaxies are

interacting with each other. The outflow might have the key role of the feedback from the AGNs on the host galaxies. For example, the outflow, especially UFO, potentially has an influence on star formation in the host galaxy. In fact, the outflow velocity and the mass outflow rate of the UFOs are very large. The kinetic energy of the UFOs is comparable to that of the jet (Tombesi et al., 2012a). The outflow might compress the interstellar matter and enhance the star formation, but on the other hand, the interstellar matter is heated by the shock and the star formation is suppressed when the outflow clashes with the interstellar matter. Details of the feedback are still under the discussion, but research on the outflow might give us the hint to resolve the process of the feedback.

In addition, the outflow is closely related to other components of the AGNs. For instance, there is the idea that the origin of the BLR clouds is explained by the outflow from the accretion disk (e.g., Ganguly et al., 2003; Miniutti et al., 2013). Thus, the investigating the outflow leads to understand the origin of the AGN structure including BLR.

To investigate the outflow is the important basis to resolve the evolution of the super massive black hole, interstellar mater of the host galaxies, and the structure as well as the formation mechanism of AGNs.

## 1.4 Disk wind model

### 1.4.1 Outline

To explain the absorption features, the phenomenological model is proposed. Based on the observation, there are two constraints on the geometry of the outflow: (1) the outflow is not ejected from the vicinity of the black hole; (2) the outflow is not collimated.

Based on the observational data, the launching region is roughly estimated by assuming that the outflow velocity is equal to the escape velocity. The estimated location of  $100 R_S$  suggests that the outflow is the accretion disk wind and not the ejection from the vicinity of the black hole like a jet. Thus, the origin of the outflow is thought to be the wind launched from the surface of the accretion disk (disk wind).

Weymann et al. (1991) suggested that the dichotomy between the BAL and non-BAL quasars is caused by observers' viewing angles, since the properties of emission lines and the continuum of the BAL and non-BAL quasars are remarkably similar. Then the detection probability of the absorption lines is interpreted as the covering factor of the wind. Here, the covering factor means the ratio of the solid angle covered by the outflow to  $4\pi$ . To explain the detection rates of the BALs, 15–20%, and UFOs, 50%, the wind

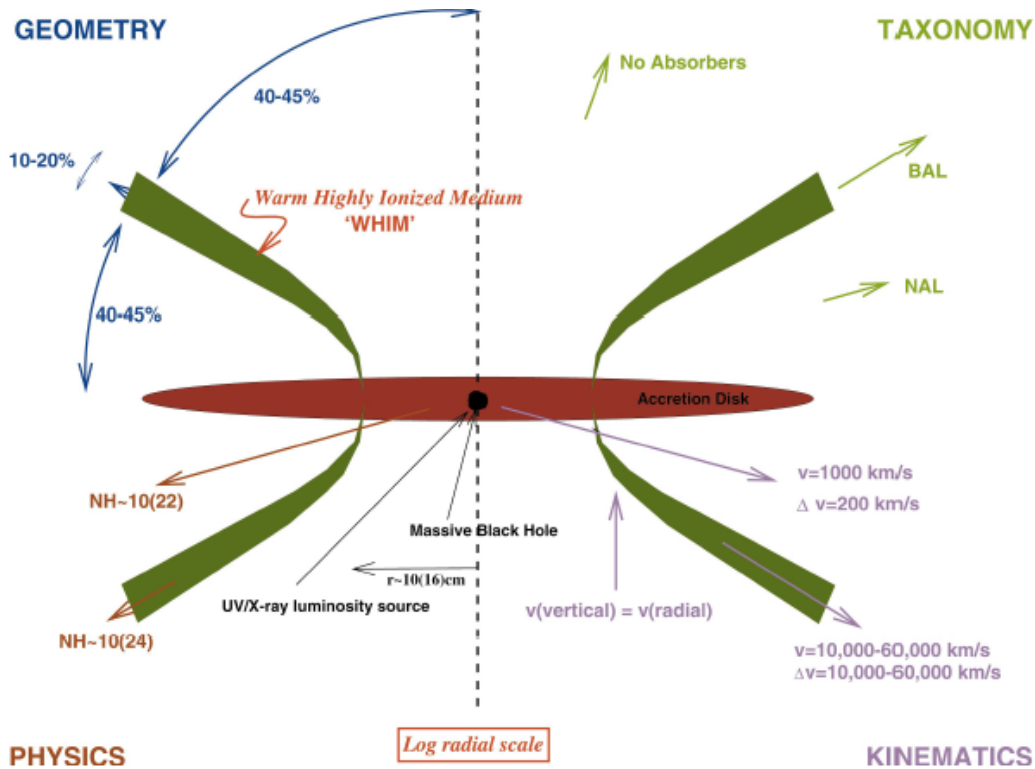


Figure 1.5: Schematic picture of the disk wind model (Elvis, 2000). The funnel-shaped disk wind is launched from the accretion disk. BALs are detected when observer's viewing angle is along the disk wind.

needs to have the large covering factor. The collimated outflow like a jet cannot reproduce such a large covering factor.

Based on the suggestion of the observations, the disk wind model that meets above two constraints is proposed by (Elvis, 2000; Ganguly et al., 2001). Figure 1.5 shows the schematic picture of the disk wind model by Elvis (2000). The funnel-shaped wind is launched from the accretion disk surface and accelerated outward. The absorption lines are detected when the disk wind interrupts the line of sight. BALs are observed when the disk wind is accelerated toward the observer because the velocity component along the line of sight is enough large to reproduce the large blueshifted speed of BALs. When we observe the quasar from the pole-on direction, there is no wind between the nucleus and the observer and we do not detect BAL features. When we observe the wind along the line of sight that crosses the wind, the absorption features are observed, but the maximum velocity and the velocity width are smaller than those when the wind observed from the front. Then, the absorption lines are classified as NALs. The width of the funnel is set to meet the condition that the covering factor of the wind is consistent with the detection

rate of the BALs.

If the disk wind has the geometry shown in Figure 1.5, the observational features are partly explained. The important remaining problem is that the launching mechanism of the wind is still unknown. In addition, this model cannot explain the time variability of the absorption lines, which is recently detected. Next, we briefly introduce the phenomenological wind model including the time variability, and after that, we explain the acceleration mechanism.

#### 1.4.2 Time variability of absorption lines and new picture of wind model

Recently the time variability of the absorption lines is observed. It is difficult to explain the complex variability by the smooth and steady funnel-shaped wind. Then, the phenomenological picture is changing in do the clumpy disk wind model. We show the example of the time variability of the BAL in Figure 1.6 (Rodríguez Hidalgo et al., 2013). CIV absorption lines show the drastic change within  $\sim 3$  yr in the quasar rest frame. The time scale of the variability of BALs ranges from several weeks to 10 yr (Misawa et al., 2007; Capellupo et al., 2012, 2013).

The origin of the time variability is still unknown, but the most plausible scenario is that the ionization state of the BAL clouds fluctuates. The shielding clouds cross between the BAL clouds and the continuum source, and induce the time variation of the ionization state (Misawa et al., 2007; Capellupo et al., 2013).

In this scenario, the disk wind has the clumpy structure and the individual clouds are accelerated outward with the rotational motion. Along the line of sight, when shielding clouds are located just between the continuum source and BAL clouds, shielding clouds dilute the ionizing flux, and the ionization state of the BAL clouds becomes low. Conversely, if no shielding cloud is between the nucleus and the BAL clouds, the BAL clouds are strongly ionized by the ionizing continuum. As a consequence, by the shielding clouds crossing the line of sight, the ionization state of the BAL clouds fluctuates, and the resulting absorption features also fluctuate. In this case, more than one BAL shows the fluctuation at the same time independently of the outflow velocity. In fact, in some quasars, BALs with the different blueshifted velocities vary at one time (e.g., Capellupo et al., 2013). This observation supports the scenario of shielding clouds crossing.

Capellupo et al. (2013) estimated that the shortest time scale of the variability of the BAL, 8–10 days, needs large transverse velocity of the crossing clouds, 10,000–80,000  $\text{kms}^{-1}$ . Assuming that the transverse velocity is equal to the Keplerian velocity,

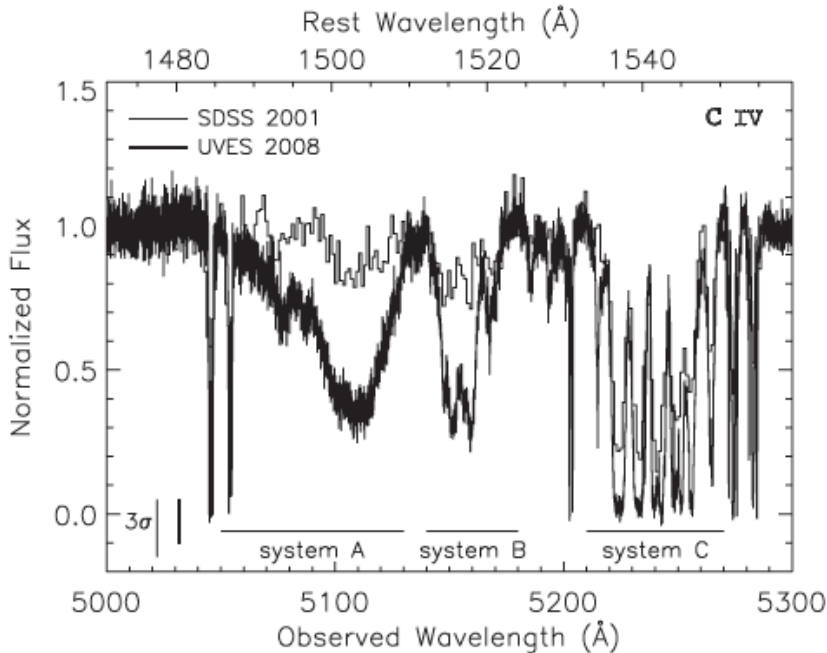


Figure 1.6: Example of the time variability of the BAL (Rodríguez Hidalgo et al., 2013). The CIV absorption lines show the changes within  $\sim 3$  yr in the quasar rest frame. System A, B, and C are the CIV absorption lines with the different outflow velocities.

the distance of the shielding clouds is  $\sim 0.001$ – $0.2$  pc ( $10$ – $200R_S$  for the black hole mass of  $10^7M_\odot$ ). This shielding cloud might correspond to the X-ray shielding gas or the disk wind in the region of several  $100R_S$  (see § 1.5.1).

To explain the time variability of the BALs, other scenarios are also proposed. For instance, variability due to BAL cloud itself, which intersects the line of sight, or due to fluctuation of the ionizing radiation from the nucleus. In reality, there could be more than one origin of the time variability. Variability with the different origins overlaps one another, then, the emergent variability of the absorption lines is complicated. It is important to research whether the disk wind has the clumpy structure and to examine the scenario of the time variability. However, this is beyond the scope of this paper and we discuss this problem as one of the future works (see § 3.3.3).

## 1.5 Line-driven wind model

### 1.5.1 Outline

Now we think about the acceleration mechanism of the disk winds. The phenomenological disk wind model is proposed to reproduce the observational features: (1) the outflow is not ejected from the vicinity of the black hole; (2) the outflow is not collimated. In

addition, there are important conditions suggested by the observation: (3) the metals in the wind are not fully ionized, since the moderately ionized metal lines are detected; (4) the wind is ejected from the sub-Eddington source. The sub-Eddington source means the nucleus which luminosity is lower than the Eddington luminosity. (The Eddington luminosity is the luminosity when the radiation force due to the electron scattering and the gravitational force balance.) The Eddington luminosity is obtained as

$$L_{\text{Edd}} = \frac{4\pi cGM_{\text{BH}}}{\sigma_e}, \quad (1.1)$$

where  $G$  is the gravitational constant,  $M_{\text{BH}}$  is the mass of the central black hole, and  $\sigma_e$  is the mass-scattering coefficient for free electrons.

Many theoretical models have been proposed to account for the origin of the outflows so far. One plausible scenario is that of ‘magnetically driven winds’ (Blandford & Payne, 1982; Konigl & Kartje, 1994; Everett & Murray, 2007). In this model, the matter is magnetically accelerated. However, this model needs an extra mechanism to meet the condition (3) that the metals are moderately ionized, since the gas irradiated by the strong X-ray around the nucleus is fully photoionized (the so-called overionization problem). Another idea is the acceleration by the radiation force. However, for the sub-Eddington sources of which luminosity is lower than the Eddington luminosity, the radiation force due to the electron scattering is smaller than the gravity, and the material cannot escape the system.

Therefore, we consider the radiation force due to spectral lines (line force). Nowadays, the line-driven disk wind model is the most plausible model that can meet the conditions (1)–(4) at one time (Murray et al., 1995; Proga et al., 2000; Proga & Kallman, 2004; Risaliti & Elvis, 2010). First, we show the outline of the line-driven disk wind model.

The line force is the force due to metals absorbing the UV radiation through the bound-bound transition. The line force accelerates the wind effectively because the accretion disks in the AGNs are bright in the UV band. In addition, when the absorber is accelerated, the line force becomes more efficient. This is because of the Doppler effect. The wavelength of the radiation absorbed by the static absorber through the bound-bound transition is determined uniquely. However, the wavelength of the radiation absorbed by the moving absorber is shifted due to the Doppler effect. When we assume that the disk wind is gradually accelerated outward, though the slow wind near the continuum source absorbs the UV radiation in the certain wavelength, the wind with the high velocity distant from the continuum source can be accelerated by absorbing the UV radiation in

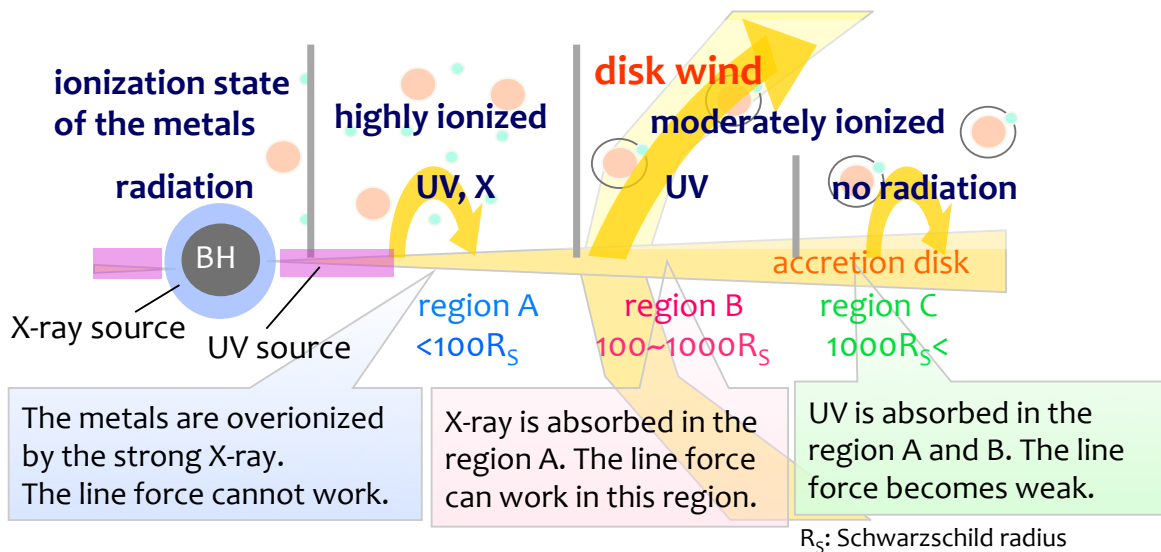


Figure 1.7: Schematic picture of the line driven disk wind. The inner region of the accretion disk is bright in the UV, and the X-ray source is the vicinity of the black hole. In the region distant from the black hole, named the region B, the metals are moderately ionized because the X-ray is attenuated in the region A. As a result, the line force works effectively and the disk wind is successfully launched.

the different wavelength. This is the reason why the line force is very effective for the accelerated absorber (for details to § 1.5.2). This line-driving mechanism is efficient even in the sub-Eddington sources since the opacity via bound-bound transition is larger than that for Thomson scattering.

Since the AGNs are bright not only in the UV but also in the X-ray, we have to consider that the X-ray ionizes the metals. If the metals are fully ionized by the X-ray, the absorption through the bound-bound transition is suppressed. As a result, the line force becomes less effective. The ionization state of the metals is the key to understand the acceleration mechanism and the structure of the line-driven disk wind in the AGNs.

We show the schematic picture of the line driven disk wind in Figure 1.7. The inner region of the accretion disk is the UV radiation source, and the X-ray source is the vicinity of the black hole. In the region near the central black hole labeled the region A, the metals are fully or highly ionized by the strong X-ray radiation. Then bound-bound transition is prevented and the line force cannot accelerate the wind. In the region distant from the black hole, labeled the region B, the metals are moderately ionized because the X-ray is attenuated in the region A. In this situation, the line force works effectively and the disk wind is successfully launched. Typically the wind launching region is located at  $100\text{--}1000R_S$  away from the black hole (e.g. Proga et al., 2000; Risaliti & Elvis, 2010). In

the more distant region from the center, labeled the region C, the UV radiation is also attenuated in the region A and B. Then even if the metals are moderately ionized, the line force cannot accelerate the wind.

The line-driven disk wind is launched from the accretion disk surface in the middle distance from the black hole, in which the metals are moderately ionized. That is, this model can explain both the acceleration and the ionization state of the wind at one time without any other mechanism for tuning the ionization state. The resulting wind is accelerated outward, and not collimated like a jet. In addition, as we explained above, the line-driven wind is accelerated even in the sub-Eddington sources. Therefore, we find that the line-driven disk wind model meets the observational conditions (1)–(4). Our research focuses on this model.

### 1.5.2 Line force

The treatment of the line force is developed by Castor, Abbott, & Klein (1975) (hereafter CAK75) and Stevens & Kallman (1990) (hereafter SK90). In this subsection, we explain the line force based on these papers. The line force is the radiation force due to the metals absorbing the UV radiation through the bound-bound transition. The line force works efficiently to the accelerated absorber. In this section, we introduce the line force working on the accelerated wind in the various ionization states.

First, we consider the line force due to the single spectral line. When the absorber is static, the metals absorb only the radiation of which frequency around the line center,  $\nu_0$ . Then the profile of the spectral line becomes the Gaussian due to the thermal fluctuation. However, when we consider the accelerated absorber, the line center is shifted by the Doppler effect,

$$\nu'_0 = (1 + \frac{v}{c})\nu_0, \quad (1.2)$$

where  $\nu'_0$  is the line center of the absorption line by the metal of which velocity is  $v$ . The disk wind is gradually accelerated from nearby the accretion disk (UV source) to a distance. That is, the wind is slow near the disk and fast in the distant region. Thus, due to the Doppler effect, the line force effectively accelerates the wind. Though the slow wind near the disk absorbs the radiation whose frequency is around the line center, the fast wind far from the disk can absorb the radiation with more large frequency. This is because the line center of the fast wind is more shifted than that of the slow wind.

For simplicity, we approximate the line profile by the rectangle. The absorber is distributed continuously and moves with constant acceleration along the light ray. We assume that the density and the temperature of the absorber are constant. Figure 1.8 shows the velocity of the absorber and the frequency of the line along the light-ray. We consider the line force working on the fluid element with the geometrical width  $s$ , which corresponds to the region painted with a green. The frequency of the line center at  $s_A$  is  $\nu'_0$ , then the fluid element absorbs the radiation of which frequency is from  $\nu'_0 - \Delta\nu$  to  $\nu'_0 + \Delta\nu + \Delta\nu s/L$ , where  $L$  is the distance between  $s_A$  and  $s_B$  and  $s_B$  is the point at which the frequency is shifted by  $\Delta\nu$  from the frequency at  $s_A$ . In other words, between the distance  $L$ , the frequency is shifted by  $\Delta\nu$ . Then,

$$\Delta\nu = \frac{\nu_0}{c} \frac{dv}{ds} L, \quad (1.3)$$

where  $dv/ds$  is the velocity gradient along the right-ray. On the other hand,  $\Delta\nu$  is written

as

$$\Delta\nu = \nu_0 \frac{v_{\text{th}}}{c}, \quad (1.4)$$

because  $\Delta\nu$  is the same as the line width due to the thermal fluctuation. From the equations (1.3) and (1.4), we derive

$$L = v_{\text{th}} \left| \frac{dv}{ds} \right|^{-1}, \quad (1.5)$$

where we take the absolute value of the velocity gradient to include the case that the acceleration is negative. The optical depth corresponding to the geometrical width,  $L$ , is

$$\tau_L = \kappa_L \rho v_{\text{th}} \left| \frac{dv}{ds} \right|^{-1}, \quad (1.6)$$

where  $\kappa_L$  is the absorption coefficient of the specific line and  $\rho$  is the density of the absorber. The radiation of which frequency is  $\nu'_0 - \Delta\nu < \nu < \nu'_0 + \Delta\nu$  is attenuated by the absorber between the light source and  $s_A$  [see the case (1) of Figure 1.8]. The radiation of which frequency is  $\nu'_0 + \Delta\nu < \nu < \nu'_0 + \Delta\nu + \Delta\nu s/L$  is not attenuated between the element and the light source [see the case (2) of Figure 1.8]. Then the radiation force due to the single line absorption,  $f_{\text{rad,L}}$ , is

$$\begin{aligned} f_{\text{rad,L}} &= \int_{\nu'_0 - \Delta\nu}^{\nu'_0 + \Delta\nu} \left[ \frac{\kappa_L F_c}{\tau_s c} e^{-\tau_1(\nu)} \int_0^{\tau_2(\nu)} e^{-\tau} d\tau \right] d\nu \\ &\quad + \int_{\nu'_0 + \Delta\nu}^{\nu'_0 + \Delta\nu + \Delta\nu s/L} \left[ \frac{\kappa_L F_c}{\tau_s c} \int_0^{\tau_2(\nu)} e^{-\tau} d\tau \right] d\nu, \end{aligned} \quad (1.7)$$

$$\simeq \frac{2\kappa_L F_c \Delta\nu (1 - e^{-\tau_L})}{c\tau_L}, \quad (1.8)$$

where  $F_c$  is the radiative flux in a vacuum independent of the frequency. In the above equation,  $\tau_1(\nu)$  is the optical depth between the light source and  $s_A$  and  $\tau_2(\nu)$  is the optical depth of the fluid element. These optical depths depend on the frequency. In Figure 1.8,  $\tau_1(\nu)$  and  $\tau_2(\nu)$  are identical to the widths of the pink band and the green band. Here, we assume that the fluid element is enough far from the light source and  $\nu'_0 - \Delta\nu > \nu_0 + \Delta\nu$ . The optical depth,  $\tau_s$ , is corresponding to the geometrical width,  $s$ , and we suppose  $\tau_s \gg 1$ .

We calculate the line force due to a single absorption line above, but for more realistic case, there are a number of absorption lines in the spectrum. Then, we have to include

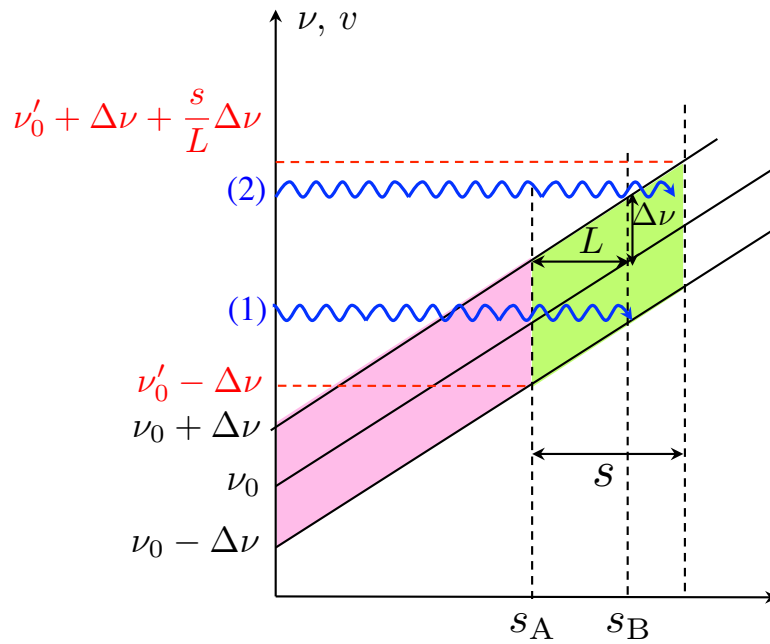


Figure 1.8: Velocity and frequency of a single line, which is made by the absorber that moves with the constant acceleration along the light-ray. The horizontal axis is the distance from the light source along the ray. We consider the line force working on the fluid element with the geometrical width  $s$ , which corresponds to the green region. The radiation labeled (1) is attenuated by the absorber between the light source and  $s_A$  (the pink region). The radiation labeled (2) is not absorbed in the inner pink region.

their contribution to the force. The total line force due to the ensemble of lines is

$$\begin{aligned}
F_{\text{rad,L}} &= \sum_{\text{line}} f_{\text{rad,L}}, \\
&= \frac{\sigma_e F}{c} \sum_{\text{line}} \frac{F_c \Delta\nu_D}{F} \frac{1 - e^{-\eta t}}{t}, \\
&= \frac{\sigma_e F}{c} M(t),
\end{aligned} \tag{1.9}$$

where  $F$  is the radiative flux integrated by the frequency across the range where the lines are distributed,  $\Delta\nu_D$  is the full width of the lines,  $\Delta\nu_D = 2\Delta\nu$ ,  $\eta$  is the ratio between the opacity of the line absorption and the electron scattering,  $\eta = \kappa_L/\sigma_e$ , and  $t$  is called the local optical depth parameter,

$$t = \tau_L/\eta = \sigma_e \rho v_{\text{th}} \left| \frac{dv}{ds} \right|^{-1}. \tag{1.10}$$

In the bottom row of the equation (1.9),  $\sigma_e F/c$  is the radiation force due to the electron scattering. Therefore,  $M(t)$  is the ratio of the line force to the radiation force due to the electron scattering, which is called the force multiplier,

$$M(t) = \sum_{\text{line}} \frac{F_c \Delta\nu_D}{F} \frac{1 - e^{-\eta t}}{t}. \tag{1.11}$$

For  $t \ll 1$ , the force multiplier is

$$M(t) \simeq \sum_{\text{line}} \frac{F_c \Delta\nu_D}{F} \eta = \text{const}, \tag{1.12}$$

end for  $t \gg 1$ ,

$$M(t) \simeq \sum_{\text{line}} \frac{F_c \Delta\nu_D}{F} \frac{1}{t} \propto \frac{1}{t}. \tag{1.13}$$

The force multiplier is large for the small local optical depth parameter. The local optical depth parameter becomes small when the velocity gradient is large, the temperature is low, and/or the density is small. If the velocity gradient is large, the slope of the  $v - s$  plot in Figure 1.8 is more steep. When the temperature is small, the width,  $\Delta\nu$  is small. In both cases, the contribution to the line force from the radiation with no attenuation between the light source and  $s_A$  increases. In the case that the density is small, the attenuation between the element and the light source becomes less effective. That is, the small local optical depth parameter,  $t$ , means that the element absorbs the much UV radiation. As a result, the force multiplier becomes large.

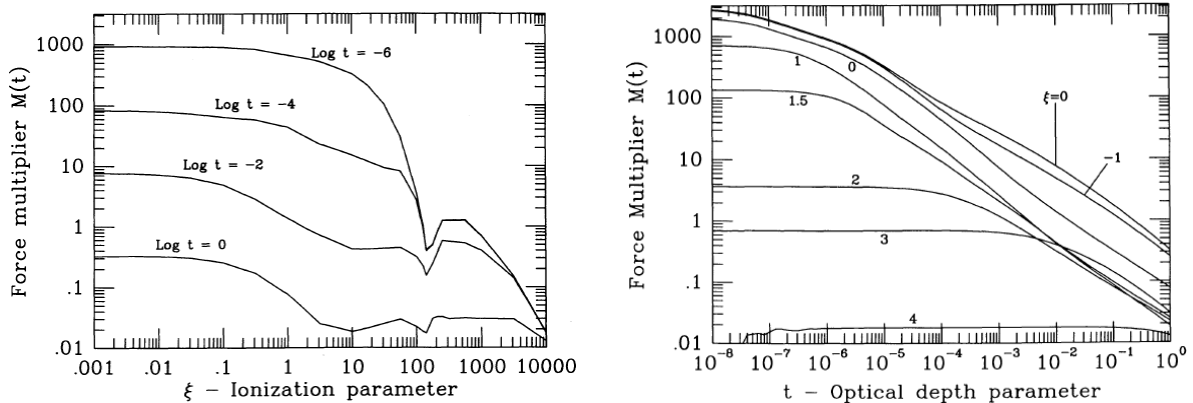


Figure 1.9: Force multiplier,  $M(t, \xi)$ , as a function of the ionization parameter,  $\xi$  (left panel), and the local optical depth parameter,  $t$  (right panel) (Stevens & Kallman, 1990). In the left panel,  $M(t, \xi)$  shows the rapid increase for  $\xi \lesssim 100$ . The labels on each curve are the respective values of  $\log t$ . In the right panel,  $M(t, \xi)$  increases with the decrease of  $t$  and becomes nearly constant for small  $t$ . The labels on each curve show the values of  $\log \xi$ .

Species of the ions, which contribute to the line force, depend on the metallicity and the ionization state of the absorber. SK90 calculates the dependence of the force multiplier on the ionization state assuming the solar metallicity. The ionization state is estimated by using an ionization parameter defined as

$$\xi = \frac{L_X}{nr_X^2} e^{-\tau_X}, \quad (1.14)$$

where  $L_X$  is the luminosity of the X-ray,  $n$  is the number density of the absorber,  $r_X$  is the distance between the X-ray source and the absorber, and  $\tau_X$  is the optical depth for the X-ray. Here we show the results of the calculation by SK90. The left panel of Figure 1.9 shows the dependence of the force multiplier on the ionization parameter for the different local optical depth parameters,  $\log t = -6, -4, -2, 0$ . Below  $\xi = 100$ , the force multiplier rapidly increases with the decrease of the ionization parameter. The right panel of Figure 1.9 shows the dependence of the force multiplier on the local optical depth parameter,  $t$ , for various ionization parameters,  $\log \xi = -1, 0, 1, 1.5, 2, 3, 4$ . The force multiplier increases with the decrease of the local optical depth parameter and become constant for small local optical depth parameter. For the small local optical depth parameter and the small ionization parameter, the force multiplier reaches  $\sim 1000$ .

The dependence of the force multiplier on the local optical depth parameter and the ionization parameter is complicated. However, by assuming the distribution function of the absorption lines, we can describe the force multiplier as the simple function of  $t$  and

$\xi$ . Owocki et al. (1988) shows that the distribution function of the absorption lines is

$$dN = N_0 \eta^{\alpha-2} e^{-\eta/\eta_{\max}} d\eta \frac{d\nu}{\nu}, \quad (1.15)$$

where  $N$  is the number of the absorption lines,  $\eta_{\max}$  is the maximum absorption strength, and the other parameters are  $N_0$  and  $\alpha$ . We rewrite the equation (1.11) by using this distribution function as

$$\begin{aligned} M(t) &= \int dN \frac{F_c \Delta \nu_D}{F} \frac{1}{t} (1 - e^{-\eta t}), \\ &= K t^{-\alpha} \left[ \frac{(1 + t\eta_{\max})^{1-\alpha} - 1}{(t\eta_{\max})^{1-\alpha}} \right], \end{aligned} \quad (1.16)$$

where the coefficient  $K$  is

$$K = \frac{v_{\text{th}} N_0 \Gamma(\alpha)}{c (1 - \alpha)}, \quad (1.17)$$

and  $\Gamma(\alpha)$  the gamma function defined as

$$\Gamma(\alpha) = \int_0^{\infty} x^{\alpha-1} e^{-x} dx. \quad (1.18)$$

For  $t \gg 1$ , the force multiplier is approximated by  $M(t) \simeq K t^{-\alpha}$ . That means,  $\alpha$  corresponds to the gradient of the plot in the right panel of Figure 1.9, which is almost the same among different ionization parameters,  $\alpha \sim 0.6$ . The other parameters,  $K$  and  $\eta_{\max}$ , depend on the ionization parameter,  $\xi$ . The parameters  $K$  and  $\eta_{\max}$  are adjusted so that the equation (1.16) has the best fit to the plots in both panels of Figure 1.9. The best-fit parameters are plotted against the ionization parameter in Figure 1.10. For  $\xi < 100$ , the fitting functions of  $K$  and  $\eta_{\max}$  are obtained as

$$K = 0.03 + 0.385 \exp(-1.4\xi^{0.6}), \quad (1.19)$$

and

$$\log_{10} \eta_{\max} = \begin{cases} 6.9 \exp(0.16\xi^{0.4}) & \log_{10} \eta_{\max} \leq 0.5 \\ 9.1 \exp(-7.96 \times 10^{-3}\xi) & \log_{10} \eta_{\max} > 0.5. \end{cases} \quad (1.20)$$

To wrap up, the force multiplier is the function of the local optical depth parameter,  $t$ , and the ionization parameter,  $\xi$ ,

$$M(t, \xi) = K t^{-\alpha} \left[ \frac{(1 + t\eta_{\max})^{1-\alpha} - 1}{(t\eta_{\max})^{1-\alpha}} \right], \quad (1.21)$$

where  $K$  and  $\eta_{\max}$  are the function of the  $\xi$  described as the equation (1.19) and (1.20). The estimation of the line force by using the force multiplier is approximative treatment. This method is employed on the previous works that are mentioned later and our works

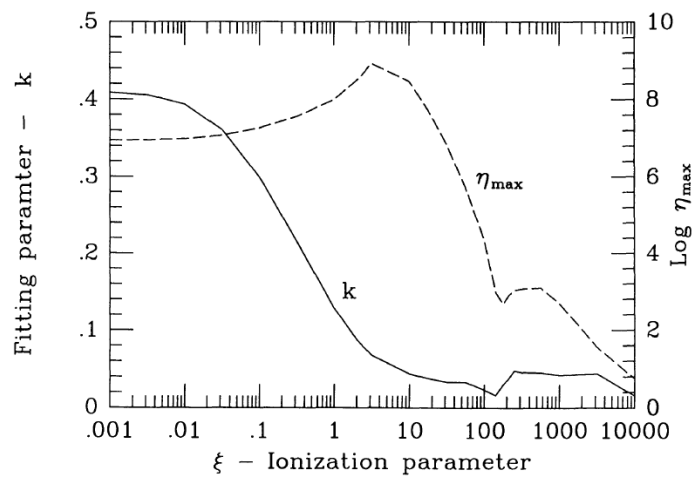


Figure 1.10: Best-fit parameters,  $k$  and  $\eta_{\text{max}}$ , against the ionization parameter,  $\xi$  (Stevens & Kallman, 1990). The solid line shows the parameter,  $k$ , and the dashed line shows the parameter,  $\eta_{\text{max}}$ .

### 1.5.3 Previous works

Line driven wind is first proposed accounting for the acceleration mechanism of the spherical stellar wind (Castor, Abbott, & Klein, 1975; Stevens & Kallman, 1990). Proga et al. (1998) and Proga et al. (1999) applied to the line-driven wind model to the disk wind around white dwarfs and performed two-dimensional radiation hydrodynamic (RHD) simulations. This RHD method has been improved and applied to the disk winds in AGNs by Proga et al. (2000) and Proga & Kallman (2004) (hereafter PK04). In their simulations, the radiation transfer of X-ray and UV is taken into consideration to estimate the line force. The UV radiation accelerates the wind by the line force. On the other hand, the X-ray suppresses the line force through the photoionization. Thus, the radiation transfer must be calculated separately.

Figure 1.11 is the resulting density map (PK04). Their result shows the funnel-shaped disk wind accelerated by the line force, of which opening angle is  $\theta \sim 70^\circ$ , where  $\theta$  is the polar angle measured from the rotation axis. The wind is launched from the disk surface several  $100R_S$  from the black hole. In the polar region, the matter with the low density falls by the gravity and makes the inflow, because metals are highly ionized by the X-ray and the line force is negligible. In the transition region between the inflow and the outflow, the line force once launches the wind since the density is large near the disk surface and the ionization parameter is enough low. However, the density decreases and the metals become ionized as the wind is accelerated and gets away from the disk. Then, the line force is made powerless and the wind returns to the disk. This “failed-wind” has an important role to attenuate the X-ray. As a consequence, behind the failed wind, the ionization state is kept low and the line force accelerates the wind. In the region of  $\theta > 70^\circ$ , the outward speed reaches  $2000 - 12,000 \text{ km s}^{-1}$  at the outer boundary of the simulation box ( $1500R_S$ ) that is consistent with the of the outflow velocity of BALs.

Risaliti & Elvis (2010) studied the line-driven disk winds in AGNs in a wide parameter space of the black hole mass,  $M_{\text{BH}}$ , and the Eddington ratio,  $\varepsilon$ , where the Eddington ratio means the ratio of the luminosity to the Eddington luminosity. They investigated the steady structures by using the non-hydrodynamic calculations, in which they solved the trajectories of the matter ejected from the disk surface without calculating the RHD equations. Figure 1.12 shows the streamlines obtained by their non-hydrodynamic method. The red lines are failed to escape the system and return to the disk because the matter is highly ionized by the strong X-ray from the vicinity of the black hole. The blue lines are successfully blown away since the ionization state of the matter is moderately due

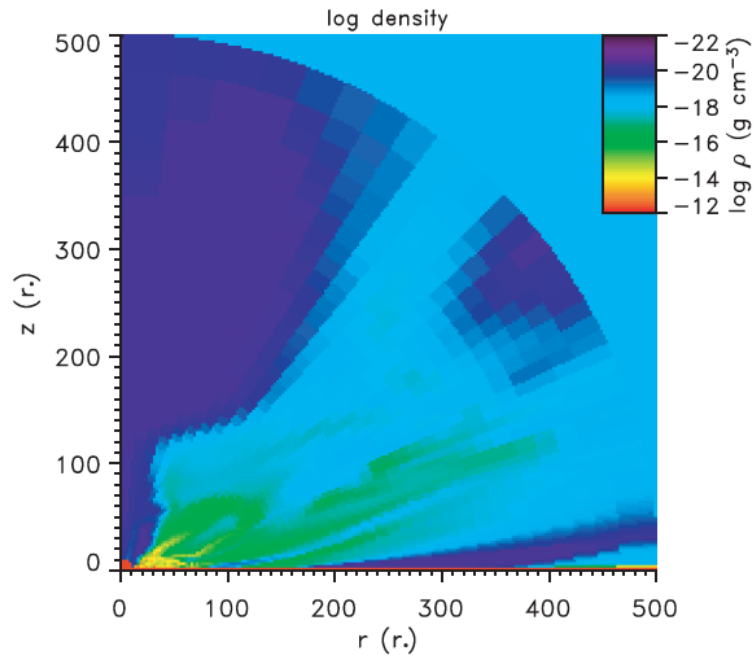


Figure 1.11: Resulting density map of the radiation hydrodynamic simulations (Proga & Kallman, 2004). The black hole is located at the origin. The accretion disk surface is equal to the  $z = 0$  plane and the  $z$ -axis is the rotational axis of the disk. The funnel-shaped disk wind of which opening angle  $\sim 70^\circ$  is launched from the disk surface several  $100R_S$  from the black hole. Here,  $r_* = 3R_S$ .

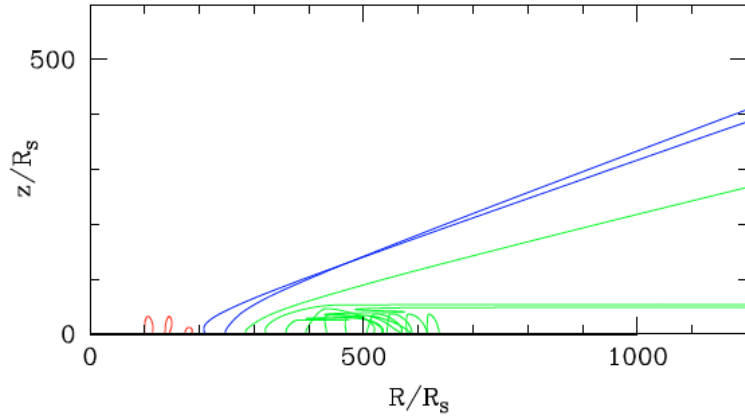


Figure 1.12: Streamlines of the line-driven disk wind calculated by the non-hydrodynamic method (Risaliti & Elvis, 2010). The black hole is located at the origin. The accretion disk is equal to the  $z = 0$  plane and the  $z$ -axis is the rotational axis of the disk. The red and green lines are failed to escape the system and return to the disk. The blue lines are successfully blown away.

to the shielding effect of red lines. The velocities of the green lines do not reach the escape velocity and the streamlines return to the disk. This is because the UV radiation is attenuated by the red and blue streamlines. The wind structure seems to be consistent with the results of the RHD simulations. They investigate the parameter range in which the disk winds are successfully launched by estimation of the outflow velocity and comparing to the escape velocity. They found that the wind is launched for  $\epsilon \gtrsim 0.2$  and  $10^8 M_\odot \lesssim M_{\text{BH}} \lesssim 10^9 M_\odot$ . This non-hydrodynamic method is a powerful tool to investigate the dependence on several unknown parameters.

To compare the theoretical model and the observation is important. To investigate whether the model can reproduce the absorption feature, it is a quite good way to calculate the synthetic spectra based on the simulations and to compare these with the observed spectra. Schurch et al. (2009) and Sim et al. (2010) calculated the X-ray spectra based on the simulations of PK04 and compared them with those of the observations.

Schurch et al. (2009) use XSCORT code that calculates the radiation transfer in the global velocity field by chaining the XSTAR code (Schurch & Done, 2007). XSTAR is the code that calculates the absorption and emission by a stationary spherical shell. They calculate the spectrum based on the results (density, temperature and radial velocity) of PK04 considering the energy-dependent absorption by lines and the Compton chattering. The X-ray source is assumed to be the point source at the center and the input spectrum is a power-law continuum. The resultant spectra are shown in Figure 1.13. The black line

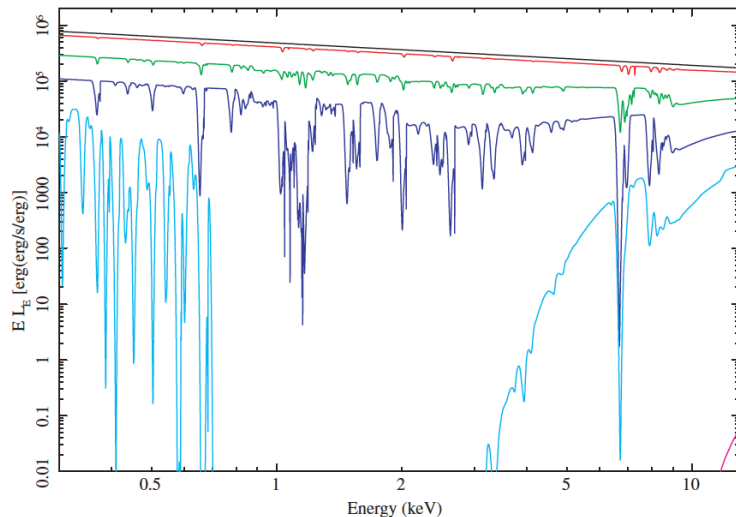


Figure 1.13: Synthetic spectra based on the result of PK04 (Schurch et al., 2009). The black line is the input spectrum. Red, green, blue, cyan, and pink lines show the results for different viewing angle,  $\theta = 50^\circ$ ,  $57^\circ$ ,  $62^\circ$ ,  $65^\circ$ , and  $67^\circ$ .

is the input spectrum. Red, green, blue, cyan, and pink lines show the results for different viewing angles,  $\theta = 50^\circ$ ,  $57^\circ$ ,  $62^\circ$ ,  $65^\circ$  and  $67^\circ$ . For  $\theta = 50^\circ$ , there is no absorption feature since the density is low and the ionization parameter is high along this sight line. Along the lines of sight for the viewing angles of  $\theta = 57^\circ$ ,  $62^\circ$  and  $65^\circ$ , there is moderately ionized wind whose ionization parameter is  $\log \xi = 3.5 - 4.5$ . As a consequence, the absorption lines appear in the spectra. At the viewing angle of  $\theta = 67^\circ$ , the column density is large,  $N_{\text{H}} > 10^{25} \text{ cm}^{-2}$ , and the wind is Compton thick. Thus, the input spectrum is almost totally attenuated by the Compton scattering. This is the reason why the pink line is only seen in the bottom right corner of Figure 1.13. Absorption lines appearing around 7keV are made from blueshifted and highly ionized Fe (FeXXV). These absorption lines are quite similar to those observed in NGC3516 (Turner et al., 2008). So they conclude that the line-driven wind model can reproduce the X-ray absorption features.

They also investigate the time variability of the absorption features by calculating the spectra based on the resulting snapshot of the simulations for the different times. The variability of the spectra is ascribable to the time variability of the key parameters in the calculation of the radiative transfer, such as the column density and the ionization parameter. When the ionization parameter of the matter is high along the line of sight, no absorption feature appears in the spectrum. The absorption features become strong with the increase of the column density of the moderately ionized matter. By their calculations, the variability whose time scale is in the range from several weeks to months is found. The

variability of the absorption lines whose time scale is similar to their result is founded by the observation, but more detailed analysis and discussion are needed to clear the origin of the variability.

Sim et al. (2010) also calculated the synthetic X-ray spectra based on the result of PK04 by Monte Carlo simulations. In addition to the energy dependent line absorption and attenuation by the Compton scattering, the line emission and scattered photons are considered in their simulations. Therefore, more realistic X-ray spectra including the emission features are obtained. The absorption features are consistent with those calculated by Schurch et al. (2009).

The two papers introduced above are the calculations of the X-ray spectra. Recently, Higginbottom et al. (2013) calculates synthetic UV spectra for the disk wind. This calculation is not based on the result of the hydrodynamic simulations, but they assume the kinematic model of the disk wind. They suppose the biconical disk wind. Based on this kinematic model, they calculate the UV spectra by using PYTHON, the radiation transfer code for UV. When the line of sight passes through the upper part of the wind, many blueshifted absorption lines of the various ions, such as CIV and SiIV, appear in the spectrum. The disk wind model is the feasible model not only to reproduce the X-ray absorption features but also BALs in the UV spectra.

## 1.6 Motivations and aim of this work

The blueshifted absorption lines are not reproduced by the unified model of the AGNs and suggest the outflow. However, the origin of the outflow is still unknown. BALs and UFOs are observed in  $\sim 20\%$  of the quasars and about half of the Seyfert galaxies respectively. Thus, such outflows are ubiquitous phenomena and we have to establish the new model or modify the unified model to explain the outflow. The phenomenological disk wind model is proposed, but the acceleration mechanism is the remaining problem. The research of the disk wind is important not only to explain the origin of the absorption lines but also to understand other phenomena around the AGNs. The outflows, especially UFOs that have large kinematic energy potentially have an influence on the star formation in the host galaxy. In addition, the large mass outflow rate is likely to have an impact on the mass accretion process and the growth of the super massive black hole. As we introduced in the previous section, the line-driven disk wind is the most plausible model because this model explains the acceleration and ionization state of the wind at one time. In this paper, we focus on this model. The previous works find that the line force successfully accelerates the disk wind.

Risaliti & Elvis (2010) studied the steady structure of the disk wind in a wide parameter range of the black hole mass and the Eddington ratio, but they did not research the wind properties, such as the ionization parameter, the velocity and the column density along the line of sight. In addition, the density and the velocity at the base of the wind (at the disk surface) are treated as free parameters and simply assumed to be independent of the distance from the black hole.

Therefore, one of the aims of our research is to investigate the conditions under which the line-driven disk wind model can reproduce the absorption features of the BALs by employing the wide range of the parameters of the black hole. We calculate the steady structure of the wind by using non-hydrodynamic method (calculation of the streamlines of the wind) that is almost same as Risaliti10. After that, we compare the resulting ionization parameter, outflow velocity and column density to those obtained from the observations. Here, we employ a more realistic density and velocity at the base of the wind based on the stellar wind theory proposed by CAK75.

Proga et al. (2000) and PK04 performed the radiation hydrodynamic simulations and research the time dependent structure of the line-driven disk wind. However, they focused on the wind for typical one parameter set of the black hole mass and the Eddington ratio. Also, the comparison between the synthetic spectra and X-ray observation was performed

only for the case of  $\varepsilon = 0.5$  and  $M_{\text{BH}} = 10^8 M_{\odot}$  (Schurch et al., 2009; Sim et al., 2010).

Then, another aim of this paper is that we investigate the dynamics of the line-driven disk wind by the two-dimensional radiation hydrodynamic simulations in a wide parameter range of the black hole mass and the Eddington ratio. We examine whether our results reproduce the X-ray observation of the UFOs. To research this in a wide parameter range, instead of calculation of the spectra, we simply compare the ionization parameter, the velocity and column density to those inferred from the observation. This method is almost the same as that used for the result of the non-hydrodynamic calculation.

In § 2, we investigate the steady structure of the line-driven disk wind by using non-hydrodynamic calculation (calculation of the streamlines of the wind) and compare the result with the X-ray observations of BAL quasars. Here, based on the stellar wind theory (CAK75), the density, the velocity and the height of the wind base are not constant and depend on the density from the center, the black hole mass and the Eddington ratio. In § 3, we research the dynamics and more realistic structure of the line-driven disk wind by employing two-dimensional radiation hydrodynamic simulations assuming the axial symmetry. We perform the parameter survey when we change the black hole mass and the Eddington ratio and compare the result to the X-ray observation of UFOs. Here we also discuss the time variability of the UFOs. Finally, § 4 is devoted to the conclusions of this paper.

In § 2, we describe our non-hydrodynamic method (§ 2.1), results (§ 2.2) and discussion (§ 2.3). We present the method of two-dimensional hydrodynamic simulations (§ 3.1), results of the calculation (§ 3.2) and discussion (§ 3.3) in § 3. Finally, § 4 is devoted to the conclusions of this paper.

## 2 Non-Hydrodynamic Calculation for BAL Quasars

### 2.1 Method

#### 2.1.1 Outline

In this section, our aim is to reveal the parameter dependence of the line-driven disk wind and the origin of the dichotomy between the BAL quasar and non-BAL quasar. We study steady structures of the line-driven disk winds in the wide parameter range of the black hole mass and the Eddington ratio. After that, we compare our results with the X-ray observations of BAL quasars. This section is based on our paper, Nomura et al. (2013).

We calculate the wind by using the non-hydrodynamic method, which is basically the same as the method used by Risaliti & Elvis (2010). However, in contrast to the previous work of Risaliti & Elvis (2010), we employ a more realistic mass outflow rate based on the stellar wind theory proposed by CAK75. In addition, we perform higher resolution calculations and evaluate the ionization parameter, the outward velocity and the column density to compare them with the observational features of BAL quasars.

The steady structure of the disk winds is obtained by the calculation of the trajectories of the fluid elements (streamlines), which are ejected from the surface of the geometrically thin and optically thick disks (Shakura & Sunyaev, 1973). To get each streamline, we solve the equation of motion considering the line force, and the mass conservation along the streamline. We also calculate the radiation transfer of the X-ray from the vicinity of the black hole and the UV radiation emitted at the inner part of the disk to calculate the ionization state, the temperature. By using these values, we evaluate the line force. We show the schematic picture for our method in Figure 2.1. To take into consideration the attenuation of the radiation by the wind itself, we calculate the streamlines in order of the distance from the black hole. When we solve the  $i$ -th streamline, we evaluate the extinction of radiation via every inner streamline of  $j$ -th ( $j < i$ ) as well as the self-shielding by the  $i$ -th flow. The overall structure of the wind appears after calculating the final (outermost) streamline.

Next, we calculate the ionization parameter, the outward velocity and the column density of the resulting disk wind for a wide range of viewing angle. By comparing them with those inferred from the X-ray observation of the BAL quasars, we evaluate the range of the viewing angle (i.e., the solid angle), in which our wind model is consistent with the observations. The solid angle divided by  $4\pi$  means the detection probability of a BAL quasar (hereafter, BAL probability). We calculate the BAL probability for a variety

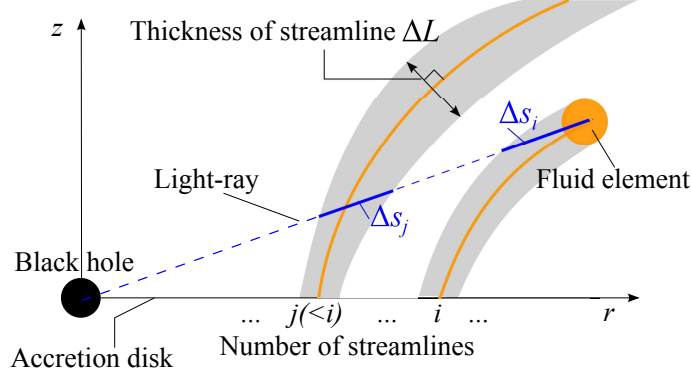


Figure 2.1: Schematic picture for our calculation method. The black hole and the accretion disk are located at the origin and the equatorial plane ( $z = 0$ ). Solid orange lines indicate the streamlines, and  $\Delta L$  is the geometrical thickness of the each flow. The length of the light ray passing through the  $j$ -th flow is  $\Delta s_j$ . When we calculate the  $i$ -th streamline, the extinction of the radiation by inner streamlines (1st, 2nd, ...,  $i - 1$ th) and by the self-shielding of the  $i$ -th flow is taken into consideration.

of the black-hole mass and the Eddington ratio and investigate the dependence of the probability on these parameters.

### 2.1.2 Initial conditions and basic equations

By solving the equation of motion including the radiation force, we investigate the trajectories (streamlines) of the fluid elements ejected from the disk surface in the cylindrical coordinate,  $(r, \varphi, z)$ . Here, the black hole and the accretion disk are located at the origin and the equatorial plane ( $z = 0$ ). We assume the system to be axisymmetric with respect to the rotation axis.

Before calculating the streamlines, we set the initial conditions: initial positions of each streamlines, density, velocity, and temperature at the initial positions. The point  $(r_0, z_0)$  is the initial position for each streamline. The first streamline is launched from the innermost radius of  $r_0 = 20R_S$ . (We note that our results do not change so much when we employ  $r_0 = 10R_S$  as the inner most radius.) The interval of the initial positions in the  $r$ -direction is set to be  $\Delta r_0 = 8R_S$  and the total number of the streamlines is 81. (We confirmed that the wind structure does not change significantly if we set the interval to be  $\Delta r_0 = 2R_S$ .) That is, the initial position in  $r$ -direction of the  $i$ -th streamline is  $20R_S + 8(i - 1)R_S$ , and the final fluid element is launched at the radius of  $r_0 = 660R_S$ . The initial altitude,  $z_0$ , is assumed to be the disk surface of the accretion disk. Then,  $z_0$

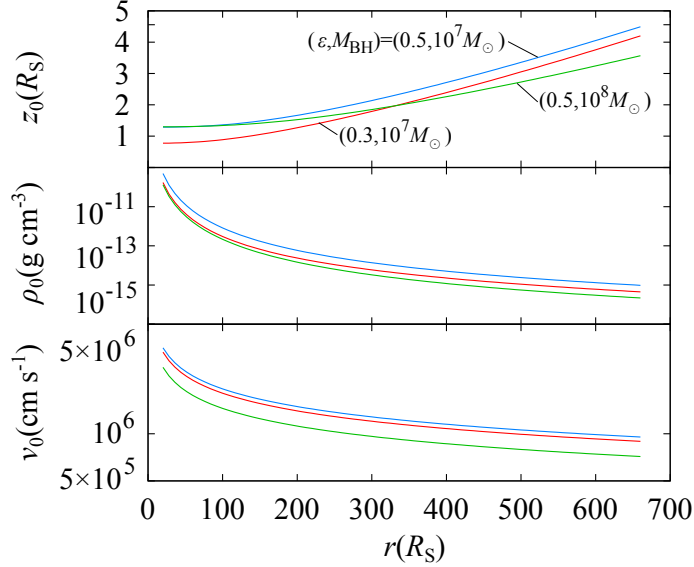


Figure 2.2: Radial profile of the initial altitude (top panel), the initial density (middle panel), and the initial upward velocity (bottom panel) are plotted for  $\varepsilon = 0.3$  and  $M_{\text{BH}} = 10^7 M_{\odot}$  (red line), for  $\varepsilon = 0.5$  and  $M_{\text{BH}} = 10^7 M_{\odot}$  (blue line), and for  $\varepsilon = 0.3$  and  $M_{\text{BH}} = 10^8 M_{\odot}$  (green line).

is derived from the hydrostatic balance in the vertical direction,

$$\frac{GM_{\text{BH}}z_0}{r_0^3} = \frac{c_s}{z_0} + \frac{\sigma_e}{c}\sigma T_{\text{eff}}^4, \quad (2.1)$$

where  $G$  is the gravitational constant,  $c_s$  is the sound speed of the gas at the mid-plane ( $z = 0$ ),  $\sigma_e$  is the mass-scattering coefficient for free electrons,  $c$  is the speed of light,  $\sigma$  is the Stefan-Boltzmann coefficient, and  $T_{\text{eff}}$  is the effective temperature. The left-hand side is the gravity of the central black hole in the vertical direction, the first term and the second term of the right-hand side are the gas pressure and the radiation force.

In the top panel of Figure 2.2,  $z_0$  is shown as a function of the accretion disk radius,  $r$ , normalized by  $R_S$ , where we employ the alpha viscosity parameter of 0.1. The blue, red and green lines show  $z_0$  for  $(\varepsilon, M_{\text{BH}}) = (0.5, 10^7 M_{\odot})$ ,  $(0.3, 10^7 M_{\odot})$ , and  $(0.5, 10^8 M_{\odot})$ . We find that  $z_0$  becomes large for the large Eddington ratio (mass accretion rate), and becomes small for the large black hole mass.

The horizontal and azimuthal components of the velocity are assumed to be null and the Keplerian velocity at the wind-base ( $r = r_0, z = z_0$ ). We set the initial velocity in the vertical direction,  $v_0$ , and the initial density,  $\rho_0$ , so as to meet the prescription of CAK75 in which they investigated the steady and spherical stellar wind accelerated by line force. They show that the resultant mass outflow rate per unit surface at the distance of  $R$  is

specified by the mass of the star,  $M_*$ , and the Eddington ratio of the star,  $\Gamma$ ,

$$\begin{aligned} \dot{m}_{\text{CAK}} = & \frac{1}{\sigma_e v_{\text{th}}} \frac{GM_*}{R^2} \alpha (1 - \alpha)^{(1-\alpha)/\alpha} \\ & \times (k\Gamma)^{1/\alpha} (1 - \Gamma)^{-(1-\alpha)/\alpha}, \end{aligned} \quad (2.2)$$

where  $v_{\text{th}}$  is the thermal speed of the gas, and  $\alpha$  ( $\sim 0.6$ ) and  $k$  ( $\sim 0.03$ ) are the constants related to the line force [see equation (21) of CAK75]. To apply the above relation to the mass outflow rate from the disk surface, we make minor revisions. Thinking about the disk wind, the gravity source is the central black hole instead of the star in CAK75 and the surface of the accretion disk is corresponding to the photosphere of the star. Then the gravity,  $GM_*/R^2$ , is replaced by  $GM_{\text{BH}}z_0/r^3$ , which is the gravity at the wind base. We use the local Eddington ratio that is the ratio of the radiation force and the gravity in the vertical direction at the distance  $R$ ,

$$\Gamma' = \frac{\sigma_e \sigma T_{\text{eff}}^4 / c}{GM_{\text{BH}}z_0 / R^3} = \frac{3\varepsilon}{4\eta z_0 / R_S}, \quad (2.3)$$

as a substitute for  $\Gamma$ . As a result, we have

$$\begin{aligned} \rho_0 v_0 = & \frac{1}{\sigma_e v_{\text{th}}} \frac{GM_{\text{BH}}z_0}{r^3} \alpha (1 - \alpha)^{(1-\alpha)/\alpha} \\ & \times (k\Gamma')^{1/\alpha} (1 - \Gamma')^{-(1-\alpha)/\alpha}. \end{aligned} \quad (2.4)$$

If we set the initial velocity, we can derive the initial density from the above relation. That is, in our study, the initial density is not a free parameter. We assume that the vertical component of the initial velocity is the sound velocity at the disk surface,  $v_0 = (k_B T_{\text{eff}} / \mu m_p)^{1/2}$ , where  $k_B$  is the Boltzmann constant,  $\mu$  ( $= 0.5$ ) is the mean molecular weight, and  $m_p$  is the proton mass. In Figure 2.2, the middle panel shows the initial density,  $\rho_0$ , given by the equation (2.4), and the bottom panel shows the initial velocity,  $v_0$ . The meaning of the line color is the same as the top panel.

We apply the CAK75 relation to set the density and the velocity at the disk surface, but they are still unknown. For example, the mass outflow rate might be enhanced if the magnetic pressure force cooperates for launching the disk wind. High resolution radiation magneto hydrodynamic simulations are needed to clear this point. It is left as an important future work.

The equation of motion including the line force,

$$\frac{d\mathbf{v}}{dt} = -\frac{GM_{\text{BH}}\mathbf{R}}{R^3} + \frac{l^2\mathbf{r}}{r^4} + \frac{\sigma_e(\mathbf{F}_{\text{UV}} + \mathbf{F}_{\text{X}})}{c} + M\frac{\sigma_e\mathbf{F}_{\text{UV}}}{c}, \quad (2.5)$$

where  $\mathbf{v} = (v_r, v_\varphi, v_z)$  is the velocity,  $\mathbf{R}$  is the point vector of the fluid element,  $l$  is the specific angular momentum,  $\mathbf{F}_X$  and  $\mathbf{F}_{UV}$  are the X-ray flux and the UV flux, and  $M$  is the force multiplier (see § 1.5.2). The radiation force due to electron scattering is the third term of the right-hand side and the line force is the final term. The gas pressure is neglected in this method, and is taken into consideration in the radiation hydrodynamic simulations (see § 3).

We assume that the density of the fluid element changes according to the mass conservation equation along the streamline. Our speculation is that the fluid element is launched from the disk surface perpendicularly (vertical phase), and is then directed away from the central source (outward phase). The geometrical thickness of the each streamline ( $\Delta L$ , see Figure 2.1), which is measured perpendicularly to the streamline on the  $r$ - $z$  plane, is kept constant ( $\Delta L = \Delta r_0$ ) while the wind is accelerated perpendicularly. When the wind is blown outward, we assume that the geometrical thickness of the streamline increases following the simple rule,  $\Delta L \propto r$ . Then the evolution of the geometrical thickness can be described as  $\Delta L = (r/r_0)\Delta r_0$  both in the vertical and outward phases. The density is derived from the mass conservation equation ( $2\pi r \Delta L \rho |v| = \text{const}$ ) as

$$\rho(v_r^2 + v_z^2)^{1/2} r^2 = \text{const}. \quad (2.6)$$

For comparison, we apply the other model, in which the geometrical thickness of the streamline,  $\Delta L$ , is kept constant even in the outward phase,  $\Delta L = \Delta r_0$ . In this model, the density is given by the mass conservation equation,  $\rho(v_r^2 + v_z^2)^{1/2} r = \text{const}$ . We note that the result is nearly independent of the models of the wind geometry. In the latter model, the density of the wind is relatively large in the distant region ( $r \gg r_0$ ). Thus, the maximum of the ionization parameter becomes smaller than that of the former model. However, a large fraction of the moderately ionized region appears where the flow is vertical to the disk ( $r \sim r_0$ ) in both cases. Then, the resultant BAL probability is almost independent from the difference of the wind geometry.

### 2.1.3 Radiative fluxes of X-ray and ultraviolet

The line force depends on the frequency of the radiation. However, it is too difficult to calculate the radiation transfer for all frequency with the calculation of the streamlines at the same time. As the simple treatment, we divide the radiation into UV and X-ray. As we mentioned in the introduction, metals absorb UV radiation through the bound-bound transition. On the other hand, the X-ray radiation ionizes the metals. So we have to

separate the radiation into at least two colors, UV and X-ray.

The luminosities of X-ray ( $L_X$ ) and UV ( $L_{UV}$ ) are described as  $L_X = f_X \varepsilon L_{\text{Edd}}$  and  $L_{UV} = (1 - f_X) \varepsilon L_{\text{Edd}}$ . Here,  $f_X$  is the ratio of the X-ray luminosity to the total luminosity,  $L_X / (L_X + L_{UV})$ ,  $\varepsilon$  is the Eddington ratio of the system defined as  $\varepsilon \equiv (L_X + L_{UV}) / L_{\text{Edd}}$ , and  $L_{\text{Edd}}$  is the Eddington luminosity. In this study,  $\varepsilon$  is a free parameter and  $f_X$  is fixed at  $f_X = 0.15$ , the typical value for quasars. Recently, Morabito et al. (2013) reported that the BAL quasars have the weaker X-ray source intrinsically than the non-BAL quasars. Then the calculation for the different  $f_X$  is one of the important works, but in this paper,  $f_X$  is fixed.

The X-ray source in the quasar is thought to be the corona that is located near the central black hole, although the exact location and extent of the X-ray source are still hot debated issues. Here we assume that the X-ray radiation is emitted from the vicinity of the black hole, and treat the X-ray source as the central point source. Thus, X-ray radiation is spherical symmetry and the radial component of the X-ray flux is

$$F_X^R = \frac{L_X}{4\pi R^2} e^{-\tau_X}, \quad (2.7)$$

where  $\tau_X$  is the optical depth for the X-ray measured from the origin. The remaining components of the X-ray flux are zero. The radiation is attenuated by the disk wind. When we calculate the  $i$ -th streamline, we consider the obscuration by every inner streamline of  $j$ -th ( $j < i$ ). That is, if a light-ray from the center to the fluid element in the  $i$ -th streamline gets across the  $j$ -th streamline ( $j < i$ ), the radiation suffers from the dilution. Even if the light-ray does not get across, the  $j$ -th flow contributes to the obscuration in the case that the distance from the light-ray to the  $j$ -th streamline is less than  $\Delta L$  (see § 2.1.2). We also take into consideration the self-shielding effect, which is extinction caused by the upper stream of the  $i$ -th flow. Therefore, the optical depth is calculated by summing up the contribution from the streamline of  $j$ -th ( $j \leq i$ ),

$$\tau_X = \sum_{j \leq i} \Delta \tau_{X,j}, \quad (2.8)$$

where  $\Delta \tau_{X,j} = \rho \sigma_X \Delta s_j$ , with  $\sigma_X$  being the mass extinction coefficient for X-ray and  $\Delta s_j$  being the length that the ray passing through the  $j$ -th flow (see Figure 2.1). The mass extinction coefficient is defined by  $\sigma_X = \sigma_e$  for  $\xi \geq 10^5$  and  $\sigma_X = 100\sigma_e$  for  $\xi < 10^5$ . Here, we calculate the ionization parameter,  $\xi$ , according to the equation (1.14). Because of the photoelectronic absorption, the mass extinction coefficient is  $\sim 100$  times larger than that of the electron scattering when the ionization state is small. To calculate in the

cylindrical coordinate, we have the  $r$ - and  $z$ -components of the X-ray flux,  $F_X^r = F_X^R(r/R)$  and  $F_X^z = F_X^R(z/R)$ . The azimuthal component is zero.

We suppose that an optically thick and geometrically thin accretion disk (Shakura & Sunyaev, 1973) is the only UV radiation source. The effective temperature of the accretion disk follows the radial profile of

$$T_{\text{eff}} = T_{\text{in}} \left( \frac{r}{r_{\text{in}}} \right)^{-3/4}, \quad (2.9)$$

where  $r_{\text{in}} (= 3R_S)$  is the disk inner radius and  $T_{\text{in}}$  is the effective temperature at  $r = r_{\text{in}}$ . The radiation from the accretion disk is the multicolor black body radiation. We consider the inner region of the disk where the UV radiation is dominant. Thus, we set  $T_{\text{in}}$  to meet the condition of

$$L_{\text{UV}} = (1 - f_X) \varepsilon L_{\text{Edd}} = \int_{r_{\text{in}}}^{r_{\text{out}}} 2\pi r \sigma T_{\text{eff}}^4 dr. \quad (2.10)$$

where  $r_{\text{out}}$  is the outer radius of the UV dominated region, at which the effective temperature of the disk is  $10^4\text{K}$ . In the outer part beyond this radius, the temperature is too cold to emit UV photons effectively, and the disk luminosity is much smaller than that of the inner part. The UV flux from the disk, in which the medium above the disk is assumed to be optically thin, is calculated by

$$\mathbf{F}_{\text{thin}} = \int \frac{\sigma T_{\text{eff}}^4}{\pi} \mathbf{n} d\Omega, \quad (2.11)$$

where  $\mathbf{n}$  is the unit vector, and  $\Omega$  is the solid angle. Because the UV source is a two-dimensional disk plane, we have to measure the optical depth along the light-rays from the points on the disk surface to the fluid element. But for simplicity, we attenuate the radial component ( $R$ -component) of the UV flux in the optically thin media ( $\mathbf{F}_{\text{thin}}$ ) using the optical depth measured from the origin,

$$F_{\text{UV}}^R = F_{\text{thin}}^R e^{-\tau_{\text{UV}}}. \quad (2.12)$$

The optical depth,  $\tau_{\text{UV}}$ , is calculated by the same rule as that of the X-ray, but we use  $\sigma_e$  instead of  $\sigma_X$ . We assume that the dilution of the polar component of the UV flux is negligible,

$$F_{\text{UV}}^\theta = F_{\text{thin}}^\theta, \quad (2.13)$$

since the disk wind is expected to have the large opening angle. The azimuthal component of the flux is zero.

In numerically, we divide the surface of the accretion disk into  $256 \times 256$  small surface elements and calculate  $\mathbf{F}_{\text{thin}}$ . We check that the number of the elements is enough for the UV flux to converge.

### 2.1.4 Force multiplier

In order to calculate the line force, we employ the force multiplier,  $M$ , proposed by SK90 [see the equation (1.21) in § 1.5.2]. In their description, the force multiplier depends on the velocity gradient along the light-ray [see the equation (1.10)]. That is,  $M$  depends on the direction. However, in our calculation, the force multiplier is replaced by the value independent from the direction for suppressing the computational cost. We approximate the velocity gradient by

$$\frac{dv}{ds} = \frac{dv_1}{dl}, \quad (2.14)$$

where  $dv_1/dl$  is the velocity gradient along the streamline. This is the local value independent from the direction of the light-ray. As we will show in § 2.2.1, the fluid element is lifted up in nearly vertical direction soon after the launching from the disk (vertical phase), since the vertical radiation flux from the wind-base mainly accelerates the matter upwards. Thus, it is reasonable to replace the velocity gradient along the right-ray by that along the streamline. Subsequently, the matter is blown away in the radial direction due to the radiation from the inner part of the accretion disk (outward phase). Thus, above approximation would be valid in both vertical and outward phases.

According to the equation (1.10), the local optical depth parameter,  $t$ , also depends on the thermal velocity,  $v_{\text{th}}$ . We calculate the gas temperature by assuming that the gas is in the radiative equilibrium, since the radiative cooling/heating time scale is much smaller than the cooling timescale via the adiabatic expansion (Proga et al., 2000),

$$n^2(G_{\text{Compton}} + G_{\text{X}} - L_{\text{b,l}}) = 0, \quad (2.15)$$

where,  $G_{\text{Compton}}$  is Compton heating/cooling rate,

$$G_{\text{Compton}} = 8.9 \times 10^{-36} \xi (T_{\text{X}} - 4T), \quad (2.16)$$

$G_{\text{X}}$  is the rate of X-ray photoionization heating and recombination cooling,

$$G_{\text{X}} = 1.5 \times 10^{-21} \xi^{1/4} T^{-1/2} (1 - T/T_{\text{X}}), \quad (2.17)$$

$L_{\text{b,l}}$  is the bremsstrahlung and line cooling,

$$L_{\text{b,l}} = 3.3 \times 10^{-27} T^{1/2} + 1.7 \times 10^{-18} \xi^{-1} T^{-1/2} \\ \times \exp(-1.3 \times 10^5/T) + 10^{-24}. \quad (2.18)$$

We assume the temperature of the X-ray radiation to be  $T_{\text{X}} = 10^8 \text{K}$ , which is the same as Proga et al. (2000). By this method, the gas temperature would be underestimated in

the region with the high-density and low-ionization parameters. Thus, to avoid unlikely temperature, we set the lower limit of the gas temperature as being equal to the disk effective temperature just under the fluid element,  $T_{\min}(r, z) = T_{\text{eff}}(r)$ .

In the present work, we suppose that the force multiplier depends on the temperature through the sound speed [see the equations (1.21) and (1.10)], but another model of the force multiplier, which does not depend on the gas temperature, has been proposed by Gayley (1995). Our results do not change so much if we employ another force multiplier, since the gas temperature is almost kept around  $10^4$  K in the region where the matter is mainly accelerated.

### 2.1.5 Assessment of BAL probability

A probability of detecting BALs (BAL probability) is evaluated as follows. We investigate the ionization parameter, the outward velocity, and the column density of our resultant wind structure along lines of sight (from an observer to the central black hole). The region where the metals make the BAL absorption lines like CIV and SiIV is thought to be more distant from the center than the region where we investigate here. Thus, instead of comparing with optical/UV observations, we refer to the X-ray observational features. According to the X-ray observations of BAL quasars, the ionization parameter is reported to be  $\lesssim 500$  (Reeves et al. 2003, Gallagher et al. 2004) and several  $\times 1000$  (Braitto et al. 2006, Wang et al. 2008). The X-ray observations also reveal that the outward velocity and the column density of the wind in such lower-ionization state are larger than  $10^4 \text{ km s}^{-1}$  and larger than  $10^{23} \text{ cm}^{-2}$  (Chartas 2007 and references therein). Based on these observations, we consider three conditions to detect BALs: (A) the outward velocity of the matter with  $\xi < 100$  exceeds  $10^4 \text{ km s}^{-1}$ , (B) the column density of the matter with  $\xi < 100$  is larger than  $10^{23} \text{ cm}^{-2}$ , and (C) the column density is smaller than  $1.5 \times 10^{24} \text{ cm}^{-2}$ . The last one is added since the Compton thick objects would not be identified as BAL quasars, since the numerous electron scattering prevents photons being observed. We check these conditions along the lines of sight with the viewing angles between  $\theta = 0^\circ$  and  $90^\circ$ . If three conditions are satisfied, we recognize that the X-ray absorption features emerge in the spectra. If this is the case, our wind model could also explain the BALs in the UV band, since the X-ray absorption closely correlates to the BALs seen in the UV wavelength (Brandt et al., 2000). We calculate the solid angle,  $\Omega_{\text{BAL}}$ , in which the conditions (A), (B), and (C) are satisfied. We can get the BAL probability by dividing this value by  $4\pi$ ,  $\Omega_{\text{BAL}}/4\pi$ .

## 2.2 Results

### 2.2.1 Structure of line-driven wind

Figure 2.3 shows the steady structure of the line-driven disk wind when we set the black hole mass and the Eddington ratio to be  $M_{\text{BH}} = 10^7 M_{\odot}$  and  $\varepsilon = 0.3$  (hereafter, we call these 'baseline parameters'). The black hole is located at the origin, the equatorial plane ( $z = 0$ ) corresponds to the optically thick and geometrically thin accretion disk and the  $z$ -axis is the rotational axis of the accretion disk. The red and black solid lines are the trajectory of the fluid elements (streamlines) ejected from the surface of the accretion disk in the  $r$ - $z$  plane. The initial density, the velocity and the altitude of the streamlines at the launching points are shown by the red lines in each panel of Figure 2.2. On the red lines in Figure 2.3, the fluid elements are accelerated and attain a velocity equal to the escape velocity,  $v = v_{\text{esc}}$ , where  $v = (v_r^2 + v_{\varphi}^2 + v_z^2)^{1/2}$ , at the points of the red filled circles. The red filled circles are located just above the accretion disk surface, thus we find that the rapid acceleration occurs in the region  $\sim 10$ – $100 R_{\text{S}}$  above the disk. Once the velocity is over the escape velocity, the matters are blown away as the disk wind. In contrast, the flow velocity does not reach the escape velocity on the black lines (first and second streamlines near the origin in Figure 2.3).

In the inner region,  $r \lesssim 30 R_{\text{S}}$ , the streamlines shown by the black lines are failed to be blown away and immediately return to the disk surface (we call this 'failed wind'). In this region, the dense matter at the wind-base weakens the acceleration by the line force. This is because the force multiplier decreases with an increase of the density,  $M \propto t^{-0.6} \propto \rho^{-0.6}$ , in the lower ionization regime ( $\xi < 100$ ). Indeed,  $\xi$  is much less than 100 in this region. Therefore, the line force does not exceed the gravity and the flow is not blown away. Note that the mechanism of making the failed wind region in our result is different from that in previous works (Murray et al., 1995; Risaliti & Elvis, 2010). We will discuss the point later in § 2.3.2.

In the middle region,  $30 R_{\text{S}} \lesssim r \lesssim 350 R_{\text{S}}$ , it is found that the disk wind is successfully blown away (see red streamlines). The fluid elements ejected from the disk surface are accelerated at the right above the launching points almost perpendicularly to the disk plane, and exceed the escape velocity at the points indicated by filled circles. Subsequently, at the certain point, the flow changes the traveling direction and is blown away towards the direction with the polar angle of  $\theta \sim 45^{\circ}$ – $55^{\circ}$ . The wind structure is understood as follows. In this region, the ionization parameter is still less than 100, leading to

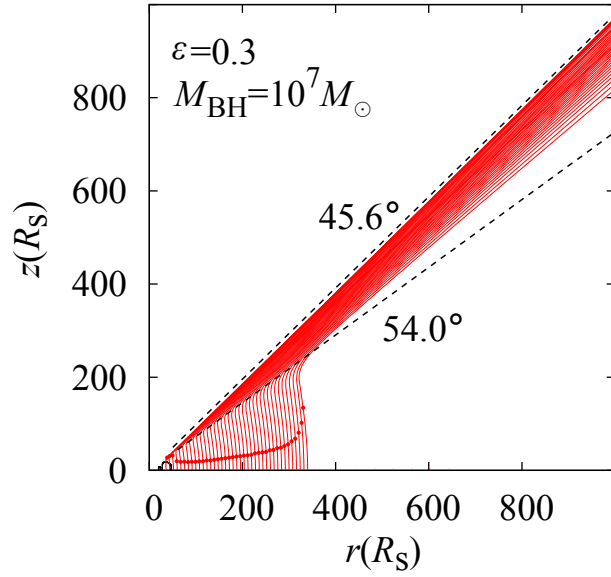


Figure 2.3: Steady structure of the line-driven disk wind for  $\varepsilon = 0.3$  and  $M_{\text{BH}} = 10^7 M_{\odot}$ . The black hole and the accretion disk are located at the origin and the equatorial plane ( $z = 0$ ). The red solid lines show the trajectories of the fluid elements (streamlines) ejected from the surface of the accretion disk. The red circles on the red lines indicate the point where the wind velocity exceeds the escape velocity. At the inner region of  $r \lesssim 30R_S$ , the ejected matter immediately goes back to the disk surface (black lines). It is also found that the wind is not launched at the outer region,  $r \gtrsim 350R_S$ , although we cannot see the streamlines in this figure. The BALs are observed at the viewing angle of  $\theta = 45.6^{\circ}$ – $54.0^{\circ}$  (between dotted-lines).

$M \propto \rho^{-0.6}$ , because the flow is shielded by the failed wind in the inner region. Since the initial density ( $\rho_0 \sim 10^{-14}$ – $10^{-13}$  g cm $^{-3}$ ) is smaller in this region than in the inner region, the force multiplier becomes large ( $M \propto \rho^{-0.6}$ ), typically several  $\times 100$ . Thus, the vertical component of the radiation force including the line force is stronger than the gravity. In contrast, the radiation from the inner region of the accretion disk is attenuated strongly by the high-density failed wind. Thus, the radial component of the radiation force cannot play an important role. As a consequence, the flow is accelerated in the vertical direction by the radiation from the disk just under the fluid element. Such a situation changes at the point of  $\theta \sim 55^\circ$ . When the polar angle is smaller than  $\sim 55^\circ$ , the radiation from the inner accretion disk, which works to accelerate the matter outward, increases with a decrease of the polar angle, because the failed wind does not dilute the radiation in this direction. Therefore, the radial component of the radiation force bends the streamlines in the outward direction and the funnel-shaped wind appears.

In the outer region,  $r \gtrsim 350R_S$ , the disk around the wind base does not effectively emit UV photons, since the temperature of the accretion disk is less than  $10^4$  K. Then, the fluid elements are not lifted up in this region. In addition, the UV radiation from the inner region of the accretion disk is obscured by the failed wind ( $r \lesssim 30R_S$ ) and the disk wind ( $30R_S \lesssim r \lesssim 350R_S$ ). Thus, although the initial density as well as the ionization parameter is small, the line force is made powerless and the disk wind cannot be ejected.

We investigate viewing angles for which the X-ray absorption features of the BAL quasars are observed and the BAL probability according to the method mentioned in §2.1.5. We investigate the ionization parameter, the outward velocity, and the column density along the light-rays based on the result for baseline parameters. It is found that the conditions (A), (B), and (C) are satisfied at the viewing angles from  $\theta = 45.6^\circ$  to  $54.0^\circ$ . That is, the absorption features are observed, since the lower-ionization matter with the sufficient radial velocity obscures the nucleus. The BAL probability is obtained as  $\Omega_{\text{BAL}}/4\pi = \cos(45.6^\circ) - \cos(54.0^\circ) \sim 11\%$ .

The reason why the BAL features are not observed when the viewing angle is smaller than  $45.6^\circ$  is that there is no wind between the observer and the nucleus. When the viewing angle is between  $54.0^\circ$  and  $63.0^\circ$ , the column density is large,  $N_{\text{H}} > 1.5 \times 10^{24}$  cm $^{-2}$ , and the system is observed as the Compton thick object. This is because the failed wind, of which the density is very high, obscures the nucleus. Thus, although the conditions (A) and (B) are satisfied, the condition (c) is unsatisfied and the object is not identified as the BAL quasar. For large viewing angle,  $\theta > 63.0^\circ$ , neither the condition (A) nor (C)

Table 2.1: The BAL probability (%)

		Black hole mass ( $M_{\text{BH}}/M_{\odot}$ )					
		$10^7$	$10^{7.5}$	$10^8$	$10^{8.5}$	$10^9$	$10^{9.5}$
Eddington ratio ( $\varepsilon$ )	0.9	7	7	7	5	0	0
	0.7	8	8	7	6	0	0
	0.5	9	9	8	8	0	0
	0.3	11	11	11	9	7	0
	0.01	0	0	0	0	0	0

is satisfied.

### 2.2.2 BAL probability

Table 2.1 presents the BAL probabilities. For  $\varepsilon = 0.3$ – $0.9$  and  $M_{\text{BH}} = 10^7$ – $10^{8.5}M_{\odot}$ , we find that the BAL probabilities are 5–11% and are not so sensitive to the black hole mass as well as the Eddington ratio. On the other hand, the BAL quasars are not observed (BAL probability is null) in the case of  $M_{\text{BH}} \gtrsim 10^9M_{\odot}$  or  $\varepsilon \lesssim 0.01$ .

**Eddington ratio dependence** — First we focus on the Eddington ratio dependence. For  $\varepsilon = 0.01$ , the radiation force is too weak to accelerate the wind. Since the wind is not successfully launched, the BAL features are not observed. The BAL probability is almost the same in the range of  $\varepsilon = 0.3$ – $0.9$ , when the black hole mass is  $M_{\text{BH}} = 10^7$ – $10^{8.5}M_{\odot}$ . This is understood by comparing the wind structure between two systems employing the different Eddington ratios. The left panel of Figure 2.4 is the same as Figure 2.3, but for  $\varepsilon = 0.5$ . We find that the wind launching region broadens as an increase with  $\varepsilon$ . However, the opening angle and the thickness of the funnel-shaped wind do not change from the case of  $\varepsilon = 0.3$ . This is the reason why the BAL probability is roughly independent of the Eddington ratio.

The opening angle reflects the changes of the initial conditions and the disk luminosity. Because these values change with  $\varepsilon$ , here, we first consider an influence of the initial density on the wind structure. For this purpose, we employ the initial density profile for  $\varepsilon = 0.5$  (blue line of the middle panel of Figure 2.2), but other initial conditions and the disk luminosity remain at the values for  $\varepsilon = 0.3$  (red lines of the top and bottom panels of Figure 2.2). The resultant streamlines are plotted by purple lines in the right panel of Figure 2.4 [case (a)]. We find that the disk wind has a wide opening angle ( $\theta \sim 65^\circ$ ). The initial density increases as an increase of  $\varepsilon$  (see Figure 2.2), and the line force is less

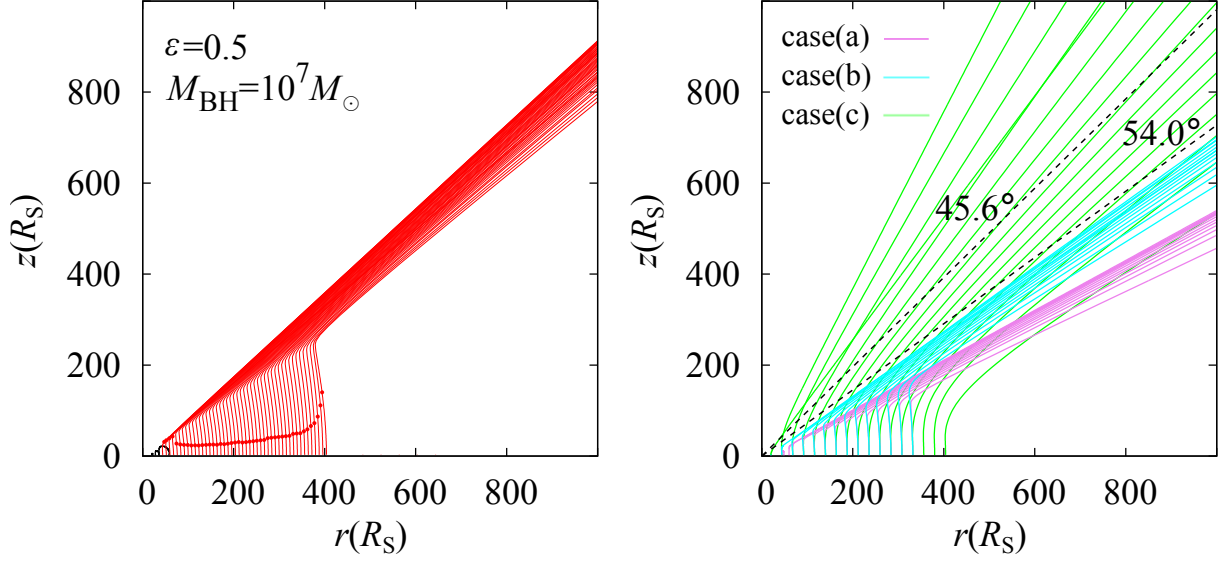


Figure 2.4: Same as Figure 2.3, but for  $\varepsilon = 0.5$  (left panel). The disk structure is almost same with Figure 2.3, although the larger Eddington ratio is employed. The right panel is also the same as Figure 2.3, but we employ the initial altitude for  $\varepsilon = 0.5$  [case (a)], the initial density for  $\varepsilon = 0.5$  [case (b)], and the disk luminosity for  $\varepsilon = 0.5$  [case (c)]. The larger initial altitude and density work to increase the opening angle of the funnel-shaped wind. In contrast, the larger luminosity tends to accelerate the matter upward.

effective for the matter with large density ( $M \propto \rho^{-0.6}$ ). The weak radiation force makes the height of the failed wind small, and the streamlines of the disk wind bend at the small altitude for the case (a) in comparison with the case with the baseline parameters. As a consequence, the higher density tends to make the opening angle of the disk wind larger.

Next, we consider an influence of change of the initial altitude,  $z_0$ . The blue lines of the right panel of Figure 2.4 show the result for the case (b) in which we employ the initial altitude for  $\varepsilon = 0.5$  (blue line of the top panel in Figure 2.2) although the luminosity, initial density, and velocity are the values for  $\varepsilon = 0.3$  (red lines of the middle and bottom panels in Figure 2.2). The initial altitude,  $z_0$ , is larger than that for the baseline parameters and this means that the initial position is distant from the disk surface. Because of this effect, the radiation force becomes relatively small and the disk wind with the large opening angle is generated. As we have discussed above, the less effective radiation force makes the height of failed wind low and forms the disk wind with the large opening angle.

Lastly we discuss the effect of the disk UV luminosity. The large disk luminosity tends to lift up the wind and narrow the opening angle. The green lines [case (c)] show the streamlines when the radiation field is calculated by assuming  $\varepsilon = 0.5$  and initial conditions remain at the values for  $\varepsilon = 0.3$  (red lines in Figure 2.2). Comparing with

the streamlines for  $\varepsilon = 0.3$  (Figure 2.3), the wind is blown away more upward and the thickness of the funnel is more broad. This is because the high Eddington ratio of the disk UV luminosity induces the strong line force. Also, because the large Eddington ratio makes the UV emitting region ( $T_{\text{eff}} \geq 10^4$  K) wide, the wind launching region expands.

To sum up, the increase of the luminosity, which contributes to reduce the opening angle of the wind, counteracts the effect to expand the funnel by the increase of the initial density and altitude. As a result, the opening angle of the funnel is insensitive to the change of the Eddington ratio and the BAL probability is roughly constant for  $\varepsilon = 0.3\text{--}0.9$ . Here, we note that the initial velocity has little influence on the wind structure.

**Black hole mass dependence** — The BAL probability is roughly constant between the range of  $M_{\text{BH}} = 10^7\text{--}10^{8.5}M_{\odot}$ , but tends to be null for  $M_{\text{BH}} \gtrsim 10^9M_{\odot}$ . The cause of the constant BAL probability is that the opening angle is not so sensitive to the black hole mass like the discussion of the Eddington ratio dependence. The streamlines for  $M_{\text{BH}} = 10^8M_{\odot}$  and  $\varepsilon = 0.5$  are shown in Figure 2.5. It is found that the launching region measured in a unit of  $R_{\text{S}}$  shrinks, but the opening angle is comparable or slightly smaller than that for the  $M_{\text{BH}} = 10^7M_{\odot}$  (the left panel of Figure 2.4). This is because of the decrease of the force multiplier as well as the temperature of the disk. First, we consider the dependence of the force multiplier on the black hole mass. The local optical depth parameter,  $t = \sigma_e v_{\text{th}} \rho (dv_l/dl)^{-1}$ , is roughly evaluated as  $t = \sigma_e \rho_0 z_0$  near the wind-base, where we suppose  $v_{\text{th}} \sim v_0$ ,  $\rho \sim \rho_0$ , and  $dv_l/dl \sim v_0/z_0$ . Since  $z_0$  is roughly proportional to  $M_{\text{BH}}$  ( $z_0 \propto R_{\text{S}}$ ),  $\Gamma'$  is almost independent from the black hole mass [see the equation (2.3)]. We have  $\rho_0 \propto (1/v_0^2)(M_{\text{BH}}^2/r^3) \propto M_{\text{BH}}^{-3/4}$  with using the relation of  $v_0 \propto M_{\text{BH}}^{-1/8}$ . Thus, the optical depth parameter is proportional to  $M_{\text{BH}}^{1/4}$ , and we have a very weak  $M_{\text{BH}}$ -dependence of the force multiplier,  $M \propto t^{-0.6} \propto M_{\text{BH}}^{-0.15}$ . As a consequence, the force multiplier is small for the large black hole mass and this effect makes the opening angle slightly larger with increase of  $M_{\text{BH}}$ . This is the reason for the slight difference of the opening angle between the two black hole masses that we employ here ( $M_{\text{BH}} = 10^7M_{\odot}$  and  $10^8M_{\odot}$ ).

Next, we investigate the dependence of the disk temperature. According to the accretion disk model here we use, the size of the UV emitting region ( $T_{\text{eff}} > 10^4$  K) is proportional to  $M_{\text{BH}}^{-1/3}$  when the Eddington ratio is kept constant. This is the main reason why the launching region of the wind becomes small with the increase of the black hole mass.

The BAL probability becomes null for  $M_{\text{BH}} \gtrsim 10^9M_{\odot}$ , because the feasible region to

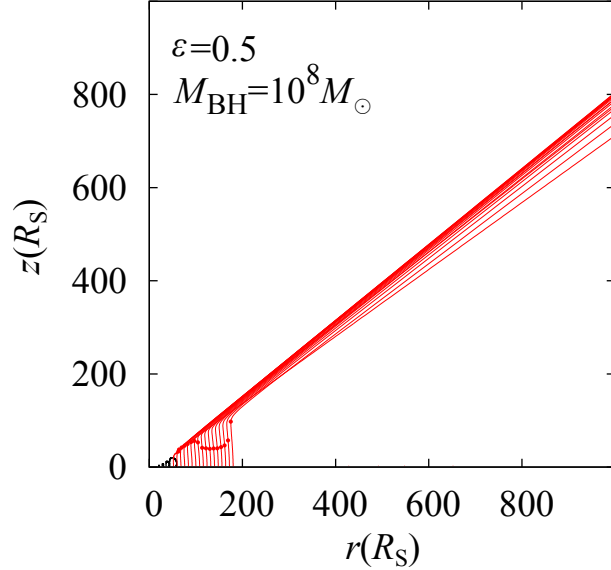


Figure 2.5: Same as the left panel of Figure 2.4, but for  $M_{\text{BH}} = 10^8 M_{\odot}$ . The opening angle of the wind does not depend on the black hole mass. However, the wind launching region shrinks with an increase of the black hole mass.

eject the wind disappears. The failed wind region slightly expands via the reduction of the line force ( $M \propto M_{\text{BH}}^{-0.15}$ ). Combined with the effect shrinking the UV emitting region, the wind launching region tends to vanish from the accretion disk when the black hole is too massive ( $M_{\text{BH}} \gtrsim 10^9 M_{\odot}$ ).

## 2.3 Discussions

### 2.3.1 Comparison with observations

Our model indicates that the BAL probability is around 10% for a wide range of the Eddington ratio and the black hole mass,  $\varepsilon = 0.3\text{--}0.9$  and  $M_{\text{BH}} = 10^7\text{--}10^{8.5} M_{\odot}$ . This percentage is roughly consistent with the abundance ratio of BAL quasars,  $\sim 10\text{--}20\%$  (e.g., Allen et al., 2011). In our calculation of the BAL probability, we do not consider the obscuration due to the torus. The BAL probability might increase if the nucleus that is obscured by the dusty torus is not identified as a quasar. For instance, the BAL probability is doubled, 10–20%, if the observer with  $\theta \geq 60^\circ$  cannot detect quasars due to the obscuration by the thick torus. Even if that is the case, our result is consistent with the percentage indicated by the observation.

In the regime of  $\varepsilon = 0.3\text{--}0.9$  and  $M_{\text{BH}} = 10^7\text{--}10^{8.5} M_{\odot}$ , the wind structures, especially the opening angles of the winds, are similar to each other. This similarity induces the almost constant BAL probability. Above result indicates that rather than the parameters

such as the black hole mass and the Eddington ratio, the observer’s viewing angle is responsible for the difference between the BAL and non-BAL quasars. The BAL features are detected when we observe the nucleus in the direction of the wind flow. If the wind does not obscure the nucleus along the line of sight or if the wind is Compton thick, the system is identified as the non-BAL quasar. This result advocates the phenomenological model (Elvis, 2000) in which the dichotomy of the BAL and non-BAL quasars is explained by the observer’s viewing angle. However, we note that the BAL features are not observed for small Eddington ratio,  $\varepsilon \lesssim 0.01$ , and large black hole mass,  $M_{\text{BH}} \gtrsim 10^9 M_{\odot}$ .

Here, is it reasonable to say that our model overestimates the BAL probability in the regime of  $\varepsilon = 0.05\text{--}0.1$ . In this regime, the resulting percentages are distributed in 20–50%, but the accurate value might be smaller than the estimation. The reason for the large BAL probability is that the thickness of the funnel-shaped wind is large for the small Eddington ratio. We show the streamlines for  $\varepsilon = 0.1$  and  $M_{\text{BH}} = 10^8 M_{\odot}$  as an example in Figure 2.6. We find that the streamlines bend toward the radial direction soon after the launching from the disk. As we explained in §2.2.2, the initial density at the wind base becomes small with the decrease of the Eddington ratio. The small density of the inner streamlines is not enough to obscure the radiation from the inner region. Thus, the flow is accelerated outward by the strong UV radiation from the inner region of the disk, before being lifted up by the radiation from just below the fluid elements. As a consequence, the wind is blown away in the wide angle and the BAL probability becomes large. The estimated BAL probability is 48%. However, we find that the mass outflow rate of the wind is a few times larger than the mass accretion rate of the accretion disk. This implies that our model overproduces the outflows, and actual BAL probability should be smaller than 48%. To avoid this inconsistency of the mass outflow rate and the accretion rate, we need to solve the wind and the accretion disk together. This is one of the important future works.

### 2.3.2 Comparison with previous works and motivations for hydrodynamic simulations

As we mentioned in §2.2.1, the origin of the failed wind region is different from Risaliti & Elvis (2010) in which they use the constant initial density, the launching velocity, and the altitude independent from the disk radius and other parameters. In the case of Risaliti & Elvis (2010), the failed wind region is formed due to the large ionization parameter in the inner region of the disk. The streamlines near the center are exposed to

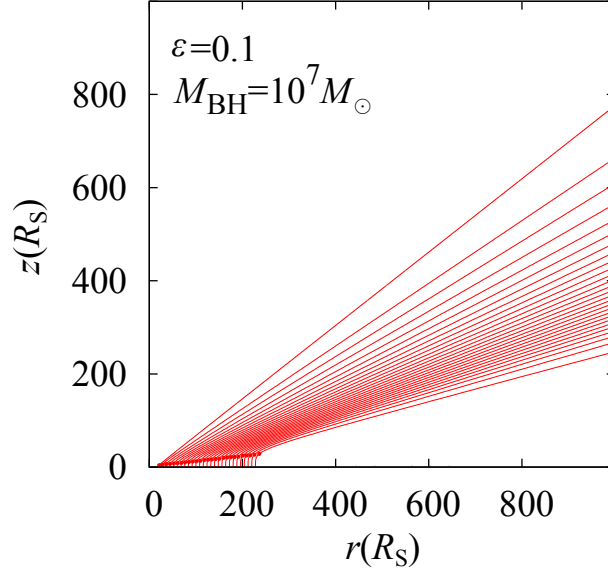


Figure 2.6: Same as Figure 2.3, but for  $\varepsilon = 0.1$ . In this case, the wind with large covering factor forms.

the strong X-ray and the ionization parameter becomes large. Thus, the line force cannot accelerate the fluid elements in this region. Murray et al. (1995) also reported that the failed wind appears in the vicinity of the black hole because of the X-ray irradiation. On the other hand, in our model, the initial density at the inner region of the disk is high ( $\rho \gtrsim 10^{-11} \text{ g cm}^{-3}$ ) because we employ the more realistic initial condition based on CAK75, which depends on the disk radius. Even if the strong X-ray irradiates the matter with high density, the ionization parameter remains small. This is the positive effect for the line force to accelerate the wind. However, the local optical depth parameter,  $t$ , becomes larger with the increase of the density [ $t \propto \rho$ , see the equation (1.10)]. This effect suppresses the line force and forms the failed wind region in our calculation. Here, we note that we can reproduce their results if we employ the same initial conditions as Risaliti & Elvis (2010). Also, our results are similar to the wind structure calculated by the hydrodynamic simulations of PK04 in terms of the opening angle, the column density of the wind in the low ionization state, and the outward velocity. By setting the initial density to be the same value as PK04, we can approximately reproduce their results.

In this section, we investigate the steady structure of the disk wind, but in reality, the disk winds are thought to have the time dependent and clumpy structure. As we have mentioned in § 1.4.2, the time variability of the absorption lines is reported by many observations. This time variability implies that the wind structure changes in time. Density fluctuation of the line-driven wind has been already reported by Owocki & Puls (1999).

They investigate the line-driven stellar wind through the one-dimensional calculations. In addition, Proga et al. (2000) also reported that the density blobs sometimes appear in the wind. In the next section, we investigate the dynamics and the more realistic structure of the wind including the time variability by the two-dimensional radiation hydrodynamic simulations.

# 3 Radiation Hydrodynamic Simulations for Line-Driven Disk Wind

## 3.1 Method

We calculate the structure and dynamics of the disk wind by two-dimensional radiation hydrodynamic simulations. The method of the calculation is almost similar to that of Proga et al. (2000) and PK04.

### 3.1.1 Basic equations and set up

The basic equations of the hydrodynamics are the equation of continuity,

$$\frac{D\rho}{Dt} + \rho\nabla \cdot \mathbf{v} = 0, \quad (3.1)$$

the equation of motion,

$$\rho \frac{D\mathbf{v}}{Dt} = -\nabla P + \rho\mathbf{g} + \rho\mathbf{f}^{\text{rad}}, \quad (3.2)$$

and the equation of energy,

$$\rho \frac{D}{Dt} \left( \frac{e}{\rho} \right) = -P\nabla \cdot \mathbf{v} + \rho\mathfrak{L}, \quad (3.3)$$

where  $\rho$  is the mass density,  $\mathbf{v}$  is the velocity,  $P$  is the gas pressure,  $e$  is the internal energy density, and  $\mathbf{g}$  is the gravitational acceleration of the central black hole.

In the final term of the equation (3.2),  $\mathbf{f}^{\text{rad}}$  is the radiation force per unit mass including the line force,

$$\mathbf{f}^{\text{rad}} = \frac{\sigma_e \mathbf{F}_{\text{UV}}}{c} + \frac{\sigma_e \mathbf{F}_{\text{UV}}}{c} M, \quad (3.4)$$

where  $\mathbf{F}_{\text{UV}}$  is the UV flux and  $M$  is the force multiplier. The first term is the radiation force due to the electron scattering and the second term is the line force. In the second term of the equation (3.3),  $\mathfrak{L}$  is the net cooling rate,

$$\mathfrak{L} = n^2(G_{\text{Compton}} + G_{\text{X}} - L_{\text{b,l}}), \quad (3.5)$$

where  $G_{\text{Compton}}$  is the rate of Compton heating/cooling,  $G_{\text{X}}$  is the rate of X-ray photoionization heating and recombination cooling, and  $L_{\text{b,l}}$  is the bremsstrahlung and line cooling. Detailed descriptions of these are shown in §2.1.4. We assume an adiabatic equation of state  $P = (\gamma - 1)e$  and consider  $\gamma = 5/3$ .

We calculate these equations in the spherical polar coordinate  $(r, \theta, \phi)$ , where  $r$  is the distance from the center,  $\theta$  is the polar angle, and  $\phi$  is the azimuthal angle. Here,

we assume axial symmetry around the rotation axis of the accretion disk ( $\theta = 0$ ). Our computational domain occupies the radial range of  $r_i = 30R_S \leq r \leq r_o = 1500R_S$  and the angular range of  $0^\circ \leq \theta \leq 90^\circ$ , same as PK04. In our calculation, the  $\theta = 90^\circ$  plane does not correspond to the mid-plane of the accretion disk. We suppose that the boundary of  $\theta = 90^\circ$  is the surface of the accretion disk. The plane of  $\theta = 90^\circ$  is placed on the height of  $z_0$  from the mid-plane of the disk, where we set  $z_0 = 4.0\epsilon R_S$ , which is roughly estimated by the hydrostatic equilibrium in the vertical direction. We assume the accretion disk is geometrically thin and optically thick standard disk (Shakura & Sunyaev, 1973). Then the interior of the disk itself is negligible and excluded our calculation box.

We divide this computational domain into grids. We prepare 100 grids for the radial range and 160 grids for the angular range. To get the good spatial resolution in the region close to the disk surface and the central black hole, we use the fixed zone size ratios,  $dr_{j+1}/dr_j = 1.05$  and  $d\theta_k/d\theta_{k+1} = 1.066$ .

### 3.1.2 Boundary conditions

We set boundary conditions as follows. We apply the axial symmetric boundary at the rotational axis of the accretion disk,  $\theta = 0^\circ$ . The outflow boundary condition is employed at the outer radial boundary. Once the outflow exits the computational domain across the outer boundary, the flow never returns. At the inner radial boundary and the boundary of  $\theta = 90^\circ$ , we apply the reflecting boundary. To keep the surface of the accretion disk in the steady state, some constrains are applied for the first grids above the disk: (1) the radial velocity is set to be zero,  $v_r = 0$ , (2) the rotational velocity is Keplerian velocity, (3) the density fixed at  $\rho = \rho_0 = 10^{-9} \text{ g cm}^{-3}$ , and (4) the temperature is fixed at the effective temperature of the standard disk surface calculated by the equations (2.9) and (2.10). These four conditions are fulfilled at all times during the simulations. By setting the density to be constant at  $\theta = 90^\circ$ , if the disk wind is launched from the accretion disk and the density becomes low above the disk, the mass is supplied by the disk surface. The more realistic condition at the disk surface should be calculated by the simulations, but this is outside the scope of our research.

### 3.1.3 Initial conditions

We assume hydrostatic equilibrium in the vertical direction, then the initial density distribution is

$$\rho(r, \theta) = \rho_0 \exp\left(-\frac{GM_{\text{BH}}}{2c_s^2 r \tan^2 \theta}\right), \quad (3.6)$$

where  $c_s$  is the sound velocity at the disk surface and  $\rho_0$  is the constant density in the first zone above the disk surface, which we mentioned in §3.1.2 and correspond to the density at the photosphere of the accretion disk. We substitute the typical value of the density at the surface,  $\rho_0 = 10^{-9} \text{ g cm}^{-3}$ . We set the initial velocity to be  $v_r = v_\theta = 0$ , and  $v_\phi = \frac{1}{\sin \theta} \sqrt{\frac{GM_{\text{BH}}}{r}}$ . The rotational velocity,  $v_\phi$ , is given to meet the equilibrium between the gravity and the centrifugal force. We also set the initial temperature distribution as follows. We assume the initial gas temperature is the same as the temperature of the accretion disk lying just under the gas,  $T(r, \theta) = T_{\text{eff}}(r \sin \theta)$ , where  $T_{\text{eff}}(r)$  is the effective disk temperature at the disk radius,  $r$ . We have already shown the specific description of  $T_{\text{eff}}(r)$  in §2.1.3.

### 3.1.4 Line force

**Radiative fluxes of X-ray and ultraviolet** — Basically, the treatment of X-ray and UV radiation is the same as the non-hydrodynamic method (see §2.1.3). The luminosities of X-ray and UV are described as  $L_X = 0.1\varepsilon L_{\text{Edd}}$  and  $L_{\text{UV}} = \varepsilon L_{\text{Edd}}$ . The ratio of the X-ray luminosity to the UV luminosity is constant throughout the present work. We assume the X-ray source as a point source at the center of the coordinate. The UV radiation source is the geometrically thin and optically thick disk whose temperature distribution is given by the equations (2.9) and (2.10). Here, the thickness of the disk is neglected and the UV radiation source corresponds to the equatorial plane. That is, the UV radiation is emitted from the  $z = -4\varepsilon R_S$  plane. We set the UV emitting region of the accretion disk by the same rule as the non-hydrodynamic method, but outer radius of UV emitting disk is set to be more large. In the non-hydrodynamic method, we set  $r_{\text{out}}$  to be the radius at which the effective temperature of the disk is  $10^4 \text{ K}$ , but in this simulation, we set  $r_{\text{out}}$  to be the radius at which the effective temperature of the disk is  $3 \times 10^3 \text{ K}$  to include the UV radiation from the outer part of the accretion disk.

We use the approximating method to calculate radiation flux. We calculate the X-ray and UV fluxes in the optically thin media before starting the hydrodynamic calculation. The X-ray radiation is spherical symmetry, and the radial component of the X-ray flux in

the optically thin media is  $F_{X,\text{thin}}^r = L_X/4\pi r^2$ . The UV flux in the optically thin media,  $F_{UV,\text{thin}}$  is calculated by the equation (2.11).

At each time step of the hydrodynamic simulations, we calculate the optical depths measured from the origin for both X-ray and UV radiation,

$$\tau_X(r, \theta) = \int_{r_i}^r \sigma_X \rho(r, \theta) dr, \quad (3.7)$$

and

$$\tau_{UV}(r, \theta) = \int_{r_i}^r \sigma_e \rho(r, \theta) dr, \quad (3.8)$$

where the definition of mass extinction coefficient,  $\sigma_X$ , is identical as that used for non-hydrodynamic method (see §2.1.3). We consider the attenuation due to the electron scattering and the photoelectronic absorption for the X-ray. The UV flux is diluted only by the electron scattering.

By using this optical depths, we attenuate the radial components of the X-ray and UV fluxes, then the resultant fluxes are  $F_X^r = F_{X,\text{thin}}^r e^{-\tau_X}$  and  $F_{UV}^r = F_{UV,\text{thin}}^r e^{-\tau_{UV}}$ . We suppose that the dilution of the angular component of the UV flux is negligible,  $F_{UV}^\theta = F_{UV,\text{thin}}^\theta$ .

**Force multiplier** — To obtain the line force, we use the force multiplier proposed by SK90 [see the equation (1.21) in §1.5.2]. By calculating the ionization parameter,  $\xi$ , and the local optical depth parameter,  $t$ , we evaluate the force multiplier at each time step. As we mentioned before (see §1.5.2 and §2.1.4), the force multiplier depends on the direction of the light-ray. However, in our simulations, the force multiplier is amended by replacing the value independent of the direction. We approximate the velocity gradient along the light-ray by the velocity gradient in the radial direction,

$$\frac{dv}{ds} = \frac{dv_r}{dr}. \quad (3.9)$$

By this approximation, the force multiplier become the regional value independent from the direction.

### 3.1.5 The code

The numerical procedure is divided into the following steps. (1) Before starting the simulations, we calculate the radiation fluxes in the optically thin media for UV and X-ray. (2) At each time step of the simulations, we calculate the optical depths measured from the center of the coordinate for the UV radiation and X-ray [see the equations (3.7) and (3.8)]. We evaluate the radiation fluxes and calculate the force multiplier as

we mentioned in §3.1.4. Then we obtain the radiation force in including the line force. (3) We calculate the equations (3.1), (3.2), and the hydrodynamic terms of the energy equation [the equation (3.3)] for ideal fluid with using HLLC scheme. Here we treat the radiation force as the external force term explicitly. The basic hydrodynamic code here we use is the same as that used in Takahashi & Ohsuga (2013), but we set the magnetic field to be zero and exclude the subroutines for the special relativistic effect and the radiation transfer. (4) After obtaining the energy equation without the net cooling term [the last term of the equation (3.3)], we calculate the temperature (i.e., internal energy of the fluid) considering the radiative heating and cooling by the implicit method. (5) If the density or the temperature is lower than the lower limit in some grids, we set the lower limits for them. The lower limit of the density is  $10^{-22} \text{ g cm}^{-3}$ . The lower limit of the temperature is  $T_{\text{eff}}(r \sin \theta)$ .

At the step (3), when we solve the hydrodynamic terms of the energy equation, we calculate the time evolution of the total energy,  $E = e + \frac{1}{2}\rho v^2$ . This method is not appropriate for the case that the velocity of the wind is very high, and the kinetic energy larger than the internal energy by several degree of magnitude (i.e.,  $E \sim \frac{1}{2}\rho v^2$ ). Then, negative pressure appears, since the pressure is given by subtracting the kinetic energy from the total energy,  $p = (\gamma - 1)e = (\gamma - 1)(E - \frac{1}{2}\rho v^2)$ . If the resulting pressure is negative, we evaluate the gas pressure from the conservation equation of entropy instead of the conservation equation for the total energy,

$$\frac{Ds}{Dt} + s\nabla \cdot \mathbf{v} = 0, \quad (3.10)$$

where  $s$  is the entropy density,  $s = p/\rho^{\gamma-1}$ .

The time step is determined by using the Courant-Friedrichs-Levi condition. At each grid, we calculate

$$\Delta t = 0.05 \frac{\min(\Delta r, r\Delta\theta)}{\sqrt{(v_r + c_s)^2 + (v_\theta + c_s)^2}} \quad (3.11)$$

where  $\Delta r$  and  $\Delta\theta$  are the grid sizes in the radial and polar directions. The minimum value of  $\Delta t$  in all grids is used as the time step.

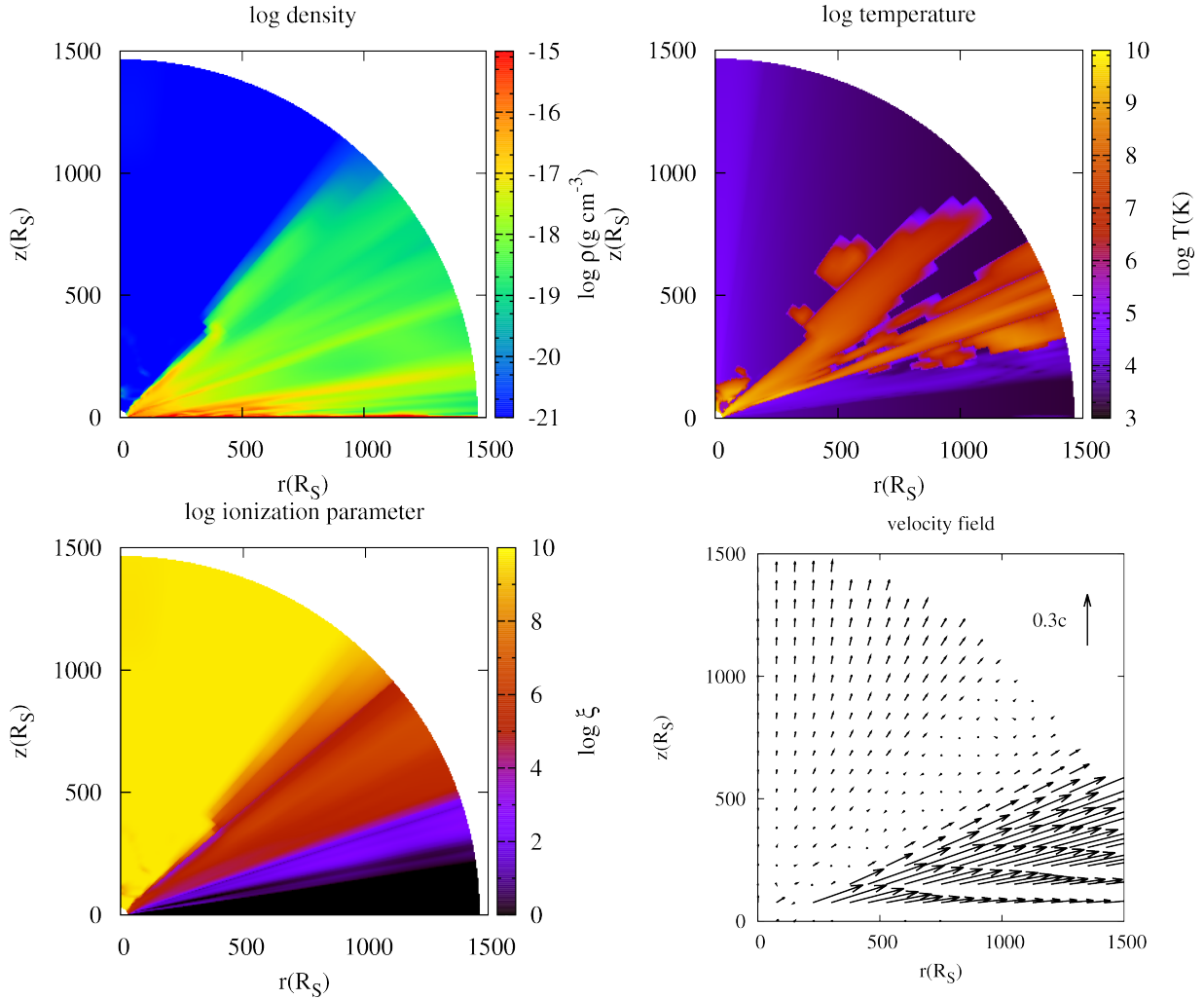


Figure 3.1: Color map of the density (top left panel), the temperature (top right panel), the ionization parameter (bottom left panel), and the map of the velocity field (bottom right panel). For all panels, the black hole is located at  $4R_S$  below the center, the equatorial plane of the accretion disk lies  $4R_S$  below the  $z = 0$  plane, and the  $z$ -axis is equal to the rotational axis of the accretion disk.

## 3.2 Results

### 3.2.1 Structure of line-driven wind

Figure 3.1 shows snapshots of the density distribution (top left panel), the temperature (top right panel), the ionization parameter (bottom left panel), and the velocity field (bottom right panel) after 6.67 yr, when we employ  $\varepsilon = 0.5$  and  $M_{\text{BH}} = 10^8 M_\odot$ . The surface of the accretion disk is corresponding to the  $z = 0$  plane of which the altitude is  $z_0 = 2R_S$  (the equatorial plane of the accretion disk is located at  $z = -2R_S$ ) and the center of this figure is located above the black hole by  $z_0$ . The  $z$ -axis is equal to the rotational axis of the accretion disk.

The disk wind is successfully launched from the accretion disk. In the region of the large polar angle,  $\theta \gtrsim 70^\circ$ , the wind is accelerated to the quite large velocity,  $0.3\text{--}0.5c$  toward the radial direction. The density is large,  $\rho \sim 10^{-16}\text{--}10^{-15} \text{ g cm}^{-3}$ , near the base of the wind (the disk surface). Behind the dense region, the ionization parameter is small,  $\log \xi \lesssim 4$ , which is suitable for the line force to accelerate the wind. This is because the dense matter shields the wind from the X-ray radiation from the vicinity of the black hole. Since the X-ray radiation is attenuated in this region, the heating effect due to the X-ray is powerless and the temperature of the wind is low,  $T \sim 10^4\text{K}$ .

In the region of  $45^\circ \lesssim \theta \lesssim 70^\circ$ , the velocity vector is partly inward. The wind once launched from the disk returns to the disk and forms the failed wind. Along the direction of  $45^\circ \lesssim \theta \lesssim 70^\circ$ , density is smaller than that near the disk surface. As a consequence, the shielding effect becomes less effective and the ionization parameter is large,  $\log \xi \sim 5$ . Because of the same reason, the matters are heated by the X-ray and the temperature rises to  $T \sim 10^8\text{K}$ .

In the polar region, the slow outflow appears because the radiation force becomes comparable with the gravitational force without the line force due to the geometrical effect, though the Eddington ratio is 0.5. The radiation force due to electron scattering is larger in the polar region because the light source is the disk. The density of this flow is very small and less than the lower limit,  $10^{-22} \text{ g cm}^{-3}$ . Therefore the matters are fully ionized,  $\log \xi \gg 6$ . In reality, no mass supply is expected from the accretion disk in this region. So in what follows, we draw little attention to this outflow.

Figure 3.2 shows the density, the outflow velocity (top panel), the ionization parameter and the column density (bottom panel) of the flow as functions of the polar angle at the outer boundary of the simulation box for the snap shot at the same time as Figure 3.1. In both panels, the ordinate on the left-hand side shows the value of the solid line. The ordinate on the right-hand side shows the value of the dashed line. The density increases in the region of  $\theta \gtrsim 40^\circ$  and reaches to the maximum value at around  $\theta \sim 82^\circ$ . The velocity is relatively small in the range of  $40^\circ \lesssim \theta \lesssim 60^\circ$  and  $v_r \sim 0$  at  $\theta \sim 50^\circ$ . The velocity rapidly increases to  $v_r \sim 0.4$  for the range of  $\theta \sim 70^\circ\text{--}80^\circ$ . The ionization parameter is  $\log \xi > 9$  for the polar region,  $\theta \lesssim 40^\circ$ , and the matters are fully ionized. The ionization parameter decreases with the increase of the angle,  $\log \xi \sim 5\text{--}6$  for  $\theta \sim 50^\circ\text{--}70^\circ$  and  $\log \xi \lesssim 4$  for  $\theta \gtrsim 70^\circ$ . The column density becomes large in the region of  $\theta \gtrsim 40^\circ$ , and this is consistent with the increase of the density. The column density is  $N_{\text{H}} \sim 10^{22} \text{ cm}^{-2}$  for a wide range,  $50^\circ \lesssim \theta \lesssim 80^\circ$ .

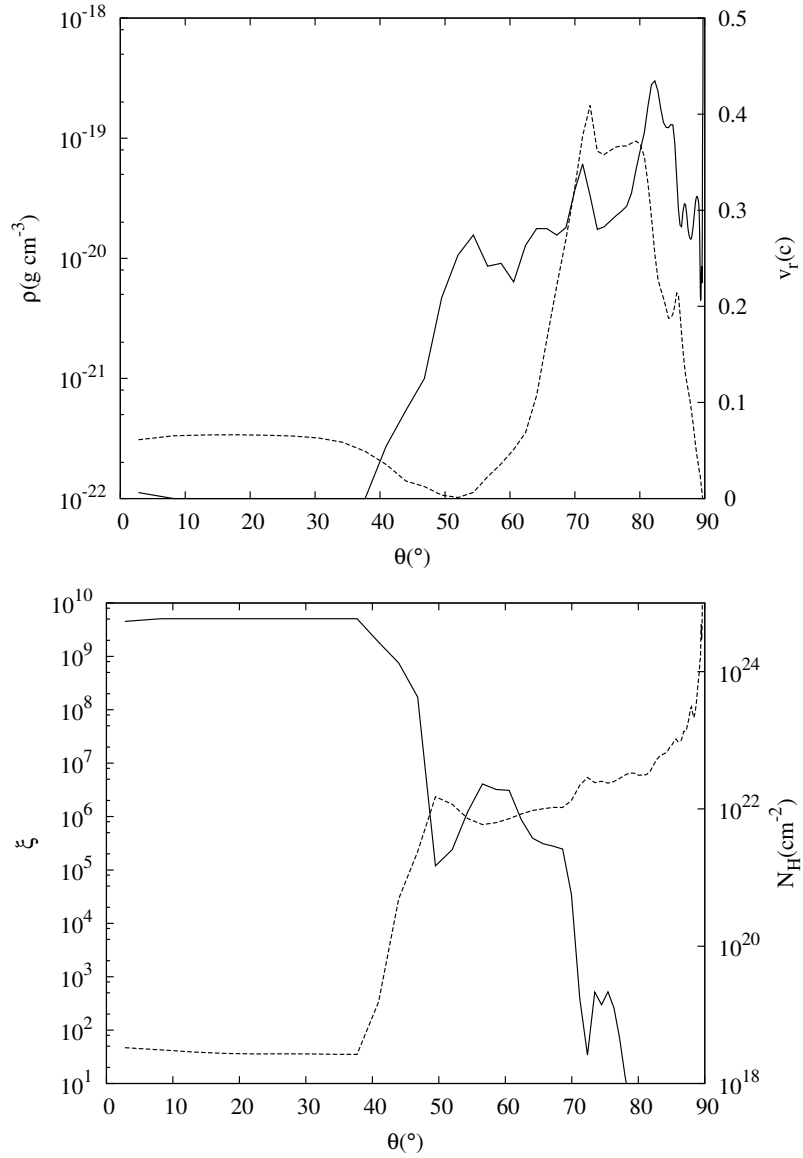


Figure 3.2: Density, outflow velocity (top panel), ionization parameter, and column density (bottom panel) of the flow at the outer boundary of the simulation box for the snapshot at the same time as Figure 3.1. In both panels, the ordinate on the left-hand side shows the value of the solid line. The ordinate on the right-hand side shows the value of the dashed line.

### 3.2.2 Mechanism of acceleration

The top panel of Figure 3.3 shows the ratio of the radiation force in the  $r$ -direction to the gravitational force in the  $r$ -direction from which the centrifugal force is subtracted,  $F_{\text{rad},r}/(F_{\text{grav},r} - F_{\text{cent}})$ . The bottom panel of the Figure 3.3 is the same as the top panel but in  $z$ -direction, but centrifugal force does not work in this direction and the ratio is  $F_{\text{rad},z}/F_{\text{grav},z}$ . These panels are close-up of the inner region of  $500R_{\text{S}} \times 500R_{\text{S}}$  using the time-averaged value from 3.34 yr to 6.67 yr. In the region,  $\theta \gtrsim 68^\circ$ , the radiation force is 10–1000 times larger than the gravitational force (gravitational force reduced by the centrifugal force in the horizontal direction). This is caused by the contribution of the line force. In this region, the ionization parameter is enough low,  $\log \xi \lesssim 4$ , for the line force to accelerate the wind. This is because the dense region near the center shields this region from the strong X-ray. This region is about the same as the region the dense disk wind is launched and blown (Figure 3.1). Therefore, we find that the wind is successfully accelerated by the line force. Accurately, wind outflows more upward than the acceleration region where the radiation force is dominant. To understand this structure and to explain the mechanism of the acceleration more precisely, we consider the two streamlines.

The two black lines in Figure 3.3 are the streamlines of the wind. The short-dashed black line launched at  $r = 60R_{\text{S}}$  goes up and travels in the region where the radiation force is larger than the gravitational force,  $F_{\text{rad},r} > (F_{\text{grav},r} - F_{\text{cent}})$  and  $F_{\text{rad},z} > F_{\text{grav},z}$ . On the other hand, the long-dashed black line launched from the region near the inner boundary of the simulation box ( $r \sim 30R_{\text{S}}$ ) travels in the acceleration region,  $F_{\text{rad},r} > (F_{\text{grav},r} - F_{\text{cent}})$  and  $F_{\text{rad},z} > F_{\text{grav},z}$ , just within several  $10R_{\text{S}}$  after the launching. However, this streamline is accelerated enough to exceed the escape velocity and blown away as the disk wind. In the region surrounded by the red lines, the velocity of the wind is greater than the escape velocity. The points where the red line and the black lines intersect show the points where the velocities of each streamlines exceed the escape velocity. In both stream lines the velocities exceed the escape velocity at  $\sim 10R_{\text{S}}$  above the disk, and this is in agreement with the result of our non-hydro dynamic calculations (see Figure 2.3).

Figure 3.4 shows the velocity and forces as functions of the distance along the streamline that is shown by the short-dashed line in Figure 3.3. The top panel of Figure 3.4 shows the velocity. The solid line indicates the horizontal component and the dashed line indicates the vertical component of the velocity. The point where the velocity exceeds the escape velocity is shown by the filled circle and the open circle on each line. The velocity of the streamline reaches the escape velocity at  $4.3R_{\text{S}}$  along the streamline after

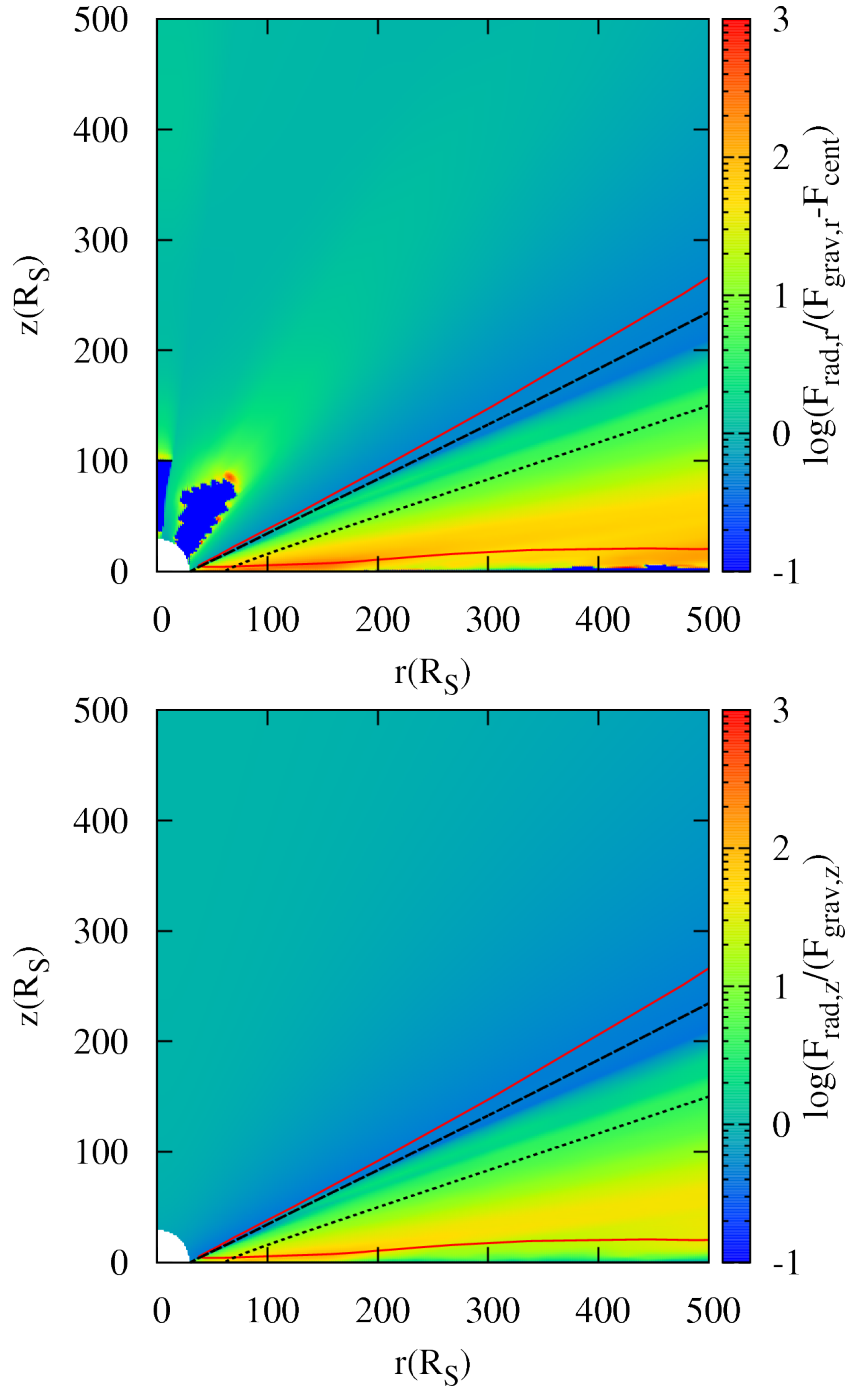


Figure 3.3: Ratio of the radiation force to the gravitational force in the horizontal direction (top panel) and the vertical direction (bottom panel). In the horizontal direction, the gravitational force is replaced by the gravitational force from which the centrifugal force is subtracted. Both panels are the close-up of the inner region of  $500R_S \times 500R_S$  using the time average from 3.34 yr to 6.67 yr. The two black lines are the streamlines of the wind. In the region surrounded by the red lines, the velocity of the wind is larger than the escape velocity.

the launching from the disk surface. At this point, the horizontal and vertical components of velocity are  $0.080c$  ( $24,000 \text{ km s}^{-1}$ ) and  $0.039c$  ( $11,700 \text{ km s}^{-1}$ ).

The middle panel of Figure 3.4 shows the forces acting in the horizontal direction. The gravitational force, the centrifugal force, the gravitational force from which the centrifugal force is subtracted and the radiation force are shown by the red, green, purple and blue lines. Comparing the blue line and the purple line, we can find that the radiation force dominates the gravitational force reduced by the contribution of the centrifugal force. The radiation force is greater than the gravitational force itself (see the blue line and the red line). The amplitude of the radiation force is  $\sim 10$  times larger than the gravity from the launching region to over  $100R_S$  after launching.

The forces acting in the vertical direction are plotted in the bottom panel of Figure 3.4. The red and blue lines show the gravitational force and the radiation force. Same as the horizontal components, the radiation force dominates the gravitational force. The amplitude of the radiation force is also  $\sim 10$  times larger than the gravitational force.

Along this streamline, the radiation force continues to be larger than the gravitational force after the velocity exceeds the escape velocity. Then the wind continues to be accelerated. However, the amplitude of the radiation force decreases with the getting away from the accretion disk. Then for  $s > 100R_S$ , the velocity is nearly constant,  $v_r \sim 0.3c-0.4c$  and  $v_z \sim 0.1c$ .

Figure 3.5 is same as Figure 3.4, but for the streamline shown by the long-dashed line in the Figure 3.3. In the top panel, the velocity exceeds the escape velocity at  $20R_S$  after the launching from the disk surface. At this point, the horizontal and vertical components of the velocity are  $0.11c$  ( $33,000 \text{ km s}^{-1}$ ) and  $0.050c$  ( $15,000 \text{ km s}^{-1}$ ). In the middle panel, comparing the radiation force (the blue line) and the gravitational force reduced by the centrifugal force (the purple line), the former is larger within  $s \lesssim 20R_S$ . Comparing the radiation force and the gravitational force itself (the red line), the regions where the radiation force exceeds the gravitational force only appear at  $s \sim 0.2-0.3R_S$  and  $s \sim 0.5-1R_S$  at which the radiation force has the peaks. In other regions of  $s \lesssim 20R_S$ , the centrifugal force assists the radiation force to accelerate the wind in the horizontal direction. In the vertical direction, the radiation force is larger than the gravitational force within  $s \lesssim 10R_S$  (bottom panel). The vertical component of the radiation force has peaks at the same regions as the horizontal component of the radiation force.

Comparing three panels, the rapid increase of the velocity occurs at the points where the radiation force has the peaks. At the first peak,  $s \sim 0.2-0.3R_S$ , the increase is small,

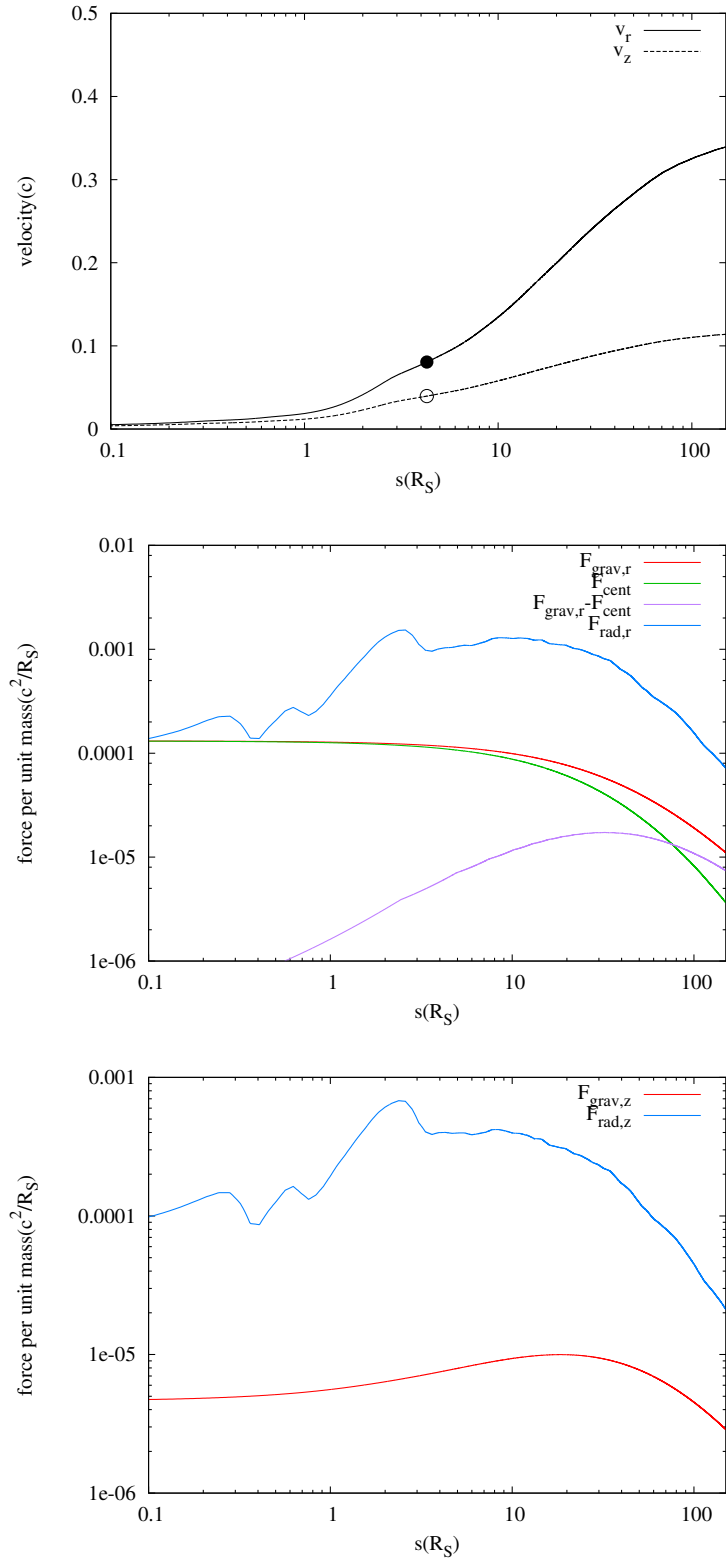


Figure 3.4: Velocity (top panel), forces acting in the horizontal direction (middle panel), and forces acting in the vertical direction (bottom panel) as a function of the distance along the streamline that is shown by the short-dashed line in Figure 3.3. In the top panel, the point where the velocity exceeds the escape velocity is shown by the filled circle and the open circle on each line.

but at the second peak,  $s \sim 1R_S$ , we can find the obvious increase of the velocity. This is explained by the fact that the strong radiation force accelerates the wind. The point where the velocity exceeds the escape velocity, which is marked by the circles in the top panel, is located at the end of the acceleration region in the horizontal direction. For this streamline, the velocity of the wind reaches the escape velocity due to the radiation force with the assistance of the centrifugal force. However, after the wind velocity exceeds the escape velocity, the radiation force becomes weaker than the gravity. Then the wind is not accelerated and the terminal velocity of the wind is smaller than that of another streamline discussed above.

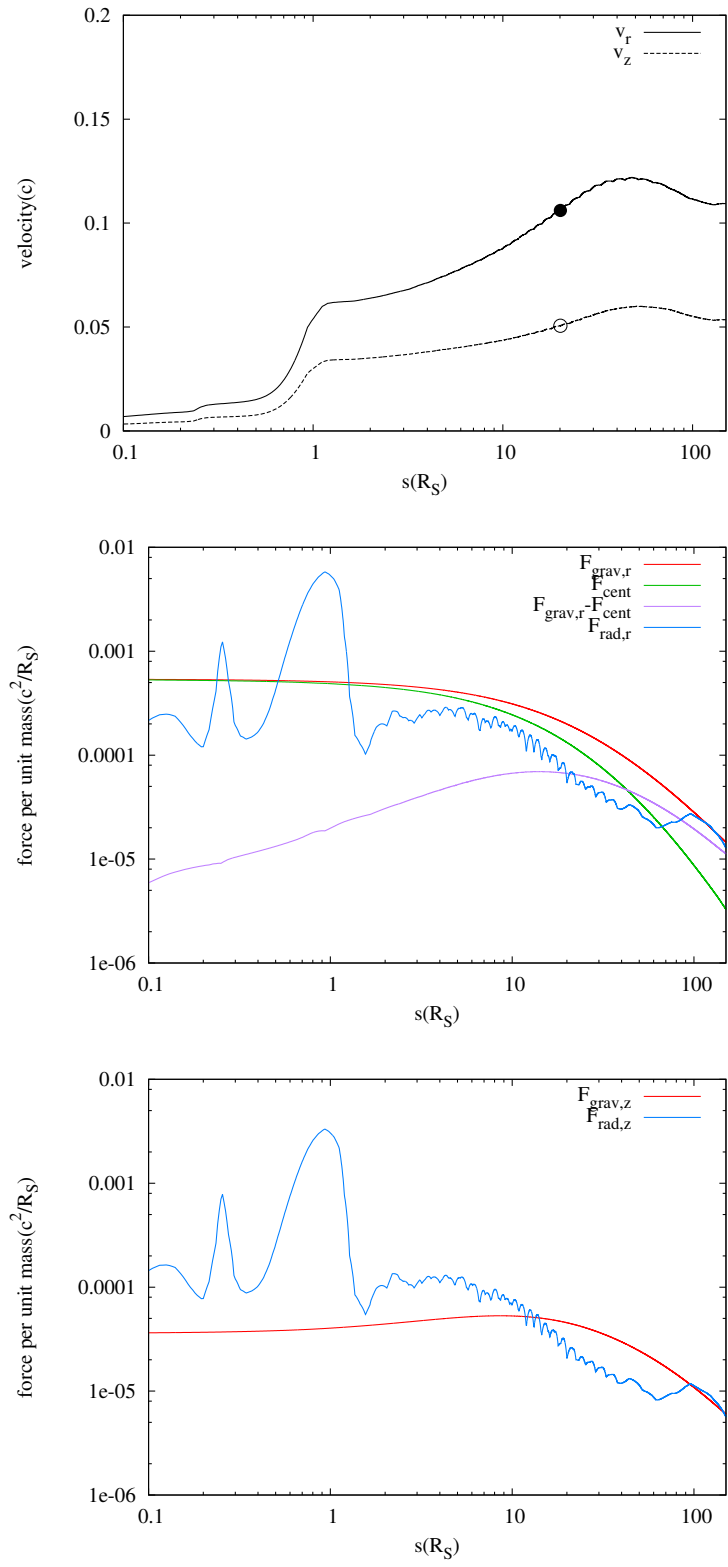


Figure 3.5: Same as 3.4, but for the streamline shown by the long-dashed line in the Figure 3.3.

### 3.2.3 Comparison with observations of UFOs

We compare the results of our simulations to the observational features and calculate the probability of the detecting UFO (UFO probability). The method is the same as the estimation of the BAL probability for the non-hydrodynamic model, (§2.1.5). Based on Tombesi et al. (2011), we consider two conditions to detect UFO: (A) the outward velocity of the matter with  $2.5 < \log \xi < 5.5$  exceeds  $10,000 \text{ km s}^{-1}$ , (B) the column density of the matter with  $2.5 < \log \xi < 5.5$  is larger than  $10^{22} \text{ cm}^{-2}$ . We check these conditions along the lines of sight (from an observer to the center of the coordinate) with the viewing angle between  $\theta = 0^\circ$  and  $90^\circ$ . If both conditions, (A) and (B), are satisfied, we consider that the absorption features of UFO emerge in the spectra. We calculate the solid angle,  $\Omega_{\text{UFO}}$ , in which the conditions (A) and (B) are satisfied. We can get the UFO probability by dividing this value by  $4\pi$ ,  $\Omega_{\text{UFO}}/4\pi$ . The average UFO probability is 20.3 %. The UFO probability for the snapshot after 6.67 yr is 24%.

Figure 3.6 shows the maximum velocity of the matter with  $2.5 < \log \xi < 5.5$  (solid line) and the column density of the matter with  $2.5 < \log \xi < 5.5$  (dashed line) for the snapshot at the same time as Figure 3.1. The abscissa is the viewing angle. The ordinate on the left-hand side shows the value of the solid line. The ordinate on the right-hand side shows the value of the dashed line. The red solid line and the red dashed line show the lines of  $v_{\text{max}} = 10,000 \text{ km s}^{-1}$  and  $N_{\text{H}} = 10^{22} \text{ cm}^{-2}$ . The UFO features are observed in the unshaded ranges,  $48.2^\circ < \theta < 53.2^\circ$ ,  $66.5^\circ < \theta < 75.9^\circ$ ,  $81.0^\circ < \theta < 82.1^\circ$  and  $89.2^\circ < \theta < 89.3^\circ$ . In these ranges, the maximum velocity of the matter with  $2.5 < \log \xi < 5.5$  is over  $10,000 \text{ km s}^{-1}$  and the column density of the matter with  $2.5 < \log \xi < 5.5$  exceeds  $10^{22} \text{ cm}^{-2}$ . That is, the UFO conditions (A) and (B) are both satisfied. In the ranges shaded with gray, the UFO features are not detected.

In the polar direction of  $\theta \lesssim 47^\circ$ , there is no dense and fast outflow, so neither of the conditions (A) nor (B) is satisfied. Also in the range of  $53^\circ \lesssim \theta \lesssim 61^\circ$ , neither of the conditions is satisfied, because around this region, the matter struggles to outflow and the outflow velocity is smaller than that in the region with the large polar angle. For other most part of the shaded ranges, the maximum velocity is enough large and meets the condition (A), but the column density insufficient to meet the condition (B).

In Figure 3.6, the abscissa is divided into 9 regions: 4 UFO regions (unshaded) and 5 non-UFO regions (shaded). Figure 3.7-3.9 show the column density as the function of the outward velocity along the line of sight with the angles picked up from the each region in Figure 3.6, except for the polar and equatorial non-UFO regions (rightmost and

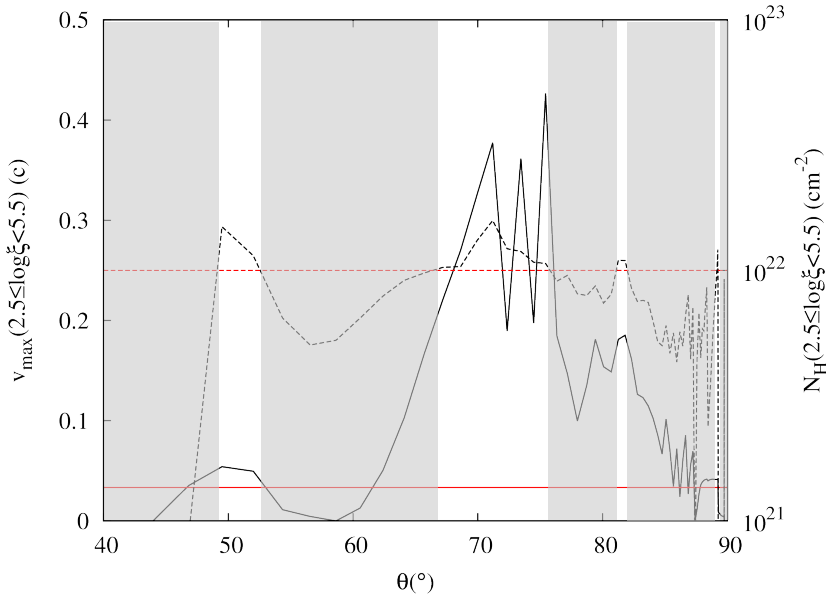


Figure 3.6: Maximum velocity of the matter with  $2.5 < \log \xi < 5.5$  and column density of the matter with  $2.5 < \log \xi < 5.5$  of the flow for the snap shot at the same time as Figure 3.1. The ordinate on the left-hand side shows the value of the solid line. The ordinate on the right-hand side shows the value of the dashed line. The red solid line and the red dashed line show the lines of  $v_{\max} = 10,000 \text{ km s}^{-1}$  and  $N_{\text{H}} = 10^{22} \text{ cm}^{-2}$ . In the ranges shaded with gray, the UFO conditions are not satisfied.

leftmost shaded regions). The radial velocity is binned, and each bin has the width of  $10,000 \text{ km s}^{-1}$ . Bars filled with the cyan and the orange refer to the column densities of the matter with the ionization parameters,  $2.5 \leq \log \xi < 5.5$  and  $2.5 \leq \log \xi < 4.0$ . The matters in these ranges of ionization parameter contribute to the absorption features of the UFO. Bars framed by green line and the blue line show the column density of the matter with the ionization parameter,  $\log \xi < 2.5$  and  $\log \xi \geq 5.5$ . Neither of them contributes to the UFO features. The dotted line shows the line of  $10,000 \text{ km s}^{-1}$ .

These are the spectra-like plots, in which the outward velocity and the column density correspond to the blueshifted velocity and the depth of the absorption line. We research the two different ranges of the ionization parameter, in which the UFO is detected,  $2.5 \leq \log \xi < 5.5$  and  $2.5 \leq \log \xi < 4.0$ , since the highly ionized matter of which the ionization parameter is 5.5 is almost fully ionized and the absorption lines of these matters are difficult to be detected. The range,  $2.5 \leq \log \xi < 4.0$ , is useful to investigate the contribution to the UFO features from the low ionization part of the wind.

For small viewing angles,  $\theta = 52.0^\circ$  and  $60.6^\circ$  (Figure 3.7), there is no matter with  $\log \xi < 2.5$ . The column densities with  $\log \xi \geq 5.5$  and  $2.5 \leq \log \xi < 5.5$  are large around

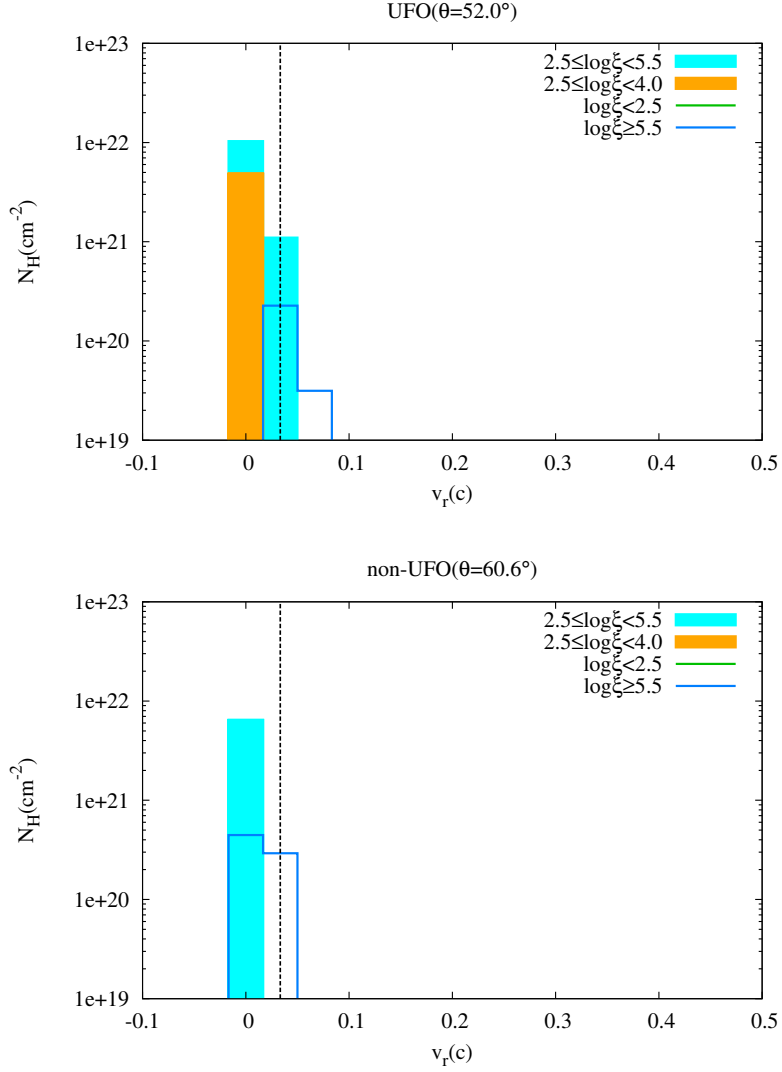


Figure 3.7: Column density as the function of the outward velocity along the line of sights with the viewing angles of  $\theta = 52.0^\circ$  (top panel) and  $60.6^\circ$  (bottom panel). The velocity is binned, and each bin has the width of  $10,000 \text{ km s}^{-1}$ . The bars filled with the cyan and the orange refer to the column density with the ionization parameter of  $2.5 \leq \log \xi < 5.5$  and  $2.5 \leq \log \xi < 4.0$ . The bars framed by the green and the blue lines show the column density with the ionization parameter of  $\log \xi < 2.5$  and  $\log \xi \geq 5.5$ . The dotted line shows the line of  $10,000 \text{ km s}^{-1}$ .

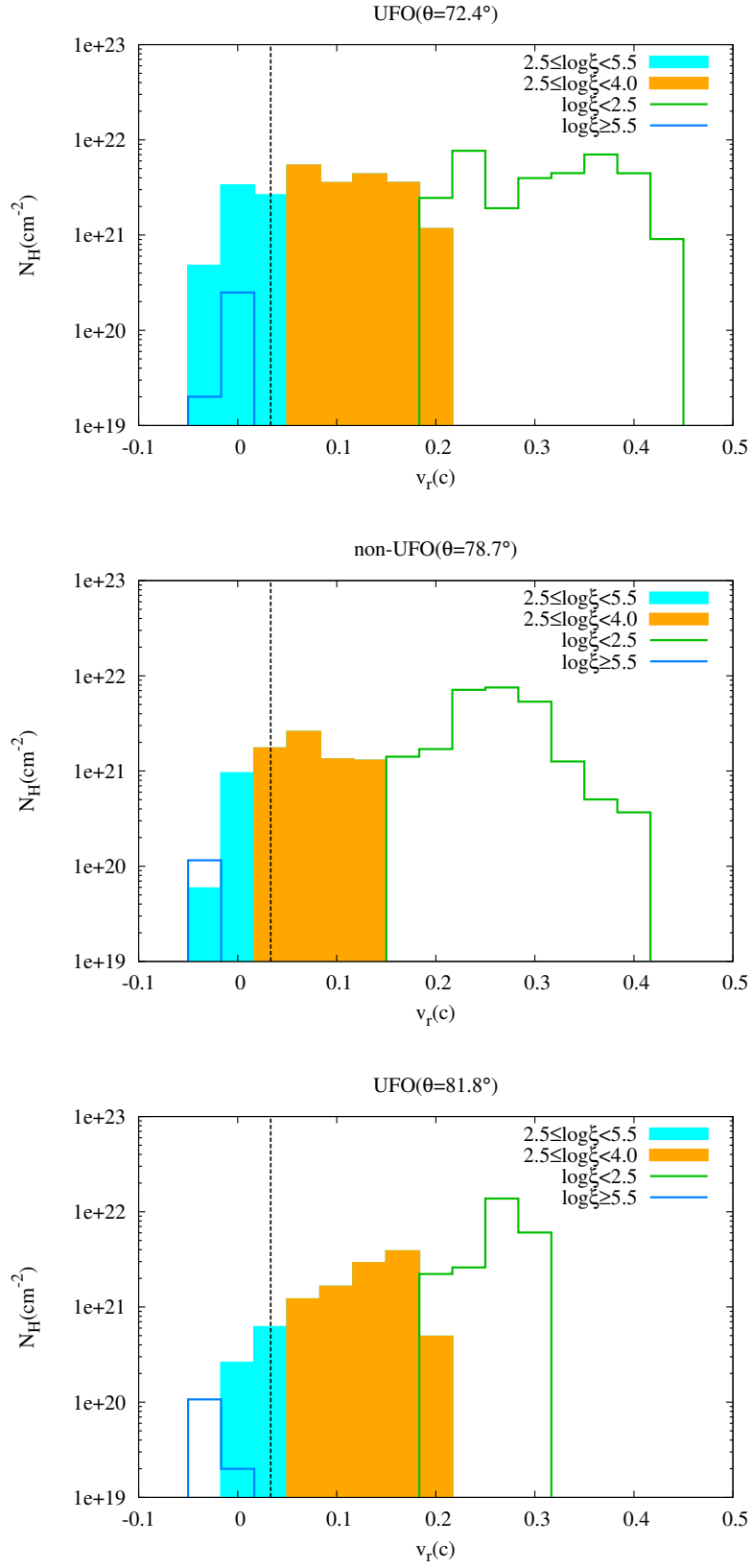


Figure 3.8: Same as Figure 3.7, but for the viewing angles of  $\theta = 72.4^\circ$  (top panel),  $78.7^\circ$  (middle panel), and  $81.8^\circ$  (bottom panel).

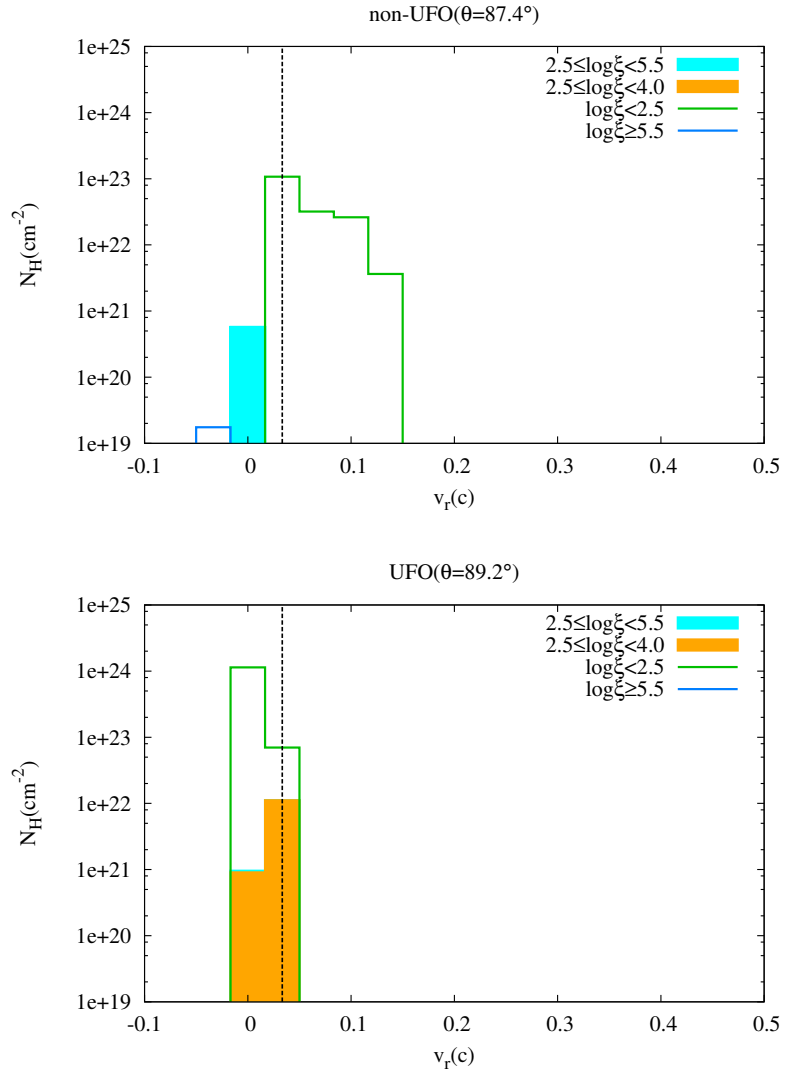


Figure 3.9: Same as Figure 3.7, but for the viewing angles of  $\theta = 87.4^\circ$  (top panel) and  $89.2^\circ$  (bottom panel).

$v_r \sim 0\text{--}10,000 \text{ km s}^{-1}$ . There is no wind with high velocity  $\gtrsim 0.1$ . This is explained by the fact that, along these streamlines, the matter is highly ionized and the acceleration by the line force is weak. The plot for  $2.5 \leq \log \xi < 4.0$  appears in the panel for  $\theta = 52.0^\circ$ . Along this angle, the UFO conditions, (A) and (B) are satisfied and the UFO is detected. For  $\theta = 60.6^\circ$ , neither the condition (A) nor (B) is satisfied and the UFO is not detected.

Among the top, middle and bottom panel of Figure 3.8 (plots for  $\theta = 72.4^\circ$ ,  $78.7^\circ$ , and  $81.8^\circ$ ), the overall tendency is similar to each other. The velocity ranges are shifted toward larger velocity with the decrease of the ionization parameter. The column densities with  $\log \xi < 2.5$  and  $2.5 \leq \log \xi < 4.0$  span the velocity ranges  $v_r = 0.2\text{--}0.4c$  and  $10,000 \text{ km s}^{-1}\text{--}0.2c$ . The matters with  $4.0 \leq \log \xi < 5.5$  and  $\log \xi \geq 5.5$  are almost at rest or move inward. This is because the acceleration by the line force is more effective for lower ionized matter. For  $\theta = 72.4^\circ$  and  $81.8^\circ$ , the condition (A) and (B) are satisfied and the UFO is observed, but for  $\theta = 78.7^\circ$ , the UFO is not detected since the total column density with  $2.5 \leq \log \xi < 5.5$  is smaller than  $10^{22} \text{ cm}^{-2}$ , though the condition of the maximum velocity [the condition (A)] is met.

For the larger viewing angle,  $\theta = 87.4^\circ$  and  $89.2^\circ$  (Figure 3.9), the amount highly ionization mater,  $\log \xi \geq 4.0$ , decreases. Inversely, the column density of the matters with  $\log \xi < 2.5$  is very large,  $\gtrsim 10^{23} \text{ cm}^{-2}$ . For  $\theta = 87.4^\circ$ , the UFO is not observed because large part of the wind is in the low ionization state. Thus neither the condition (A) nor (B) is satisfied. For  $\theta = 89.2^\circ$ , the cyan plot disappears. The UFO condition is satisfied by the contribution of relatively lower ionized matters.

We discussed about the comparison between our result and observation of the UFO for the snapshot. Next we focus on the time variability of the UFO probability. Figure 3.10 shows the time variability of the UFO probability (black solid line with filled circles) and the mass of the matter with the ionization parameter of  $2.5 \leq \log \xi \leq 5.5$  (blue dashed line with open circles). The UFO probability fluctuates around 20%. The overall behavior of the UFO probability is similar to that of the mass of the matter with the ionization parameter,  $2.5 \leq \log \xi \leq 5.5$ , in the simulation box, and this is the previous origin of the fluctuation of the UFO probability.

We investigate the time variability of the ranges of viewing angle for which UFO is observed. In Figure 3.11, the ranges of the viewing angle for which UFO is detected are collared by the cyan for the time range from 5 yr to 6 yr. Around  $\theta \sim 70^\circ$ , the UFO is observed independent from the time. However, the fluctuation gradually appears with the increase or decrease of the viewing angle. When the UFO probability is large, the

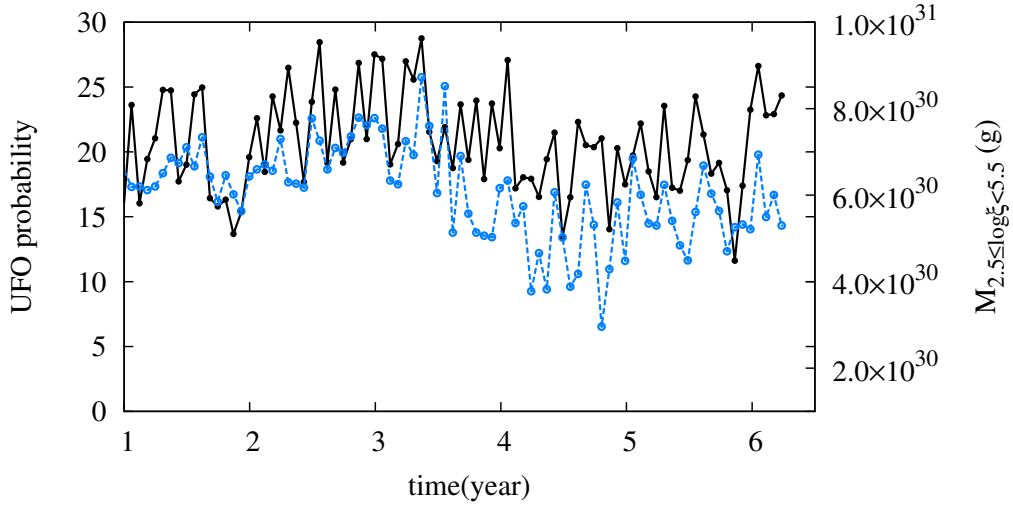


Figure 3.10: Time variabilities of the UFO probability (the black solid line with the filled circles) and the mass of the matter with the ionization parameter of  $2.5 \leq \log \xi < 5.5$  (the blue dashed line with the open circles).

UFO features are detected for these larger and/or smaller viewing angles.

We research the variation of the maximum velocity and column density for three viewing angles shown by the black lines in Figure 3.11. The solid line ( $\theta = 72.4^\circ$ ) is chosen from the range of the viewing angle in which UFO is statically observed. The dashed line ( $\theta = 65.7^\circ$ ) and dotted line ( $\theta = 77.2^\circ$ ) are in the ranges in which we find the fluctuation of the detecting UFO. The former is for the smaller viewing angle and the latter for the larger viewing angle. The results are presented in the Figure 3.12-3.14. The green, orange, cyan and blue lines show the value of the matter with  $\log \xi < 2.5$ ,  $2.5 \leq \log \xi < 4.0$ ,  $2.5 \leq \log \xi < 5.5$ , and  $\log \xi \geq 5.5$ . The cyan lines are the values that satisfy the condition of the ionization parameter for UFO detection. In each panel, the dashed black lines show the condition value of the velocity and column density,  $v_r = 10,000 \text{ km s}^{-1}$  and  $N_{\text{H}} = 10^{22} \text{ cm}^{-2}$ . If cyan lines exceed these dashed lines in both panels for the velocity and the column density, the UFO is detected. The time intervals in which the UFO is not observed are shaded by the gray.

We focus on the behavior of the cyan lines. For  $\theta = 72.4^\circ$  (Figure 3.12), the maximum velocity and the column density fluctuate, but both meet the conditions for detecting UFOs at all times. For  $\theta = 77.2^\circ$  (Figure 3.13) that is the larger than the range of the viewing angle in which UFOs are stably observed, the velocity meets the condition at all times (top panel). The column density is slightly larger than  $10^{22} \text{ cm}^{-2}$  in the unshaded regions, but slightly smaller than the threshold in the shaded regions (bottom panel).

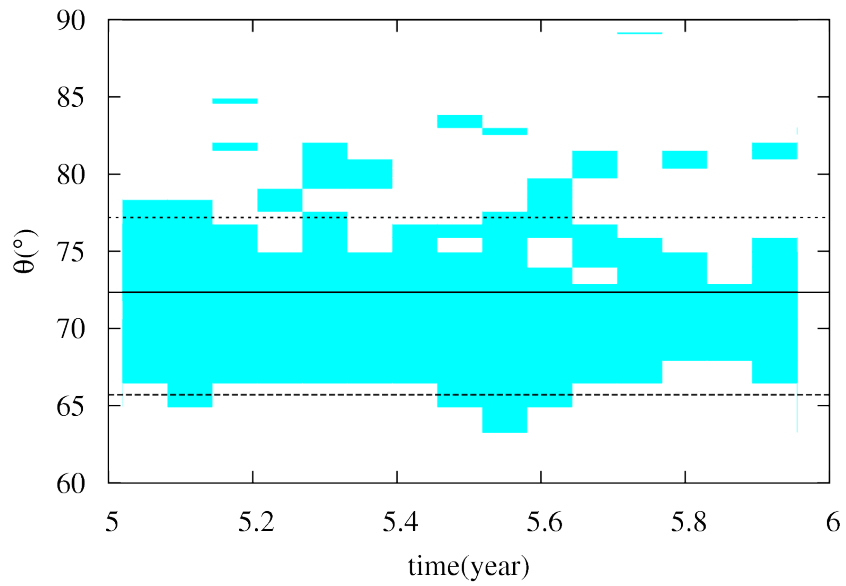


Figure 3.11: Time variability of the ranges of the viewing angle in which the UFO is detected. The ranges are collared by the cyan. The solid, dashed and dotted lines show the angles,  $\theta = 72.4^\circ$ ,  $65.7^\circ$ , and  $77.2^\circ$ .

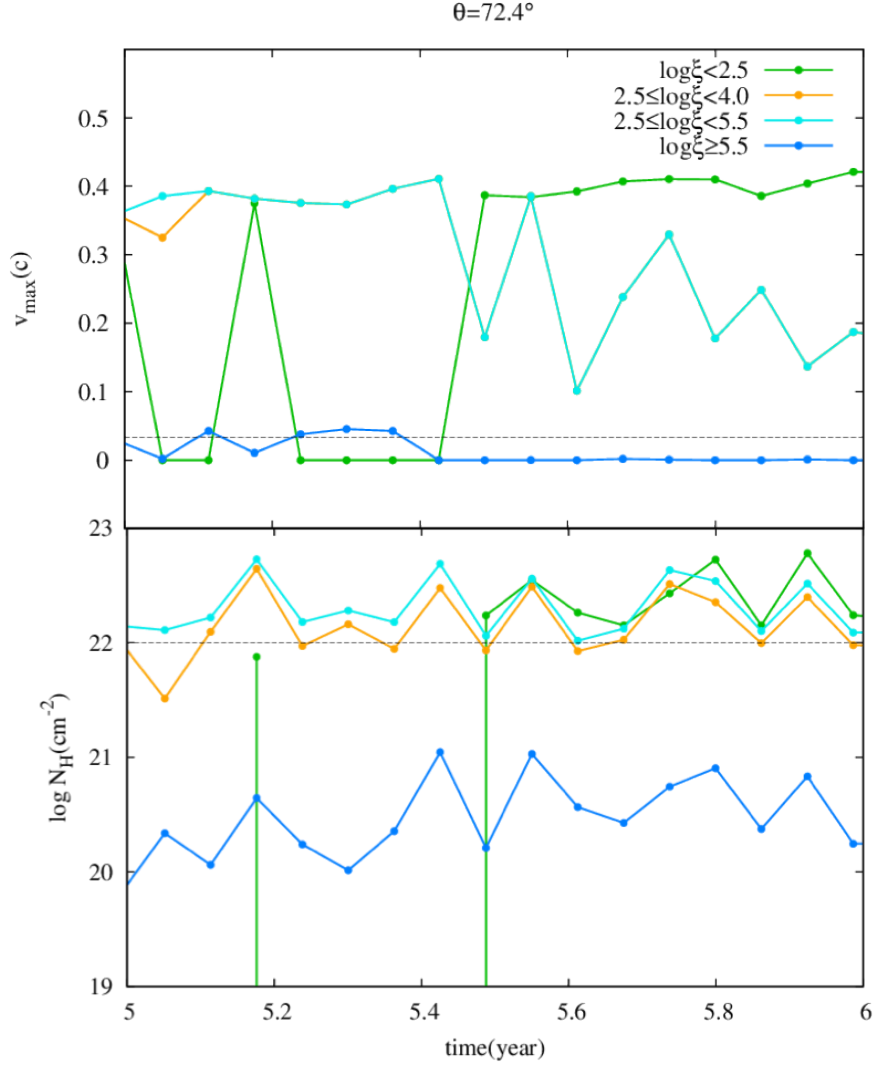


Figure 3.12: Time variabilities of the maximum velocity (top panel) and the column density (bottom panel) for  $\theta = 72.4^\circ$ . The green, orange, cyan, and blue lines show the values for  $\log \xi < 2.5$ ,  $2.5 \leq \log \xi < 4.0$ ,  $2.5 \leq \log \xi < 5.5$ , and  $\log \xi \geq 5.5$ . In each panel, the dashed black lines show the condition values of the velocity and the column density,  $v_r = 10,000 \text{ km s}^{-1}$  and  $N_{\text{H}} = 10^{22} \text{ cm}^{-2}$ . The time intervals in which the UFO is not observed are shaded by the gray.

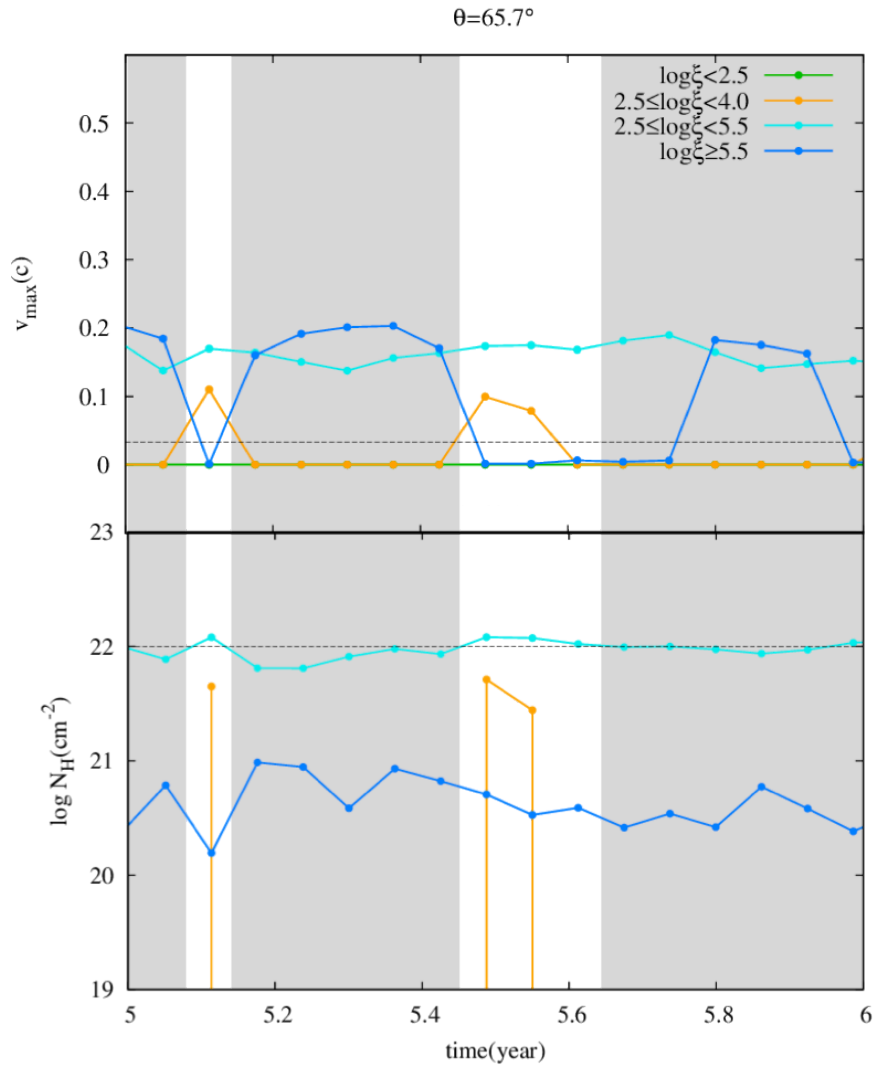


Figure 3.13: Same as Figure 3.12, but for  $\theta = 65.7^\circ$ .

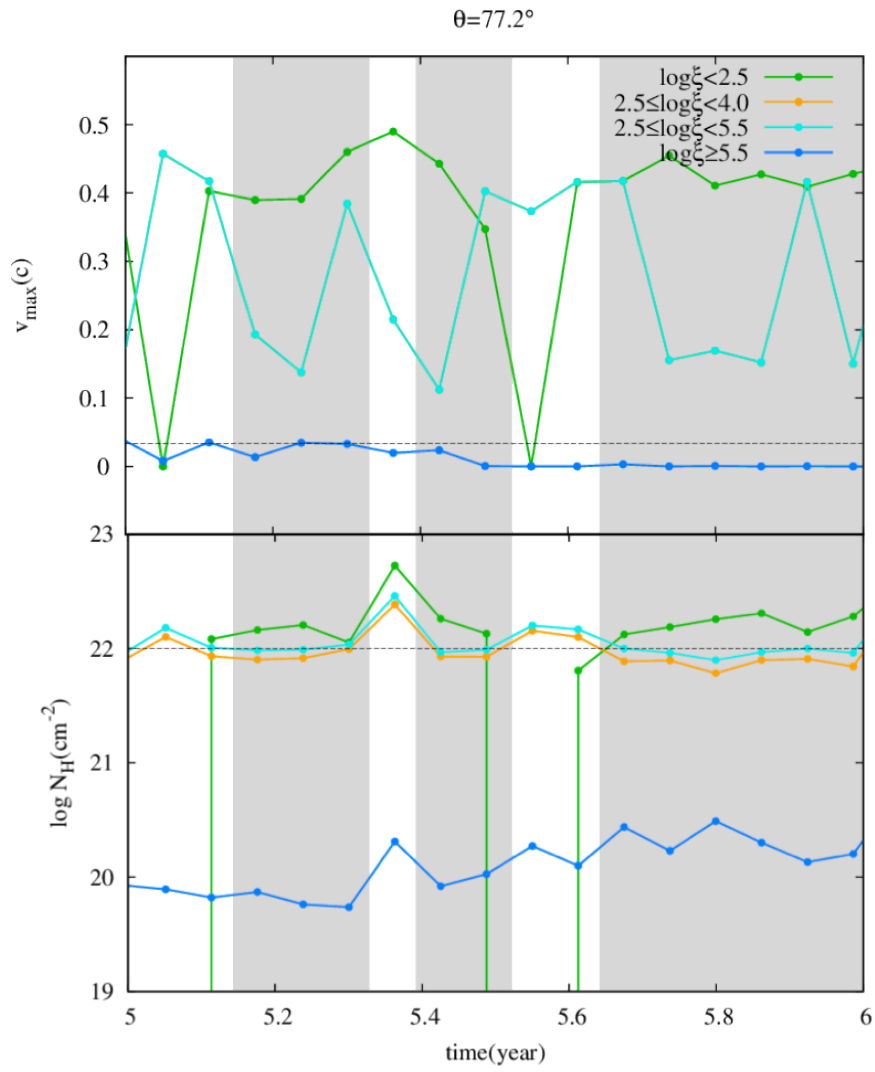


Figure 3.14: Same as Figure 3.12, but for  $\theta = 77.2^\circ$ .

Thus, the cause of the fluctuation between UFO and non-UFO is the variation of the column density. The same could be said for smaller viewing angle,  $\theta = 65.7^\circ$ . In the top panel of Figure 3.14, the maximum velocity is smaller and more static than that for  $\theta = 77.2^\circ$ , but exceeds  $10,000 \text{ km s}^{-1}$  at all times. The cause of the transition between UFO and non-UFO is the fluctuation of the column density around the condition value,  $10^{22} \text{ cm}^{-2}$ . We conclude that the minute fluctuation of the column density induces the fluctuation of the UFO detection.

It is needed more consideration whether the column density of the flow must be larger than  $10^{22} \text{ cm}^{-2}$  to detect the absorption features of UFOs in the realistic observation. Here we regard the case that the column density is just a little smaller than  $10^{22} \text{ cm}^{-2}$  as a non-UFO. In reality, it is possible that the shallow absorption troughs on the spectra are still observed, though the column density is small. If we can detect the shallow absorption features, the transition between UFO and non-UFO we explained above might be the variation of the absorption strength of the absorption features of the UFOs.

Here we comment about the plots for other ionization parameter range. The behavior of the orange lines ( $2.5 \leq \log \xi < 4.0$ ) is similar to the cyan lines ( $2.5 \leq \log \xi < 5.5$ ) in Figure 3.12. In the panel for the maximum velocity (top panel), orange line overlaps with the cyan line. The column density shown by the orange line is the slightly smaller than that shown by the cyan line and sometimes falls below the condition value. If we use  $2.5 \leq \log \xi < 4.0$  as the condition of the ionization parameter for UFO, the UFO is not detected when the column density is smaller than  $10^{22} \text{ cm}^{-2}$  and the transition between UFO and non-UFO appears. We use the range,  $2.5 \leq \log \xi < 4.0$ , as the another candidate of the condition that the ionization parameter of the flow should meet for detecting UFOs, because the ionization parameter of  $\log \xi > 4.0$  suggests that the metals are nearly fully ionized and might not contribute to making absorption feature so much. Also in Figure 3.14, orange and cyan lines show the similar behavior. However, in Figure 3.13, maximum velocity shown by the orange line is around zero for most of the time. In addition, column density falls to well below  $10^{22} \text{ cm}^{-2}$ . Thus, we find that relatively highly ionized matter mainly contributes the UFO features. If we use  $2.5 \leq \log \xi < 4.0$  as the condition of the ionization, we cannot observe a UFO in this viewing angle. About almost fully ionized matter of which the ionization parameter is  $\log \xi \geq 5.5$ , the column density is around  $10^{20}$ – $10^{21} \text{ cm}^{-2}$  for all three angles, but the maximum velocity becomes smaller with the increase of the viewing angle. About lower ionized matter of which the ionization parameter is  $\log \xi < 2.5$ , the amount of matter and the maximum velocity

become larger with the increase of the viewing angle. There is no matter that meets this range of the ionization parameter for smaller viewing angle,  $\theta = 65.7^\circ$ .

Table 3.1: Eddington ratio dependence of the time averaged UFO probability (%)

Eddington ratio	0.1	0.3	0.5	0.7
UFO probability	3.5	21.0	20.4	26.9

### 3.2.4 Parameter dependence

We investigate the parameter dependence of UFO probability. In our calculation, the Eddington ratio and the black hole mass are the free parameters. First we consider the Eddington ratio dependence.

**Eddington ratio dependence**— Table 3.1 shows the Eddington ratio dependence of the averaged UFO probability. We investigate the disk wind for  $\epsilon = 0.1, 0.3,$  and  $0.7$  when we set the black hole mass to be constant,  $M_{\text{BH}} = 10^8 M_{\odot}$ . Here, we focus on the sub-Eddington disk. Except for the case of  $\epsilon = 0.1$ , the UFO probabilities are  $\sim 20\text{--}30\%$ . For  $\epsilon = 0.1$ , the UFO probability is very small,  $3.5\%$ .

Figure 3.15-3.17 show the color maps of the density, temperature, and ionization parameter and the velocity field in the same manner as Figure 3.1, but for  $\epsilon = 0.1, 0.3$  and  $0.7$ . We find the disk wind with the small opening angle and the low density in the top left panel of Figure 3.15. The height of the  $z = 0$  plane above the equatorial plane of the disk is set to be  $z_0 = 4.0\epsilon R_{\text{S}}$ . Therefore, for  $\epsilon = 0.1$ , the height is  $z_0 = 0.4R_{\text{S}}$  and the wind is launched from just above the UV source. As a result, the vertical component of the radiation force is larger relative to the horizontal component in the launching region and the matter is blown up to a relatively polar region. The density in the inner region is small, because of the weak radiation force. This results in the weak X-ray shielding. Even in the region with the large polar angle  $\theta \gtrsim 75^\circ$ , the ionization parameter is relatively large  $\log \xi \sim 2\text{--}4$  (see the bottom left panel of Figure 3.15). This means that the line force works only in the near equatorial region. The large portion of the wind is accelerated only near the disk surface and the portion of the launched wind returns to the disk. The region in which the line force continues to accelerate the wind after the launching is very small. Also, the region with the low temperature is small due to the weak X-ray shielding (top right panel of Figure 3.15). The small Eddington ratio and the contribution of the line force in the tight region work to decrease the velocity of the wind. However, the wind is launched from only  $0.4R_{\text{S}}$  above the UV source, and this has the opposite effect that increases the velocity. These effects are countered by each other. As a consequence, the

velocity is almost the same as that for  $\varepsilon = 0.5$  (see the bottom right panel of Figure 3.15 and Figure 3.1).

The results for  $\varepsilon = 0.3$  (Figure 3.16) have the same tendency with the results for  $\varepsilon = 0.1$ . However, there is matter with relatively high density,  $\rho = 10^{-16} \text{ g cm}^{-3}$ , in the inner region of the disk surface (top left panel), since the radiation force is larger than that for  $\varepsilon = 0.1$ . This dense matter plays a role of X-ray shielding gas. As a result, the region in which the ionization parameter and the temperature are low becomes large (bottom left panel and top right panel). The acceleration region due to the line force becomes larger with the increase of the low-ionization region. However the outflow velocity is not so changed (bottom right panel), because the height of the  $z = 0$  plane from the UV source,  $z_0 = 1.2R_S$ , is more distant than that in the case of  $\varepsilon = 0.1$ .

In Figure 3.17, the features of the results for  $\varepsilon = 0.7$  are also explained by the basically same mechanism. In this case, the height of the  $z = 0$  plane from the UV source is large,  $z_0 = 2.8R_S$ . Then the opening angle is larger than the result for smaller Eddington ratios. By the strong radiation force, the dense matter is blown up from the inner disk surface (top left panel), and the strong X-ray shielding effect appears in near the equatorial region. In the shielded region, the ionization parameter and the temperature are low (bottom left panel and top right panel). Since the radiation force is large and the density of the matter is enough large to decrease the ionization parameter, there is almost no failed wind region. If once the matter is accelerated near the disk surface, the wind successfully blown away. For this reason, the density map (top left panel) has the sharp edge between the line-driven disk wind and the low-density polar region. Also in this case, the terminal velocity of the wind is almost the same as that for other smaller Eddington ratios due to the effects of the strong radiation force and large distance from the UV source are cancelled out by each other (see the bottom right panel).

Figure 3.18 is the same as Figure 3.6, but for different Eddington ratios,  $\varepsilon = 0.1$  (top panel),  $0.3$  (middle panel), and  $0.7$  (bottom panel). For  $\varepsilon = 0.1$  (top panel), unshaded range in which UFO is observed is very narrow and the UFO probability is very small, 1.7% for this snapshot. This is because the column density of the matter with the ionization parameter,  $2.5 \leq \log \xi < 5.5$ , is small though the maximum velocity of the matter in this ionization parameter range is enough large to exceed the condition value,  $10,000 \text{ km s}^{-1}$ . The low density of the wind shown in Figure 3.15 results in the small column density.

For  $\varepsilon = 0.3$  (middle panel), the UFO is observed around  $70^\circ$  and the overall behaviors of the maximum velocity and the column density are similar to those of  $\varepsilon = 0.5$ . For

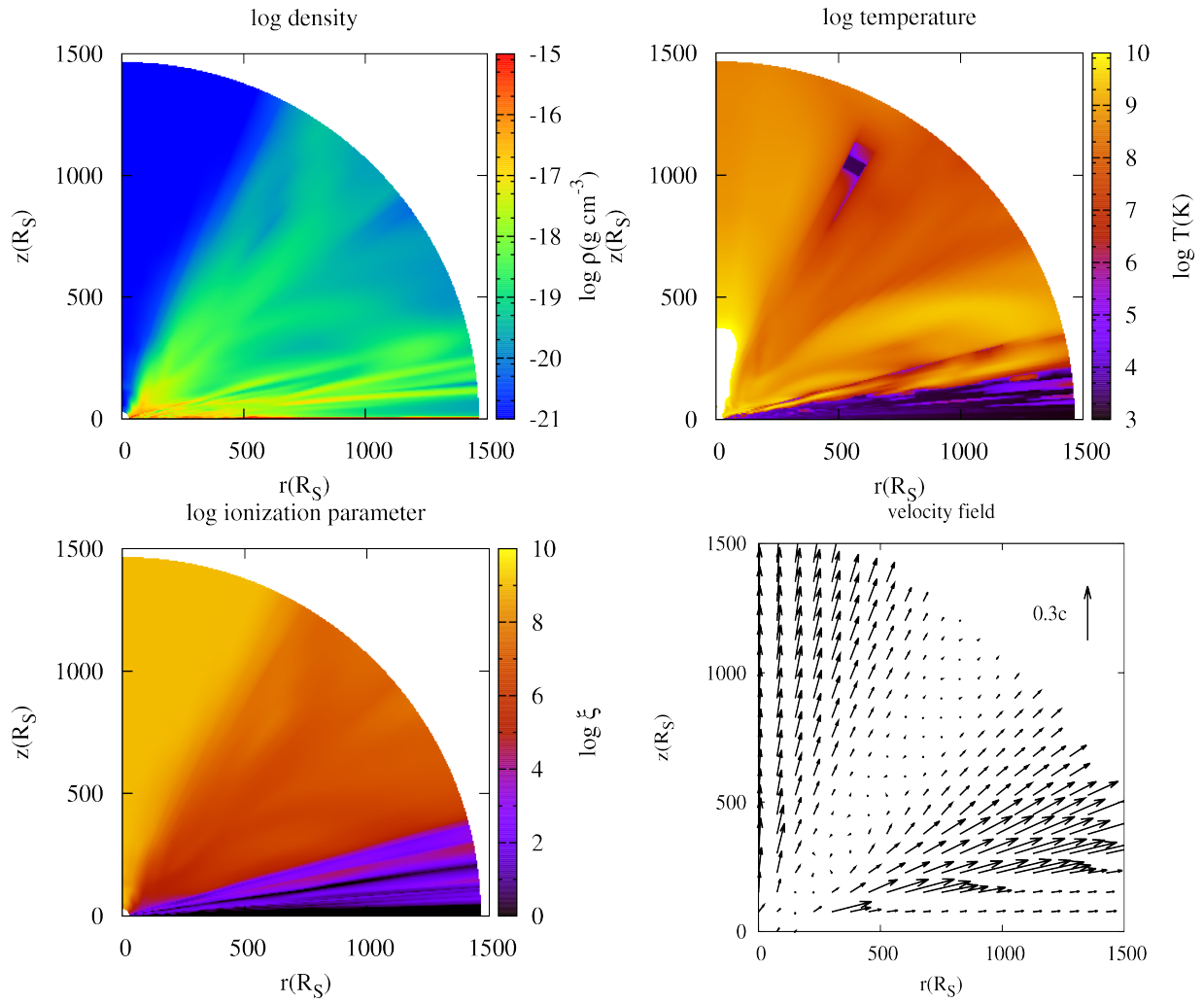


Figure 3.15: Same as Figure 3.1, but for  $\varepsilon = 0.1$ .

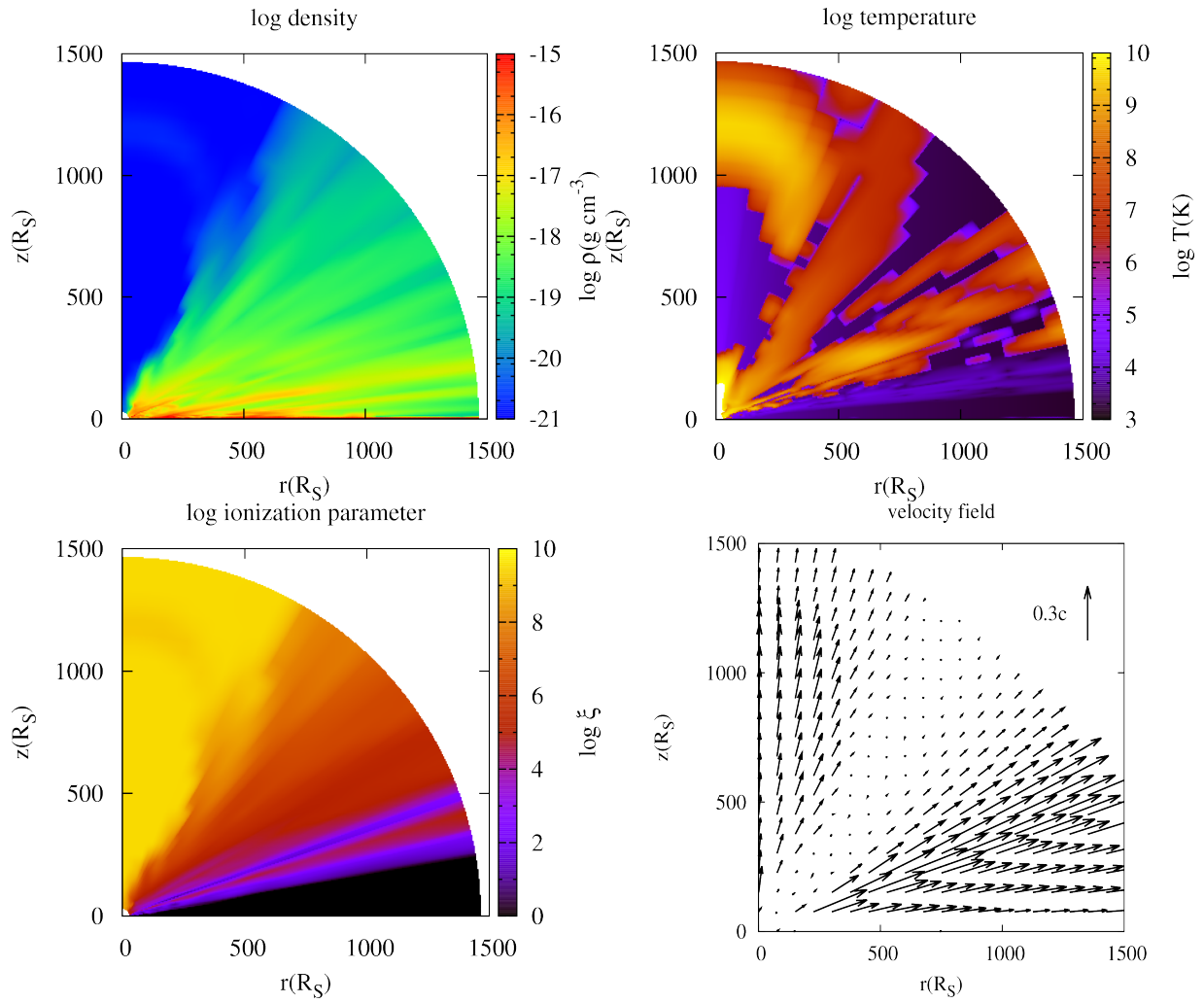


Figure 3.16: Same as Figure 3.1, but for  $\varepsilon = 0.3$ .

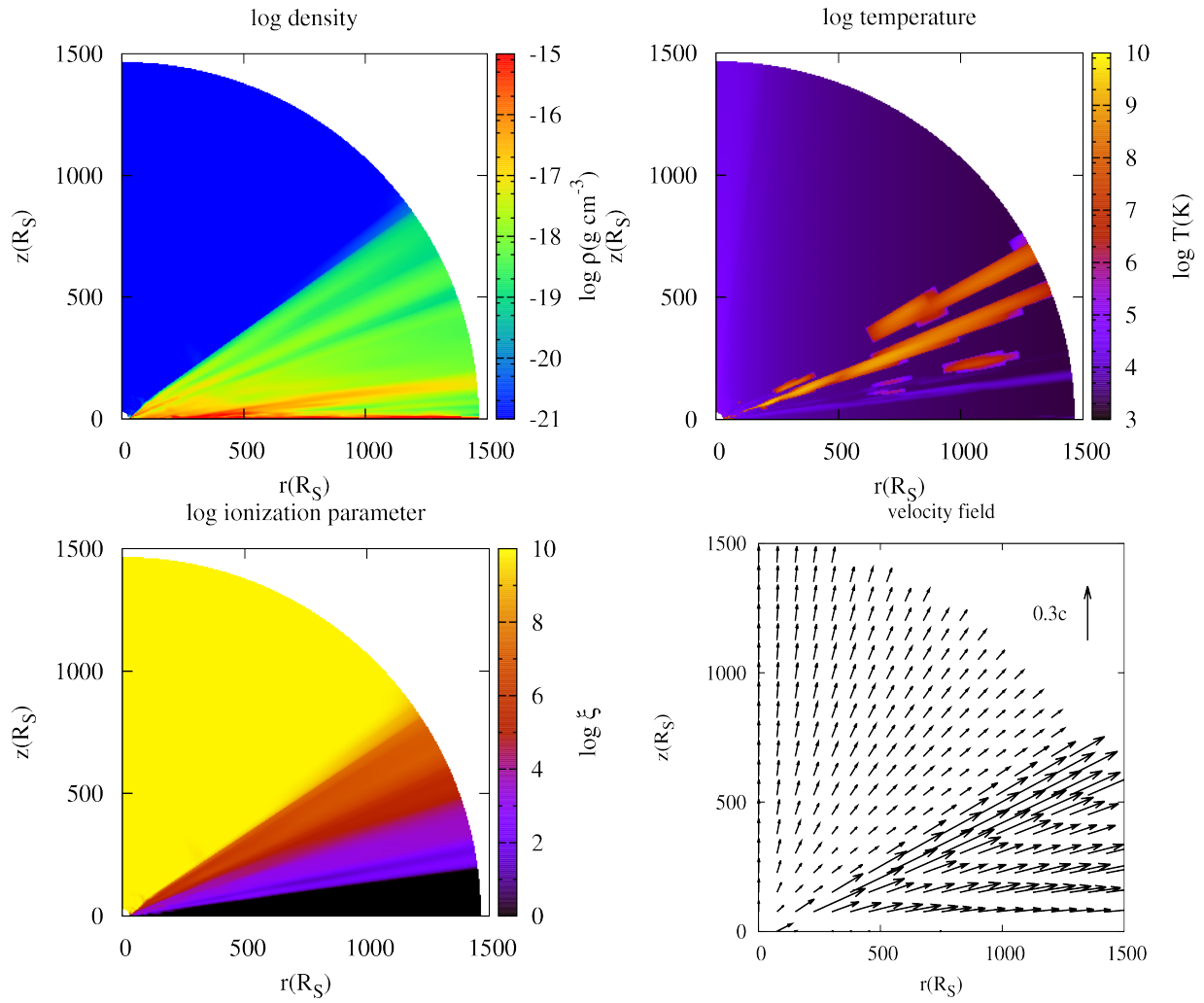


Figure 3.17: Same as Figure 3.1, but for  $\varepsilon = 0.7$ .

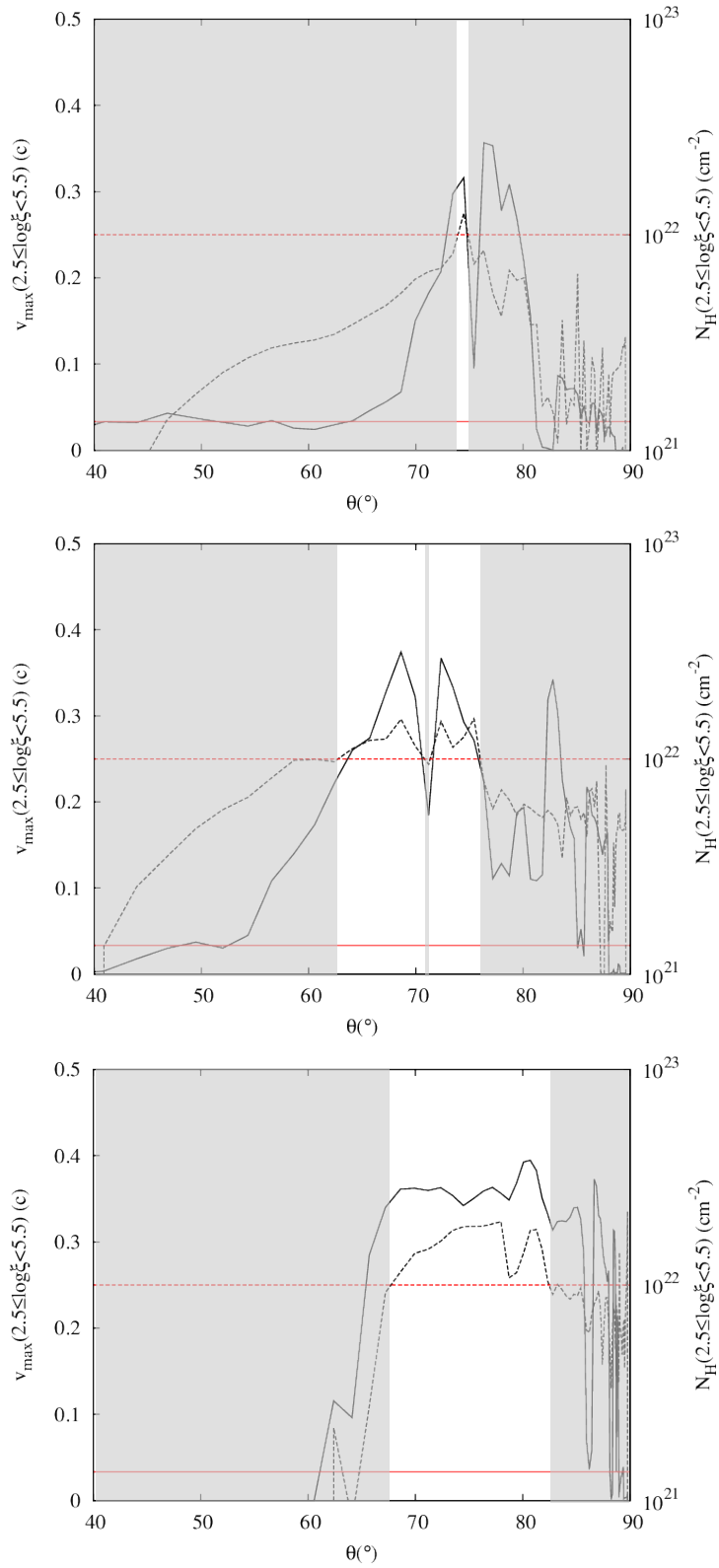


Figure 3.18: Same as Figure 3.6, but for different Eddington ratios,  $\varepsilon = 0.1$  (top panel),  $0.3$  (middle panel), and  $0.7$  (bottom panel).

Table 3.2: Black hole mass dependence of the time averaged UFO probability (%)

Black hole mass ( $M_{\odot}$ )	$10^{7.5}$	$10^8$	$10^{8.5}$	$10^9$
UFO probability	0	20.4	23.5	28.5

this snapshot, the UFO probability is 18.6 %. In the large part of the shaded region, the maximum velocity reaches  $10,000 \text{ km s}^{-1}$ , but the column density is insufficient to meet the condition of  $> 10^{22} \text{ cm}^{-2}$ . The main reason that the UFO is not detected is small column density of the matter with  $2.5 \leq \log \xi < 5.5$ .

In the case of  $\varepsilon = 0.7$  (bottom panel), the maximum velocity and the column density rapidly rise around  $\theta = 65^\circ$ , and the UFO is observed in the range of  $\theta \sim 70^\circ$  to  $80^\circ$ . The detectable range of the UFO is slightly larger than that for smaller Eddington ratios and shifted toward large polar angle. Thus, the result shows the large UFO probability 25.4% for this snapshot.

**Black hole mass dependence**— Table 3.2 shows the black hole mass dependence of the time averaged UFO probability. We investigate the disk wind for  $M_{\text{BH}} = 10^{7.5} M_{\odot}$ ,  $10^{8.5} M_{\odot}$ , and  $10^9 M_{\odot}$  with no change of the Eddington ratio,  $\varepsilon = 0.5$ . Except for the case of  $M_{\text{BH}} = 10^{7.5} M_{\odot}$ , the UFO probability is  $\sim 20 - 30\%$ . For the small black hole mass,  $\lesssim 10^{7.5} M_{\odot}$ , the UFO is not detected though the disk wind is successfully launched.

Figure 3.19–3.21 show the color maps of the density, temperature and ionization parameter and the velocity field like Figure 3.1, but for  $M_{\text{BH}} = 10^{7.5} M_{\odot}$ ,  $10^{8.5} M_{\odot}$  and  $10^9 M_{\odot}$ . There is the tendency that the more dense and fast outflow appears for smaller black hole masses.

We find the disk wind similar to that for  $10^8 M_{\odot}$  in the top left panel of Figure 3.19. But the density is higher near the disk surface. This makes the X-ray shielding more effective. As a result, the region with the low ionization parameter and low temperature increases (bottom left panel and top right panel of Figure 3.19). In the low ionization region, the line force accelerates the wind toward high velocity (bottom right panel). Weak attenuation of the UV radiation also assists the acceleration by the radiation force. For the small black hole masses, the attenuation of the UV radiation is relatively weak at the same distance from the central black hole, which is normalized by  $R_{\text{S}}$ , because the optical depth is proportional to the black hole mass,  $\tau = \sigma_{\text{e}} \rho R \propto R_{\text{S}} \propto M_{\text{BH}}$ .

The structures of the disk winds for  $M_{\text{BH}} = 10^{8.5} M_{\odot}$  (Figure 3.20) and  $10^9 M_{\odot}$  (Figure 3.21) are quite similar. In the top left panels of the both figures, we find that the density

is smaller than that for  $M_{\text{BH}} = 10^{7.5}M_{\odot}$  and  $10^8M_{\odot}$  (see the top left panels of Figure 3.19 and Figure 3.1). Then the region with the low ionization parameter and low temperature decreases due to the weak X-ray shielding effect (bottom left panels and top right panels). In addition, the UV radiation force is strongly attenuated because the optical depth becomes larger with the increase of the black hole mass. For example, along the light-ray of  $\theta \gtrsim 75^\circ$ , the UV radiation force is diluted more than 10% in the central region. As a consequence, the acceleration region shrinks and velocity becomes small (bottom right panels).

Figure 3.22 is the same as Figure 3.6, but for different black hole masses,  $M_{\text{BH}} = 10^{7.5}M_{\odot}$  (top panel),  $10^{8.5}M_{\odot}$  (middle panel), and  $10^9M_{\odot}$  (bottom panel). For  $M_{\text{BH}} = 10^{7.5}M_{\odot}$  (top panel), the UFO is undetected independent from the viewing angle though the wind is successfully launched and blown away into a large angle. The maximum velocity largely exceeds the condition value,  $10,000 \text{ km s}^{-1}$ . The reason for that the UFO is undetectable is that the column density of the matter with  $2.5 \leq \log \xi < 5.5$  is small. As I mentioned, the column density is proportional to the black hole mass. Then the condition (B)  $N_{\text{H}}(2.5 \leq \log \xi < 5.5) > 10^{22} \text{ cm}^{-2}$  (see § 3.2.3) becomes harder to meet with the decrease of the black hole mass.

For the  $M_{\text{BH}} = 10^{8.5}M_{\odot}$  (bottom panel), the UFO is observed around  $70^\circ$ – $80^\circ$ . In the large part of the shaded region in which the UFO is undetectable, the condition (A) nor (B) (see § 3.2.3) is satisfied. For the more larger black hole mass,  $M_{\text{BH}} = 10^9M_{\odot}$  (bottom panel), the UFO is observed in wide ranges of the viewing angle though the disk wind not so dense and fast (see Figure 3.21). This is because the large column density that meets the UFO condition (B) in a wide range of the viewing angle. Here we comment again that the column density is proportional to the black hole mass. For large black hole masses, the condition (B) is easy to satisfy. In this case, in the shaded region where the UFO is not observed, the column density is enough large to meet the UFO condition (B), but the maximum velocity is smaller than  $10,000 \text{ km s}^{-1}$  and the condition (A) is not satisfied.

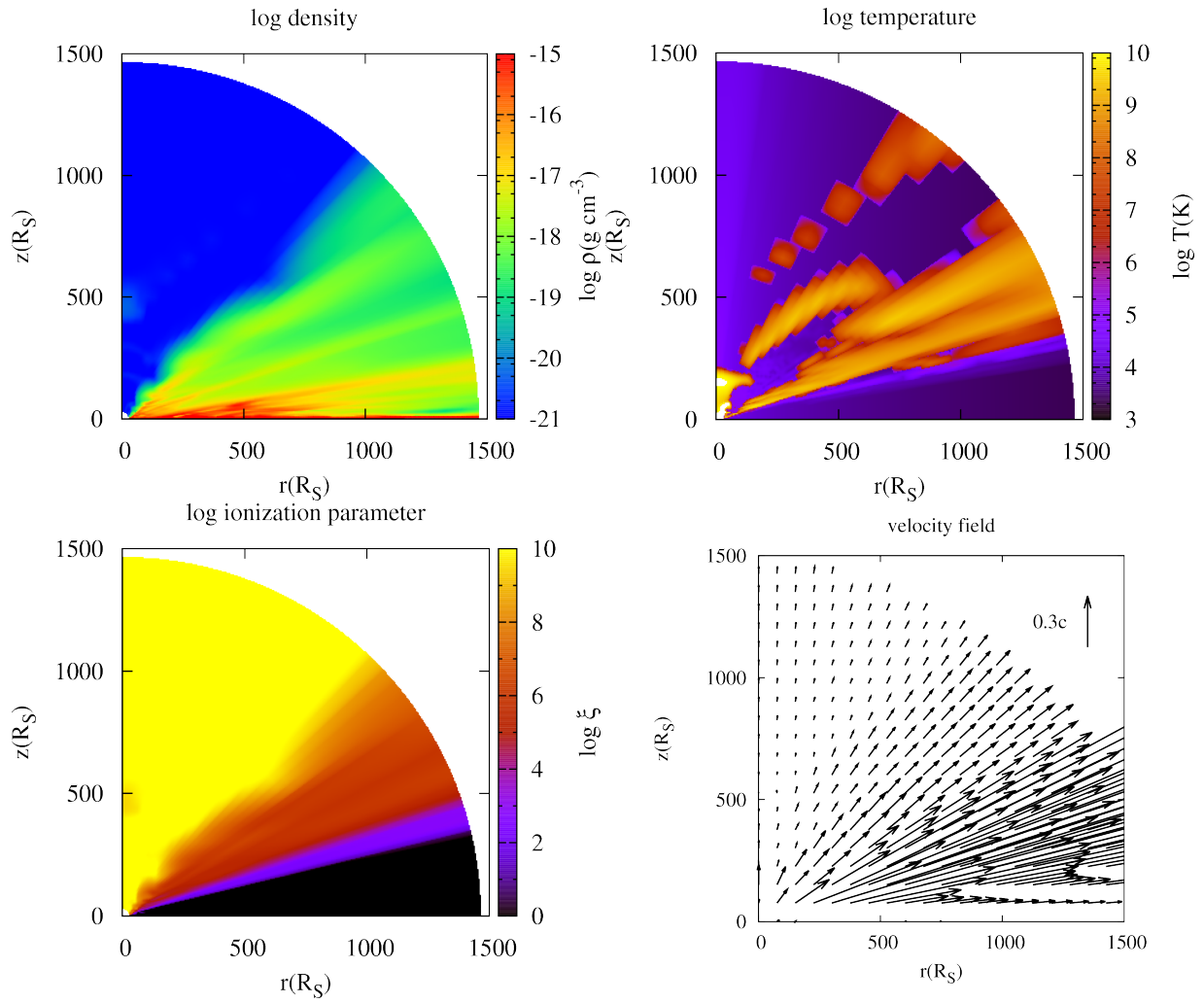


Figure 3.19: Same as Figure 3.1, but for  $M_{\text{BH}} = 10^{7.5} M_{\odot}$ .

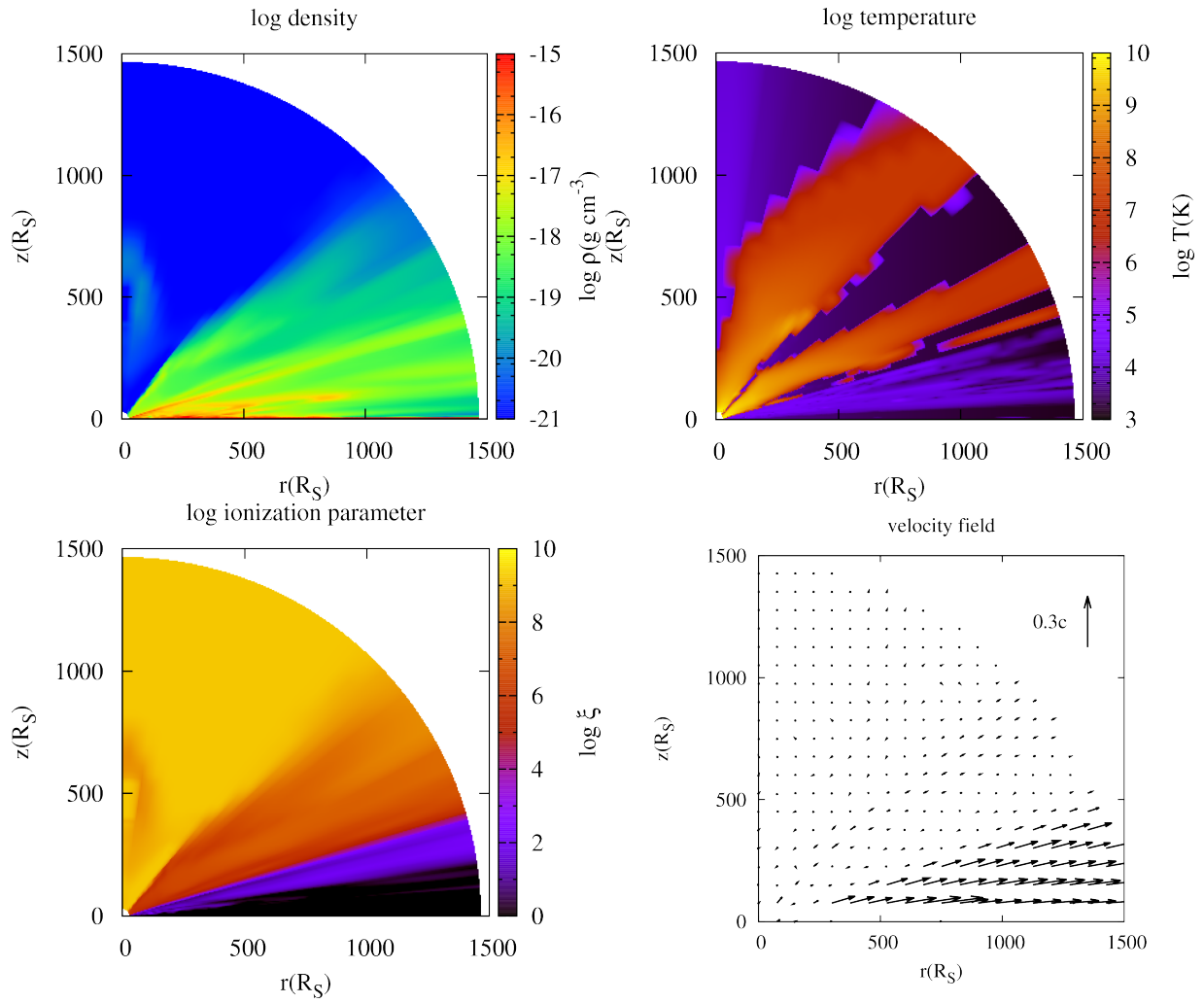


Figure 3.20: Same as Figure 3.1, but for  $M_{\text{BH}} = 10^{8.5} M_{\odot}$ .

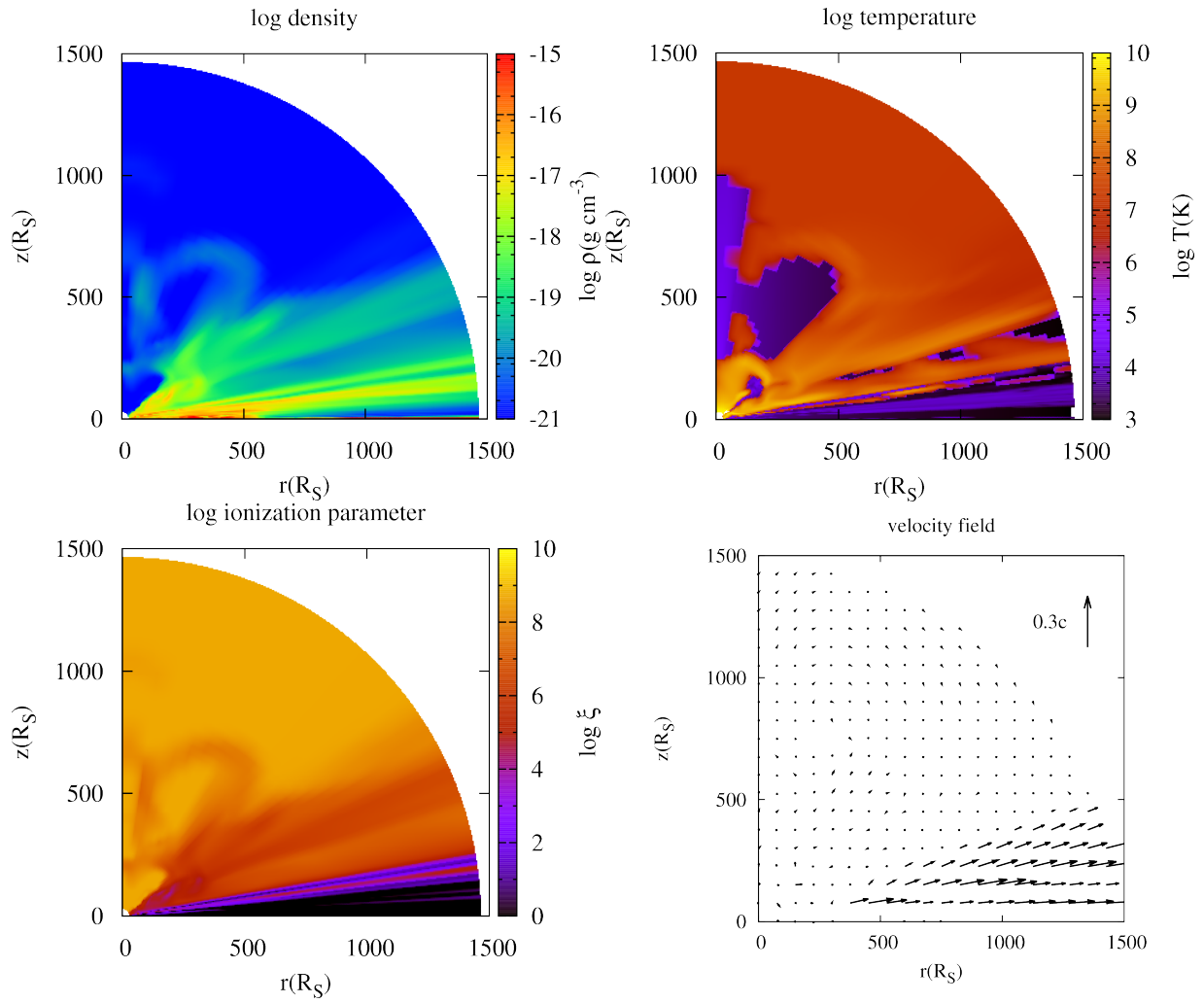


Figure 3.21: Same as Figure 3.1, but for  $M_{\text{BH}} = 10^9 M_{\odot}$ .

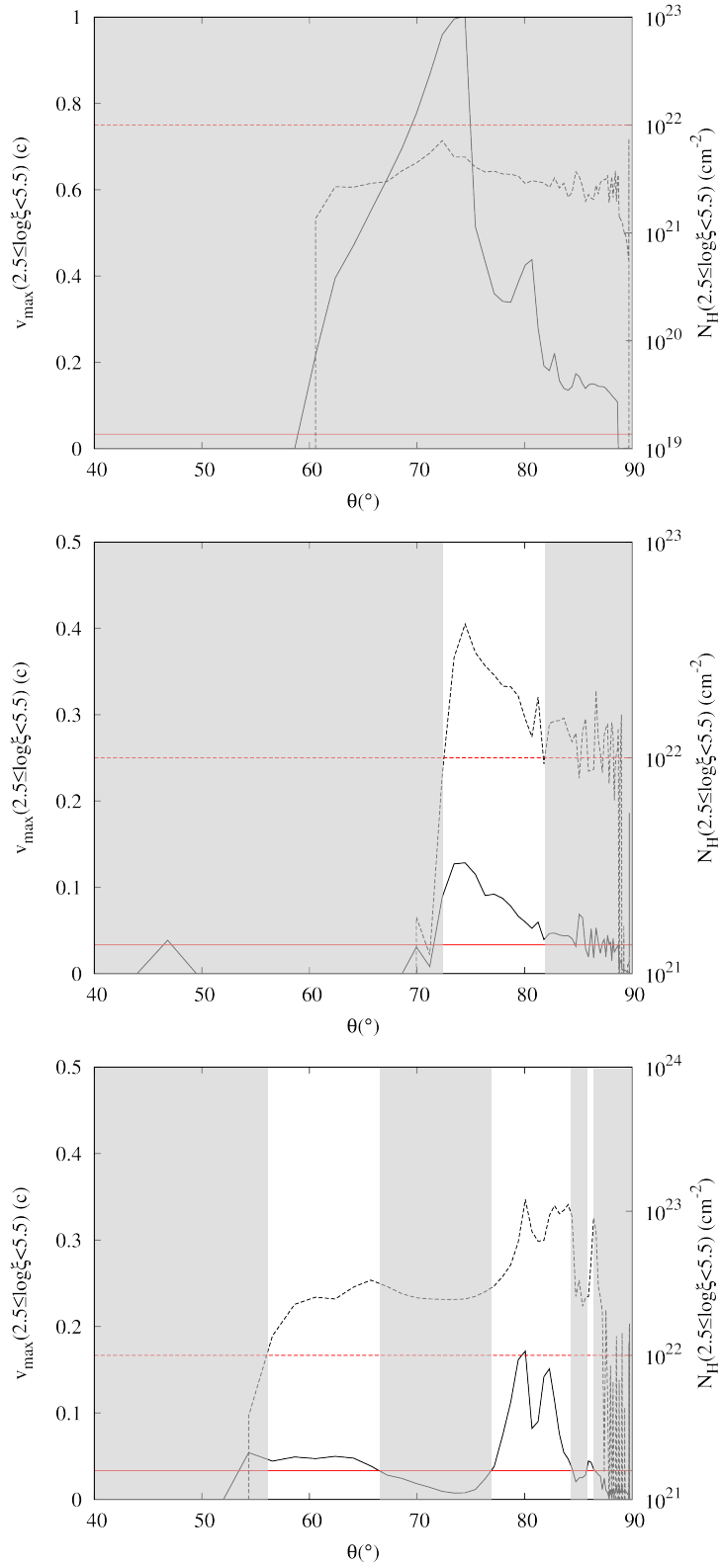


Figure 3.22: Same as Figure 3.6, but for different black hole masses,  $M_{\text{BH}} = 10^{7.5} M_{\odot}$  (top panel),  $10^{8.5} M_{\odot}$  (middle panel), and  $10^9 M_{\odot}$  (bottom panel).

### 3.3 Discussions

#### 3.3.1 Comparison with observations

**Comparison with observations of UFO**— By comparing the results of our simulations and the X-ray observation of the UFOs, we find that the UFO features, the outflow velocity, the ionization parameter and the column density are reproduced by the line-driven disk wind. Based on our analysis, the time averaged UFO probability is 20%–30%, which is comparable to or slightly smaller than that estimated by the observation,  $\sim 50\%$  (Tombesi et al., 2011). The resulting UFO probability might increase if the nuclei strongly obscured by the torus, which aligns with the accretion disk, are excluded from the samples for the UFO survey. In fact, Tombesi et al. (2011) selected only the type 1 sources and the type 2 sources of which the X-ray is affected by the neutral absorption with a column density lower than  $10^{24} \text{ cm}^{-2}$ , because the nuclear continuum radiation is not assured in the obscured sources. Thus, the UFO probability based on our simulations might come closer that estimated by the observation. Additionally, the samples of the sources, which are used to estimate the UFO probability, are still small, and statistical survey of the UFOs is now developing. Our results are suggestive for the new observation in years to come.

Our results suggest that the dichotomy of the UFO and non-UFO depends on not only the viewing angle but also the Eddington ratio and the black hole mass. For the small Eddington ratio,  $\varepsilon \sim 0.1$ , the time averaged UFO probability is very small,  $\sim 3\%$ , and for the small black hole mass,  $M_{\text{BH}} \lesssim 10^{7.5} M_{\odot}$ , the UFO probability is null even though the disk winds are successfully launched in both cases. The UFO probability becomes slightly larger with the increase of the Eddington ratio and the black hole mass, but the percentages are within 20%–30%. In the parameter range in which the UFO is detectable,  $\varepsilon \gtrsim 0.3$  and  $M_{\text{BH}} \gtrsim 10^8 M_{\odot}$ , the difference between the UFO and non-UFO is determined largely on the viewing angle like the phenomenological model of the wind (Elvis, 2000). In other words, the simple wind model of Elvis (2000) can be explained by the line-driven mechanism, but there is the condition of the Eddington ratio and the black hole mass for the nucleus to eject the wind that reproduces the features of the UFO.

From our results, we find that the UFO has the time variability of which the time scale is  $\sim 20$  days to several months. For some viewing angles, the UFO features come and go at this time scale (see Figure 3.13 and 3.14), which is similar to the rapid time variability of the UFO reported by Tombesi et al. (2012b). They show that the transition

between the UFO and non-UFO occurs in  $\sim 7$  days in 3C111. In this paper, we find that the reason for the transition event between the UFO and non-UFO is the variation of the column density of the matter with the feasible ionization parameter. The variation of the column density results from the time variability of the density structure of the wind. To reveal the origin of the time variability of the density structure, more detailed analyses are required. One possible origin is the instability of the line driving. Owocki & Puls (1999) reported the density fluctuations due to the line driven mechanism for the one-dimensional problem of the stellar wind.

**Absorption features observed in black hole X-ray binaries**— The absorption features by highly ionized metals, FeXXV and/or FeXXVI, are found in the black hole X-ray binaries (e.g., Ponti et al., 2012; Neilsen, 2013). These absorption lines suggest the existence of the outflows that are different from jets in the X-ray binary systems. For the X-ray binaries, the acceleration of the wind by the line force is not likely, because the accretion disk is luminous in the X-ray. The strong X-ray irradiates the disk surface and ionizes the metals. Then the line force cannot work efficiently in this situation (Proga & Kallman, 2002). Another model is the thermal wind heated by the strong X-ray radiation (e.g., Luketic et al., 2010), but the simulated thermal wind is weak to reproduce the column density and outflow velocity suggested by the observations. The remaining possibilities are the magnetically-driven wind (e.g., Blandford & Payne, 1982), the wind driven by the radiation force due to the absorption of ionizing X-ray photons via the bound-free transition, or the hybrid of two or more acceleration mechanisms. The simple treatment of the acceleration by the X-ray via the bound-free transition like the force multiplier has not established yet. It might be important future work to consider the X-ray absorption effect for applying the radiation-driven wind model to the disk winds in the X-ray binaries.

### 3.3.2 Comparison with previous works

Our result for  $\varepsilon = 0.5$  and  $M_{\text{BH}} = 10^8 M_{\odot}$  is basically similar to the result of PK04. As I mentioned in §3.1, our calculation method is almost same as PK04, but we simplify the treatment of the UV radiation. In PK04, they use the intensity of the radiation integrated by the wavelength between 200–3200 Å. In our calculation, we simply set the UV emitting region of the accretion disk based on the disk temperature,  $r \leq r_{\text{out}}(T_{\text{eff}} = 3 \times 10^3 \text{K})$ . Then we regard the radiation from this region as the UV radiation contributing to the line-driving. This treatment slightly overestimates the UV radiation than that of PK04.

Another difference of the method is that we consider the photoelectronic absorption when we calculate the attenuation of the X-ray. PK04 assumes that the X-ray is attenuated due to only the electron scattering. Our treatments explained above are almost the same as (Proga et al., 2000; Risaliti & Elvis, 2010; Nomura et al., 2013). In addition, in our calculation, the height of the  $z = 0$  plane roughly corresponding to the scale height of the accretion disk is configured on be smaller than that of PK04. Therefore, the  $z = 0$  plane is placed near the UV radiation source. As a result of these treatments, the outflow velocity of our resultant wind is larger than what is suggested by PK04.

Relative to PK04 focusing on the wind structure for the typical parameter, our work investigates the disk wind in a wide parameter range. Additionally, different from the previous works attempting to reproduce the absorption features represented by the BALs, we focus on whether the line-driven disk wind reproduces the UFOs. Here we simply compare the outflow velocity, the ionization parameter and the column density between our results and the X-ray observations. To investigate the absorption features made by the line-driven disk wind more precisely, we need to calculate the synthetic spectra and compare them directly with the X-ray observations like Schurch et al. (2009) and Sim et al. (2010). However, to make the comparisons in a wide parameter range and a wide range of the viewing angle, and to roughly estimate the UFO probability, our simplified method is useful.

### 3.3.3 Future works

**Calculation of synthetic spectra** — As we mentioned above, to compare our model with the X-ray observations, the calculation of the synthetic spectra is necessary. In previous works (Schurch et al., 2009; Sim et al., 2010), the spectra are calculated based on the result of PK04 for the typical parameter. However, our results show that there are the dependences of the wind structure and the UFO probability on the Eddington ratio and the black hole mass. Thus the calculation of the spectra also should be performed in the wide parameter range. From these synthetic spectra, we might be able to find not only the angle dependence and the time dependence but also the dependence on the Eddington ratio and the black hole mass.

Based on our results of the density and the velocity, we plan to calculate the spectra by using CLOUDY. CLOUDY is an open code that calculates the radiation transfer. By assuming the atomic abundance and setting the input continuum spectrum, CLOUDY calculates the interaction between the radiation and the matter. As a consequence, we

obtain the ionization state, the temperature, and the synthetic spectra after passing through the disk wind.

Here we comment that, in this method, the calculation of the radiation transfer is the post-process after the hydrodynamic simulations. The result of the radiation transfer gives no feedback to the dynamics of the wind. Still computational power is not sufficient to self-consistently calculate wind dynamics and radiation transfer depending on the wavelength at the same time.

**Three-dimensional radiation hydrodynamic simulations**— To understand the origin of the time variability of the absorption lines, it is not enough to investigate the dynamics of the wind assuming the axial symmetry. Some phenomenological models to explain the time variability of the absorption lines are proposed (§ 1.4.2). The most plausible model for BALs is that the ionization state of the BAL clouds is changing since the X-ray shielding clouds are crossing between the continuum source and BAL clouds (Misawa et al., 2007; Capellupo et al., 2013). According to the estimation by Capellupo et al. (2013), the shielding clouds are located  $10\text{--}200R_S$  from the nucleus and might to be a part of the disk wind or the failed wind. In fact, we found the partly failed and partly successfully launched winds in this region and they play a role of shielding gas. The density distribution and the time variability of the wind structure in this inner region are important to clarify the origin of the time variability of absorption features such as BALs. Therefore it is necessary to investigate more realistic structure of the wind such as the non-axial symmetric structure and the break up of the wind.

Before now, all previous works assumed the axial symmetry. In the three-dimensional simulations, the disk winds are expected to show the clumpy and non-axial symmetric structures. The radiation force including the line force is sensitive to the change in the velocity, the density and the ionization state of metals. For example, the line force works more effective on the absorber with large velocity gradient. This means that the accelerated wind is more accelerated by the line force. On the other hand, the wind with the weak acceleration is not strongly accelerated any more, because the line force is less effective. The line force induces the positive feedback and instability. This instability grows the ununiformity of the density distribution, and the disk wind might become clumpy. Even in the two-dimensional simulations such as our calculation and Proga et al. (2000), the density fluctuations are found. For the one-dimensional problem, the density fluctuations due to the instability of the line driving are reported by Owocki & Puls (1999).

Our simulation code can be soon extended to apply three-dimensional calculation and we have already performed the test run of the three-dimensional simulations. We will report the details in a future paper.

**Modification of treatment of radiation transfer**— To estimate the line force, we calculate the radiation transfer of the UV and the X-ray. Roughly speaking, the UV radiation is absorbed via the bound-bound transition and contributes to the line force. The X-ray ionizes metals and reduces the line force. Then, in the simple method here we use, the force multiplier enhances the radiation force by the UV radiation without considering the frequency dependence. In addition, when we estimate the optical depth of the UV radiation, we use the mass-scattering coefficient for free electrons. That is, we do not consider the attenuation due to the bound-bound absorption that depends on the frequency. This leads to the underestimation of the attenuation of the UV. These treatments are approximative methods and we have to calculate the radiation transfer depending on the frequency to estimate a more realistic line force. For the calculation of the radiation transfer depending on the frequency, it is helpful to employ the calculation code like XSTAR or CLOUDY. It is hard to calculate the wind dynamics and the frequency-dependent radiation transfer at one time since the computational power is not enough. However, improving the treatment of the frequency-dependent radiation transfer is one of the important future works.

In our calculation, we ignore the scattered photons. This is the reasonable approximation since many photons are scattered into the polar region in which the density of the matter is low. However, the wind structure might change if we consider the scattered X-ray photons that ionize the metals and reduce the line force. Part of the wind irradiated by the scattered X-ray photons becomes highly ionized and difficult to be accelerated by the line force. In some cases, the wind could not be launched due to the scattered X-ray radiation. Recently, by calculating the radiation transfer as a post process after the hydrodynamic simulations of PK04, Higginbottom et al. (2014) reported that the ionization parameter of the matter becomes large and the line force is suppressed when the scattered and reprocessed photons are considered. To investigate whether the line-driven disk wind is still launched in such circumstances and how the structure changes, the radiation hydrodynamic simulations containing the scattered and reprocessed radiation is important.

**Calculation of accretion disk**— In our simulations, we assume that the accretion disk is geometrically thin and optically thick standard disk (Shakura & Sunyaev, 1973).

The internal configuration of the disk is excluded from the simulation box. The  $\theta = 90^\circ$  plane corresponds to the static disk surface, and we set the boundary condition that the density on the grids of  $\theta = 90^\circ$  is constant independently from the time. Thus, the density is supplied from the accretion disk if the matter on the surface is blown away as the disk wind. In addition, we treat the accretion disk as the external UV radiation source. The UV radiation comes from the equatorial plane of the disk and the radiation field is steady. However, in reality, the condition of the disk might change if the mass outflow rate due to the disk wind is large. In our simulations, the resulting mass outflow rate is comparable or slightly larger than the mass accretion rate, so it is better to consider the impact on the accretion disk due to the wind. To achieve this, we need to calculate the configuration of the accretion disk by radiation (magneto) hydrodynamic simulations. The UV radiation comes from no longer the external source, but the accretion gas itself. To obtain the realistic wind structure and evaluate the impact on the disk, it is a momentous work to calculate the disk wind and the accretion disk self-consistently.

## 4 Conclusion

We researched the line-driven disk wind in the AGNs and compared our results with the X-ray observations of BAL quasars and UFOs in Seyfert galaxies.

First, we investigated the steady structure of the disk wind driven by the radiation force including the line force, by calculating the trajectories of the fluid elements that are launched from the surface of the geometrically thin and optically thick disk. Here, the density and velocity at the wind base are set so as meet the condition of line-driven stellar wind (Castor, Abbott, & Klein, 1975). We have solved the equation of motion, coupling with the mass conservation along the streamlines. The radiation force, the ionization parameter, and the temperature are calculated by taking into consideration the attenuation of the X-ray from the vicinity of the black hole and the UV from the disk via the ejected matter. We have compared the resulting wind structure with the wind properties of X-ray observations of the BAL quasars (the ionization parameter, the outward velocity, and the column density), and estimated the probability (BAL probability), with which the system is identified as a BAL quasar.

In the case that the Eddington ratio is  $\varepsilon \sim 0.3\text{--}0.9$  and the black hole mass is  $M_{\text{BH}} \sim 10^7\text{--}10^{8.5}M_{\odot}$ , we found that the funnel-shaped disk wind with an opening angle of  $\sim 50^\circ$  forms. In this regime, since the wind shape is insensitive to the Eddington ratio and the black hole mass, the BAL probability of several to 10% does not change so much.

The wind is launched from the middle region of the disk, where the line force is strong enough to accelerate the matter. In the inner region, since the larger initial density reduces the force multiplier (line force), the ejected matter immediately returns to the disk surface. On the other hand, in the outer region, since the UV radiation is attenuated via the obscuration by the matter in the inner and middle regions, the radiation force fails to launch the wind. In the case of  $M_{\text{BH}} = 10^7M_{\odot}$  and  $\varepsilon = 0.3$ , the launching region is  $30R_{\text{S}} \lesssim r \lesssim 350R_{\text{S}}$ .

If the Eddington ratio is very small ( $\varepsilon \lesssim 0.01$ ), the disk wind does not appear, since the UV intensity is too weak for the matter to be accelerated by the line force. Also, the disk wind is not launched when the black hole is too massive ( $M_{\text{BH}} \gtrsim 10^9M_{\odot}$ ). This is because that the force multiplier at the wind base decreases with an increase of the black hole mass. In addition, the disk temperature also decreases (UV emission region,  $T_{\text{eff}} > 10^4\text{K}$ , shrinks) with an increase of the black hole mass. Thus, for  $\varepsilon \lesssim 0.01$  or for  $M_{\text{BH}} \gtrsim 10^9M_{\odot}$ , the BAL quasars are not observed independently of the viewing angle.

Second, we have performed the two-dimensional radiation hydrodynamic simulations of the line-driven disk wind assuming the axial symmetry. For simplicity, we assumed that the density of the wind base ( $z = 0$  plane) is constant and independent from the disk radius, the Eddington ratio and the black hole mass. The treatment of the radiation transfer is almost the same as the non-hydrodynamic method. We estimated the line force by calculating the force multiplier considering the ionization state of the metals. By numerical calculation of the equation of continuity, the equation of motion considering the line force and the energy equation considering radiative heating and cooling due to the X-ray irradiation, we investigate the time dependent structure of the line-driven disk wind. Also, we compared the resultant ionization parameter, the outward velocity and the column density with those inferred from the X-ray observation of UFOs. We calculated the UFO probability and investigated the time variability of the absorption feature.

As a consequence, we found the funnel-shaped disk wind consistent with the result of the non-hydrodynamic method. For the case of  $\varepsilon = 0.5$  and  $M_{\text{BH}} = 10^8 M_{\odot}$ , in the upper region of the funnel, the ionization parameter is high,  $\log \xi \sim 5$ , and the wind is accelerated only near the disk surface in which the ionization parameter is enough low for the line force to accelerate the disk wind. Therefore, the terminal velocity is relatively small,  $v_r < 0.1c$ , and a part of the wind returns to the disk. In the equatorial region, the ionization parameter is small,  $\log \xi \lesssim 4$ , and the wind continues to be accelerated after the launching. Then the outflow velocity reaches to  $0.3\text{--}0.4c$ .

For  $\varepsilon = 0.3\text{--}0.9$  and  $M_{\text{BH}} = 10^8\text{--}10^9 M_{\odot}$ , the UFO features are observed in the direction of  $\sim 70^\circ$ . The detection probability of the UFO (UFO probability) fluctuates on the time scale from  $\sim 20$  days to several months and the time-averaged UFO probability is  $20\text{--}30\%$ . This is comparable to or slightly smaller than that estimated by the observation,  $\sim 50\%$ . For  $\varepsilon \lesssim 0.1$  and  $M_{\text{BH}} \lesssim 10^{7.5} M_{\odot}$ , the disk wind is launched, but the UFO probability is pretty small or null since the column density of the matter with the feasible ionization state is small.

Finally, we conclude that the line force successfully launches the disk wind for both cases of using the non-hydrodynamic method and the radiation hydrodynamic simulations. The line-driven disk wind model can reproduce the absorption features of the BALs and UFOs. In addition, not only the viewing angle, but also the Eddington ratio and the black hole mass are responsible for whether or not the AGNs exhibit the absorption features.

## Acknowledgments

I would like to express my sincere gratitude to my supervisor, M. Morikawa, for wide-ranging discussions, helpful advices, and strong supports throughout my doctoral program. I am deeply grateful to K. Ohsuga for helpful discussions and strong supports throughout this work, especially during my stay in National Astronomical Observatory of Japan (NAOJ). I am grateful to K. Wada, H. Susa, T. Misawa, and H. Takahashi for significant contribution to this thesis. I wish to thank G. Cho, K. Kobayashi, M. Ban, and R. Matsumoto for careful reading and improving my manuscripts. I also wish to thank the members of the astrophysics group, Ochanomizu Univ. and the members of the division of the theoretical astronomy, NAOJ. Numerical computations in §3 were carried out on Cray XC30 at the Center for Computational Astrophysics, CfCA, at NAOJ. I received support from the Research Fellowship for Young Scientists from Japan Society for the Promotion of Science (JSPS).

## References

- Allen, J. T., Hewett, P. C., Maddox, N., Richards, G. T., & Belokurov, V. 2011, MNRAS, 410, 860
- Antonucci, R. R. J., & Miller, J. S. 1985, ApJ, 297, 621
- Blandford, R. D., & Payne, D. G. 1982, MNRAS, 199, 883
- Braitto, V., et al. 2006, Astronomische Nachrichten, 327, 1067
- Brandt, W. N., Laor, A., & Wills, B. J. 2000, ApJ, 528, 637
- Capellupo, D. M., Hamann, F., Shields, J. C., et al. 2012, AGN Winds in Charleston, 460, 88
- Capellupo, D. M., Hamann, F., Shields, J. C., Halpern, J. P., & Barlow, T. A. 2013, MNRAS, 429, 1872
- Castor, J. I., Abbott, D. C., & Klein, I. 1975, ApJ, 195, 157
- Chartas, G. 2007, Spectral Line Shapes in Astrophysics, 938, 3
- Elvis, M. 2000, ApJ, 545, 63
- Everett, J. E., & Murray, N. 2007, ApJ, 656, 93
- Gallagher, S. C., Brandt, W. N., Wills, B. J., Charlton, J. C., Chartas, G., & Laor, A. 2004, ApJ, 603, 425
- Ganguly, R., Bond, N. A., Charlton, J. C., et al. 2001, ApJ, 549, 133
- Ganguly, R., Masiero, J., Charlton, J. C., & Sembach, K. R. 2003, ApJ, 598, 922
- Gayley, K. G. 1995, ApJ, 454, 410
- Gregg, M. D., Becker, R. H., Brotherton, M. S., et al. 2000, ApJ, 544, 142
- Gültekin, K., Richstone, D. O., Gebhardt, K., et al. 2009, ApJ, 698, 198
- Hamann, F., Korista, K. T., & Morris, S. L. 1993, ApJ, 415, 541
- Higginbottom, N., Knigge, C., Long, K. S., Sim, S. A., & Matthews, J. H. 2013, MNRAS, 2343

Higginbottom, N., Proga, D., Knigge, C., et al. 2014, arXiv:1402.1849

Jannuzi, B. T., et al. 1996, ApJL, 470, L11

Khachikian, E. Y., & Weedman, D. W. 1974, ApJ, 192, 581

Konigl, A., & Kartje, J. F. 1994, ApJ, 434, 446

Krongold, Y., Nicastro, F., Elvis, M., et al. 2007, ApJ, 659, 1022

Luketic, S., Proga, D., Kallman, T. R., Raymond, J. C., & Miller, J. M. 2010, ApJ, 719, 515

Magorrian, J., Tremaine, S., Richstone, D., et al. 1998, AJ, 115, 2285

Miniutti, G., Saxton, R. D., Rodríguez-Pascual, P. M., et al. 2013, MNRAS, 433, 1764

Misawa, T., Eracleous, M., Charlton, J. C., & Kashikawa, N. 2007, ApJ, 660, 152

Morabito, L. K., Dai, X., Leighly, K. M., Sivakoff, G. R., & Shankar, F. 2013, arXiv:1309.5978

Murray, N., Chiang, J., Grossman, S. A., & Voit, G. M. 1995, ApJ, 451, 498

Neilsen, J. 2013, Advances in Space Research, 52, 732

Nomura, M., Ohsuga, K., Wada, K., Susa, H., & Misawa, T. 2013, PASJ, 65, 40

Owocki, S. P., Castor, J. I., & Rybicki, G. B. 1988, ApJ, 335, 914

Owocki, S. P., & Puls, J. 1999, ApJ, 510, 355

Ponti, G., Fender, R. P., Begelman, M. C., et al. 2012, MNRAS, 422, L11

Pounds, K. A., Reeves, J. N., King, A. R., et al. 2003, MNRAS, 345, 705

Proga, D., Stone, J. M., & Drew, J. E. 1998, MNRAS, 295, 595

Proga, D., Stone, J. M., & Drew, J. E. 1999, MNRAS, 310, 476

Proga, D., Stone, J. M., & Kallman, T. R. 2000, ApJ, 543, 686

Proga, D., & Kallman, T. R. 2002, ApJ, 565, 455

Proga, D., & Kallman, T. R. 2004, ApJ, 616, 688

Reeves, J. N., O'Brien, P. T., & Ward, M. J. 2003, *ApJL*, 593, L65

Risaliti, G., & Elvis, M. 2010, *A&A*, 516, 89

Rodríguez Hidalgo, P., Eracleous, M., Charlton, J., et al. 2013, *ApJ*, 775, 14

Shakura, N. I., & Sunyaev, R. A. 1973, *A&A*, 24, 337

Schurch, N. J., & Done, C. 2007, *MNRAS*, 381, 1413

Schurch, N. J., Done, C., & Proga, D. 2009, *ApJ*, 694, 1

Sim, S. A., Proga, D., Miller, L., Long, K. S., & Turner, T. J. 2010, *MNRAS*, 408, 1396

Stevens, I. R., & Kallman, T. R. 1990, *ApJ*, 436, 599

Takahashi, H. R., & Ohsuga, K. 2013, *ApJ*, 772, 127

Tombesi, F., Cappi, M., Reeves, J. N., et al. 2010, *A&A*, 521, A57

Tombesi, F., Cappi, M., Reeves, J. N., et al. 2011, *ApJ*, 742, 44

Tombesi, F., Cappi, M., Reeves, J. N., & Braitto, V. 2012a, *MNRAS*, 422, L1

Tombesi, F., Sambruna, R. M., Marscher, A. P., et al. 2012b, *MNRAS*, 424, 754

Turner, T. J., Reeves, J. N., Kraemer, S. B., & Miller, L. 2008, *A&A*, 483, 161

Wang, J., Jiang, P., Zhou, H., Wang, T., Dong, X., & Wang, H. 2008, *ApJL*, 676, L97

Weymann, R. J., Morris, S. L., Foltz, C. B., & Hewett, P. C. 1991, *ApJ*, 373, 23